



Università di Genova

UNIVERSITY OF GENOVA

PHD PROGRAM IN MECHANICAL, ENERGY AND MANAGEMENT ENGINEERING

DESIGN, OPTIMISATION, AND ACTUATION OF TENDON-DRIVEN HYPER-REDUNDANT MANIPULATORS

by

Ardit Poka

Thesis submitted for the degree of *Doctor of Philosophy* (XXXVIII cycle)

March 2026

PhD Carlo Canali — Supervisors
Prof. Giovanni Berselli
Prof. Darwin G. Caldwell

Prof. Giovanni Berselli — Head of the PhD program

DECLARATION

I hereby declare that, except where specific reference is made to the work of others, the contents of this dissertation are original and have not been submitted in whole or in part for consideration for any other degree or qualification in this, or any other university. This dissertation is my own work and contains nothing that is the outcome of work done in collaboration with others, except as specified in the text and Acknowledgements. This dissertation contains fewer than 65,000 words, including appendices, bibliography, footnotes, tables and equations and has fewer than 150 figures.

Ardit Poka
March 2026

ACKNOWLEDGEMENTS

This journey was not just about intellectual ability. In my experience, it is mostly about refusing to quit. I did not reach this milestone on my own. This thesis represents the collective effort, support, and patience of many individuals who stood beside me.

I must first express my deepest gratitude to my supervisors. Dr. Carlo Canali has been a constant source of support. He is a rare example of a supervisor who combines supervision with sincere care for people. He was available whenever I needed guidance.

I am equally grateful to Prof. Giovanni Berselli. He is a phenomenal mentor and a great person. He provided me with opportunities that helped me grow as a researcher. His guidance directed my entire career path.

My daily work relied heavily on my colleagues' support. Daniele was a mentor and a friend. There were many moments of difficulty where I saw no way forward. Daniele always had a solution. I do not believe I would have finished this PhD without his help. Lorenzo was another essential resource. He helped me solve many problems and supported me in many ways. I am also grateful to Federico. We worked side by side on almost everything. We learned, designed, and built together. We spent evenings until 11 pm writing papers, eating dinner at our desks, and joking despite the tiredness. I also thank Alessandro. Though he left IIT some time ago, his guidance during my early days was important, and his humour was a much needed distraction.

I am especially grateful to the entire staff at IIT for all the support and the great work they do to provide researchers with everything they need.

My family remains the most important part of my foundation. My mom, dad, brother, and sister have supported me unconditionally. They encouraged me to aim for the stars even when I doubted myself. They never stopped believing in me.

Finally, my girlfriend Denise. She has been my anchor. She understood the pressure and the stress. Her support was fundamental to my mental well-being. She helped me maintain hope during the most challenging periods. She is the reason I kept going.

ABSTRACT

Tendon-driven hyper-redundant manipulators allow safe inspection and maintenance in confined, hazardous environments by keeping actuators outside the work zone and moving through tight, cluttered spaces. However, their long tendon routings introduce friction, elasticity, and slack that often degrade performance in real-world scenarios.

This thesis addresses these limitations through a complete design-to-application framework. A lightweight, 3D-printed 5-joint polymeric manipulator is developed with compact integration, embedded sensors, and an off-board actuation unit that includes active global tendon tensioning. The manipulator provides a platform for investigating real-world performance limits.

A central challenge in the robot's design was determining critical load cases for design optimisation. Traditional worst-case loading assumptions led to overdesign and inefficient material use. To overcome this, a data-driven framework based on Gaussian Process regression and Bayesian Optimisation is introduced. It identifies load configurations that induce worst-case stress on structural components while minimising the number of costly simulations. This method allows both design-time optimisation and safe operation by predicting and avoiding stress-critical joint configurations.

Using this platform and optimisation framework, experiments are conducted on the robot to quantify tensioning efficiency at rest and in motion, while systematically excluding joint configurations associated with maximum stress. Furthermore, a simple model is obtained to link commanded tension to slack mitigation. Subsequently, experiments quantify hysteresis losses and overall mechanical efficiency of the tensioning system. Further testing characterises stiffness modulation and establishes a direct relationship between tendon tension and payload capacity.

Finally, the optimisation framework is applied to design a longer underwater variant with 8 joints, adapted for inspection tasks in underwater environments. Buoyancy and payload constraints are addressed through geometry reconfiguration and structural mass reduction, allowed by the proposed design method.

Overall, the thesis provides a generalisable approach to tendon-driven robot design, combining mechanical design, experimentation, data-efficient optimisation, and adaptation to real-world scenarios.

TABLE OF CONTENTS

List of figures **ix**

List of tables **xii**

1 Introduction **1**

1.1 Motivation 1

1.2 Foundational work 2

1.3 Main Contributions of this work 4

2 State of Art **7**

2.1 Tendon-Driven Continuum Manipulators 8

2.1.1 NiTi Backbone Manipulators 9

2.1.2 Telescopic Backbone Manipulators 10

2.1.3 Spring Backbone Manipulators 10

2.1.4 Elastic Tube Backbone Manipulators 11

2.1.5 Origami-Like Manipulators 11

2.1.6 Soft Limbs Manipulators 12

2.1.7 Other Tendon-Driven Continuum Manipulators 12

2.2 Tendon-Driven Rigid-Link Manipulators 13

2.2.1 Lightweight Manipulators 14

2.2.2 Long-Reach Manipulators 15

2.2.3 Compliant Joints Manipulators 15

2.2.4 Spring Joint Manipulators 17

2.2.5 U-Joints Manipulators 17

2.2.6 Gear Joints Manipulators 18

2.2.7 Rolling Joint Manipulators 19

2.2.8 Spherical Joints Manipulators 20

2.2.9 Other Tendon-Driven Manipulators 20
2.3 Alternative Actuation Solutions 21
2.4 Design Considerations for Hyper-Redundant Manipulators 24

3 LORY-5JP Design and Implementation 26
3.1 LORY-5JP Design Methodology 27
3.2 Tendon Routing 30
3.3 Sensor Integration 32
3.4 Distributed SPI Daisy-Chain Control Logic 33
3.5 Design Challenges and Limitations 35

4 Bayesian Optimisation of Worst-Case Loads 37
4.1 Mechanical Context and Problem Formulation 38
4.1.1 Robot worst-case stress objective 39
4.1.2 Black-box optimisation setting 40
4.1.3 Load bounds and feasible domain 40
4.2 Data Preparation and Scaling 41
4.2.1 Initial training dataset 41
4.2.2 Normalisation of inputs, outputs, and bounds 41
4.3 Gaussian Process Surrogate Model 42
4.3.1 GP prior, mean function, and kernel 42
4.3.2 Hyperparameter learning via marginal likelihood 43
4.3.3 Posterior prediction and uncertainty 44
4.3.4 Computational considerations and model choice 44
4.4 Bayesian Optimization 45
4.4.1 Acquisition function: Expected Improvement 45
4.4.2 Batch Bayesian optimisation with q-EI 46
4.4.3 Model Performance Evaluation 47

5 Tendon Tensioning, System Validation and Stiffness Control 51
5.1 Tensioning System 51
5.1.1 Tensioning System Overview 52
5.1.2 New Static Model Considering Active Tension 53
5.2 Tensioning System Performance in Static Condition 57
5.2.1 Tension Experiments and Data Acquisition 57
5.2.2 Tensioning system performance 59
5.2.3 Tensioning System Hysteresis and Mechanical Efficiency 60

5.3 Tensioner Effectiveness During Robot Motion 62
5.3.1 Trajectory Generation and Experimental Protocol 62
5.3.2 Tension Analysis 66
5.3.3 Trajectory Tracking Performance vs Tensioner Force 69
5.4 Stiffness Modulation on LORY-5JP 71
5.4.1 Theoretical Framework 72
5.4.2 Experimental Protocol 77
5.4.3 Manipulator Deflection and Stiffness Analysis 80

6 LORY-8JP: Optimisation and Underwater Adaptation 86
6.1 State of the Art on Underwater Manipulators 87
6.1.1 Compliant Robotic Arms 88
6.1.2 Rigid-Joint Robotic Arms 89
6.1.3 Soft Robotic Arms 90
6.1.4 Design Considerations 92
6.2 Design Framework for Underwater Adaptation 93
6.2.1 Optimisation Process and Performance 94
6.2.2 Optimal Streamlined Geometry with Generative Design 96
6.2.3 3D Printing, Buoyancy Design and Testing 101

7 Towards the Metallic Prototype: Torsional Stiffener Design 108
7.1 Problem Description 108
7.1.1 Tube-shaped geometry 111
7.1.2 Rectangular-shaped geometry 112
7.2 Proposed Solutions 113
7.2.1 Solution 1: Tube-Shaped Stiffener 114
7.2.2 Solution 2: Rectangular-Shaped Stiffener 116
7.2.3 Results and Final Considerations 118

8 Conclusion and Future Works 119
8.1 Future Works 120

References 121

Appendix A Nylon and Zylon Material Properties 136

Appendix B Summary of Foundational Models and Prior Work 137
B.1 Tendon Routing Topology 137
B.1.1 The Routing Matrix 137
B.1.2 Geometric Mapping through the Matrix D 138
B.2 Static Model via Newton-Euler Recursion 138
B.2.1 Joint Decomposition and Load Definitions 139
B.2.2 Equilibrium Equations 139
B.2.3 Matrix Resolution 141
B.3 Optimisation of Cable Preloads 141

Appendix C Actuation Hardware Details 143

Appendix D Tensioning system test results: tension in motion 145

LIST OF FIGURES

1.1 Foundational virtual prototype and gear joint geometry 2

2.1 A schematic representation of a simple T-D CHRM 9
2.2 A schematic representation of a simple T-D RLHRM 14
2.3 A long-reach RLHRM prototype [1] 16
2.4 Conceptual schemes of non-T-D extrinsically actuated CHRMs. 22
2.5 Conceptual schemes of non-T-D intrinsically actuated CHRMs. 23
2.6 Conceptual schemes of intrinsically actuated non-T-D RLHRMs. 25

3.1 Rendered picture of a robot link 27
3.2 Rendered representation of a single module from the virtual prototype . 29
3.3 Virtual prototype of LORY-5JP with all its components assembled . . . 31
3.4 Tendon passage through the joint 32
3.5 Implementation of the sensors into the joint module 33
3.6 SPI wiring scheme 34

4.1 Model performance plots 47

5.1 LORY-5JP and its actuation and tensioning system 52
5.2 Working principle of the active-tensioning system 53
5.3 Side view of a tensioning slider 53
5.4 Working principle of the proposed active tensioning system with the case of necessary actuation torque $\tau > 0$ 54
5.5 Measured forces. The output force F_{sl} is measured in both sliders of a single joint. 56
5.6 Comparison of slider tensions 59
5.7 Loading and unloading F_t trends representing the hysteresis loss at the tensioner 61

5.8 Joint angles and their velocities as a function of time. 65
5.9 Relevant tendon tension T_{rel} during motion phase as a function of tensioner force for each joint 67
5.10 Relevant tendon tension T_{rel} during hold phase as a function of tensioner force for each joint 68
5.11 Efficiency comparison between motion and hold phases. 69
5.12 Mean Trajectory Tracking Error vs. F_t 71
5.13 Joint geometry and joint angle representation 73
5.14 Experimental setup for stiffness testing 77
5.15 Marker displacements for each link, with different weights for each tension level 81
5.16 Tip translational stiffness $K_{\text{tip}}(W, F_t)$ versus tensioner force F_t for the three payloads 81
5.17 Rotational stiffness of joints 1, 3, and 5, for the three payloads 83
5.18 Compliance share vs. Tension for all payloads and joints 84

6.1 Number of yearly documents on snake-like underwater robots 87
6.2 Percentages of research papers found on underwater robot designs for each category 88
6.3 Schematic representations of tethered underwater robots 88
6.4 Concept of the underwater system 94
6.5 Optimisation Process 95
6.6 Performance Parameters Plots of the GP model for the first link 96
6.7 Shape of the first joint before and after design constraints. Left: the preliminary design. Right: the final design. 98
6.8 Virtual prototype of the optimised manipulator 101
6.9 Simple buoyancy test on a two-module prototype 103
6.10 Comparison between the two possible BE geometries (left), and the BE base geometry (right) 104
6.11 Implementation of the BE in the modules 105

7.1 Robot configuration corresponding to maximum torsional load on the first joint, M_t. 109
7.2 3D CAD model of the simplified joint highlighting the point P. 110
7.3 Deformed model of the simplified joint showing the constraint on the inner shaft and the torsional load on the outer shaft 110

7.4 Geometrical parameters for a stiffener element surrounding the gears. . 111
7.5 Geometrical parameters for a stiffener element mounted in the inner space of the gears. 113
7.6 Sensitivity analysis for solution 1 in terms of ε. The orange circle highlights the values associated with maximum efficacy. 114
7.7 Sensitivity analysis for solution 1 in terms of ε. The orange diamond highlights the values associated with maximum efficiency. 115
7.8 Design for solution 1 that maximises ε_1. 115
7.9 Design for solution 1 that maximises η_1. 115
7.10 Deformed model of the simplified joint with the stiffener solution 1 that maximises ε. A scale factor of 10 is applied to better visualise the deformation. 115
7.11 Deformed model of the simplified joint with the stiffener solution 1 that maximises η 116
7.12 Sensitivity analysis for solution 2 in terms of ε. The orange circle highlights the values associated with maximum efficacy. 116
7.13 Sensitivity analysis for solution 2 in terms of η. The orange diamond highlights the values associated with maximum efficiency. 116
7.14 Design for solution 2 that maximises ε_2. 117
7.15 Design for solution 2 that maximises η_2. 117
7.16 Deformed model of the simplified joint with the stiffener solution 2 that maximises ε 117
7.17 Deformed model of the simplified joint with the stiffener solution 2 that maximises η 117

B.1 Schematic of the tendon routing ports distributed along the flange pitch circle. 138
B.2 Free body diagram of the joint module showing internal forces and tendon interactions. Tendon-flange interaction forces are shown in red. 139

C.1 Virtual prototype of the linear actuator 144

D.1 Joint 1 tendon tension trends for each F_t setpoint 145
D.2 Joint 2 tendon tension trends for each F_t setpoint 146
D.3 Joint 3 tendon tension trends for each F_t setpoint 146
D.4 Joint 4 tendon tension trends for each F_t setpoint 147
D.5 Joint 5 tendon tension trends for each F_t setpoint 147

LIST OF TABLES

2.1 Research works that present non-T-D actuation solutions 23
2.2 Advantages of T-D RLHRMs and CHRMs 24

3.1 Components within each sub-assembly 29
3.2 DH parameters of the robot. 30

4.1 Summary of data preprocessing parameters and GP performance metrics. 49
4.2 Gaussian Process Model Configuration and Hyperparameters 49

5.1 Target joint positions for the motion test trajectory 65
5.2 Minimum relevant tendon tension during motion phases 67
5.3 Minimum relevant tendon tension during hold phases 68
5.4 Mean deflections (Δz) and their respective uncertainty 80
5.5 Percentage increase in stiffness for each joint and payloads W_1, W_2, W_3. 83

6.1 Performance parameters of the GP model for each robot link 96
6.2 Mass reduction of the robot links after optimisation. 99
6.3 Theoretical and real densities of the printed parts 102

7.1 Physical and mechanical properties of A7075 T6 (Ergal). 109
7.2 Geometric parameters describing the tube-shaped geometry constraints. 112
7.3 Geometric parameters describing the rectangular-shaped geometry constraints. 113
7.4 Summary of the results of the sensitivity analyses for solution 1 and 2. . 118
7.5 End-effector displacement corresponding to the first 118

A.1 Properties of 3D-printed PA 12 136
A.2 Zylon Fibres Material Properties 136

CHAPTER 1

INTRODUCTION

Industrial inspection [1] remains one of the modern domains where human operators are regularly exposed to serious safety risks for routine tasks. Current methodologies rely mostly on human operators entering hazardous, confined, or remote environments to assess structural integrity. This dependence requires extended plant shutdowns and exposes operators to severe health risks, ranging from toxic exposure to physical injury. The challenge is amplified by an ageing infrastructure [2] that operates beyond its initial design life and lacks accessible inspection routes [2]. Unlike the standardised environments, such as in automotive manufacturing, inspection scenarios are mostly unstructured and require highly adaptable solutions. Consequently, removing operators from hazardous zones and drastically reducing production downtime are important objectives. Fulfilling these requirements requires systems that can navigate complex geometries while withstanding harsh environmental conditions.

1.1 MOTIVATION

The transition towards automated inspection and maintenance in industrial sectors is primarily driven by the need to enhance operator safety and reduce plant downtime. While the market has seen a successful deployment of aerial vehicles [3] for large-scale external monitoring and magnetic crawlers [4] for surface-level assessment, a significant technological gap remains regarding the inspection of confined, hazardous, and geometri-

[1] https://www.energy-robotics.com/post/industrial-inspection
[2] https://asi-group.com/
[3] https://www.feds.group/blog/critical-infrastructure-inspections-with-drones
[4] https://nexxis.com/custom-solutions/snowcat-2/

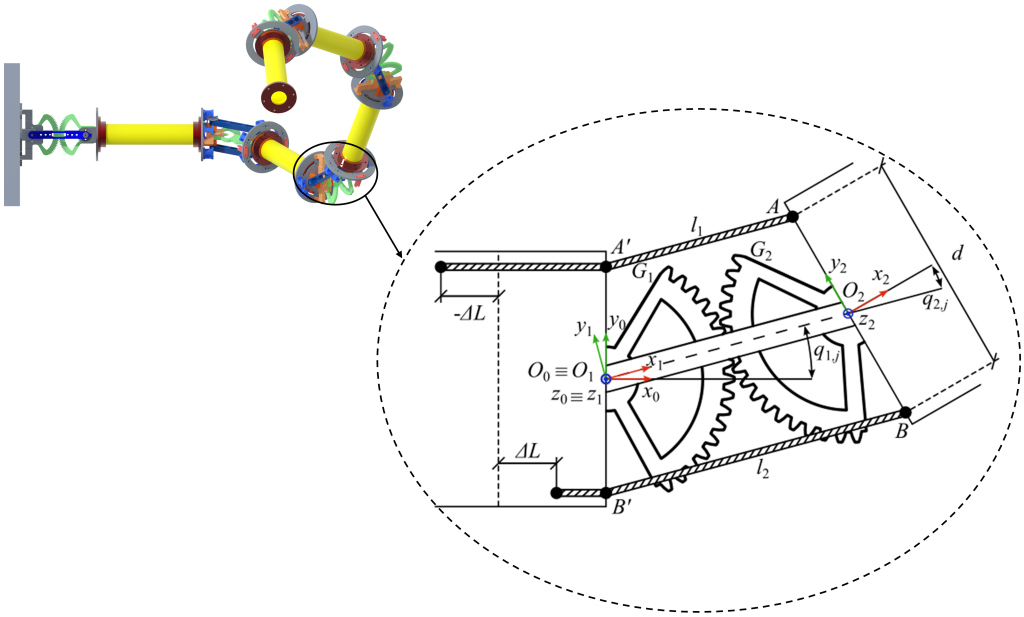


Figure 1.1 Foundational virtual prototype and gear joint geometry

cally complex internal volumes [3]. Traditional rigid manipulators lack the dexterity and manoeuvrability to navigate these complex paths, whereas mobile robots often struggle with vertical traversal in constrained spaces [4]. This operational limitation motivates the focused study of tendon-driven hyper-redundant manipulators; by relocating the actuation hardware to the robot's base, this design not only protects sensitive electronics from potential extreme conditions, such as high temperatures or radiation, but also significantly reduces the moving inertia, obtaining a slender, lightweight design capable of "snake-like" motion. However, the flexibility that makes these systems advantageous introduces significant engineering challenges, specifically regarding non-linear tendon elasticity, stiffness, friction-induced hysteresis, and complex kinematic coupling, necessitating the development of modelling, design and optimisation frameworks to transform these theoretical advantages into reliable industrial solutions.

1.2 Foundational Work

This thesis builds on prior foundational work that established the baseline robotic system and an initial end-to-end design workflow for a Tendon-Driven (TD) Hyper-Redundant (HR) robot for inspection and maintenance, with actuation hardware located outside the hazardous zone and long tendon transmissions delivering motion inside the workspace.

A key design decision was a pulleyless actuation layout with $n_{\text{act}} = n_{\text{DOF}}$, with one motor assigned to one controlled degree of freedom. Each motor drives an antagonistic tendon pair, shortening one tendon while lengthening the other. This choice reduces motor count compared with independent actuation of each tendon, yet imposes a kinematic constraint on joint motion. Standard revolute and universal joints change the total length of an antagonistic pair during rotation, which leads to tension loss unless an additional compensation mechanism is introduced. The previous work, therefore, derived a joint-motion constraint aimed at preserving tendon tension under single-motor antagonistic actuation, which can be expressed as an approximately constant antagonistic sum (figure 1.1):

$$l_1(\boldsymbol{\theta}) + l_2(\boldsymbol{\theta}) = 2L \tag{1.1}$$

with l_1 and l_2 the antagonistic tendon lengths, θ the joint rotation angle, and L the nominal intermediate link length $\overline{O_1O_2}$.

Three modular joint concepts were synthesised around this actuation constraint, a gear-transmission joint, an internal cable-transmission joint, and an articulated joint. After extensive consideration, analysis and experimentation, the gear transmission joint was chosen as the best performing one in terms of force low variations and constant tendon length.

Furthermore, the foundational work developed a model aimed at rapid design exploration and actuator sizing. A preliminary five-module robot served as the reference platform for deriving kinematics, statics, and actuator requirements. Modified Denavit-Hartenberg parameters defined the serial chain [5], and tendon routing was encoded through an routing matrix T describing tendon passage through successive modules. This routing representation allowed to obtain direct and inverse kinematic maps between joint coordinates and actuator coordinates, and led to a compact differential relation between joint velocities and actuator linear velocity:

$$\dot{\mathbf{L}} = \mathbf{J}_\theta(\boldsymbol{\theta}, T)\dot{\boldsymbol{\theta}} \tag{1.2}$$

where $\mathbf{L}$ contains actuator tendon lengths, $\boldsymbol{\theta}$ represents joint coordinates, and $\mathbf{J}_\theta$ is the Jacobian matrix, and it is lower triangular because routing proceeds upstream along the chain.

A complementary static model was developed to compute actuation and internal forces for a given configuration and external loading. The foundational work adopted a Newton-Euler recursion, propagating kinematics forward and solving equilibrium backward

joint-by-joint to obtain antagonistic actuation forces as functions of configuration, routing, tendon pre-tension, and gravity. Two direct design tasks followed. First, pre-tension levels were selected to prevent tendon slack under expected loading. Second, routing sensitivity was quantified using the predicted maximum tendon forces and predicted actuator stroke, showing that routing choice strongly affects both force levels and motion-range.

The robot's performance proved highly sensitive to the specific path the tendons take through the joints. A poor routing choice results in excessive friction or unmanageable actuator demands. To address this, a multi-objective genetic algorithm was applied to the design. This optimisation process identified the ideal internal routing path. It simultaneously minimised the required tendon tension and the travel distance of the linear actuators.

Ball-screw-based linear actuators were proposed to convert motor torque into tendon translation with high axial force capacity. Stroke requirements were derived from the kinematic maps, while force requirements were derived from static predictions and preload constraints.

While the study established the model and theoretical feasibility of the system, it relied on simplified physics. Critical real-world complexities, specifically tendon elasticity, variable friction, and structural compliance, were omitted to maintain computationally manageable simulations. These unmodeled physical phenomena represent the gap between theoretical prediction and physical reality that the current work aims to address.

1.3 Main Contributions of this work

The inherited starting point is based on a model and simulation-validated design, and the focus of this new project is to bridge the gap between the virtual and physical domains. The primary objectives of the work described in this thesis are, therefore, outlined as follows:

- **Chapter 2** provides a comprehensive overview of HR manipulators, categorising them into continuum and rigid-link systems. It analyses existing actuation strategies, with a specific focus on tendon-driven mechanisms, reviewing various architectures and joint designs. The chapter concludes by comparing the trade-offs between continuum and rigid-link designs, identifying the specific need for active tensioning and optimisation in high-payload, slender manipulators for industrial inspection.

- **Chapter 3** presents the physical realisation and validation of a polymeric prototype: design and fabrication of a TD **LO**ng-**R**each h**Y**per-redundant **5**-**J**oint **P**olymeric

(**LORY-5JP**) prototype, using additive manufacturing (PA12/Nylon) with a design for assembly approach to minimise component count and the integration of embedded optical sensors for direct joint-level feedback, while providing a lightweight and slender manipulator. The design process revealed a persistent bottleneck: determining which load combinations were truly critical to structural integrity. Standard worst-case assumptions led to overly conservative designs, especially for joint structures under coupled loading. This highlighted the need for a data-driven method capable of identifying the true worst-case stress configurations from the robot's full actuation space.

- **Chapter 4** formalises this need by introducing a data-driven structural optimisation framework: a Bayesian optimisation method based on Gaussian Process regression to predict worst-case stresses over the robot's full configuration space. This allows efficient identification of critical load cases without computationally expensive Finite Element Analysis (FEA), supporting both mass optimisation of structural components and safety validation of existing physical components. This method reduces the computational cost of FEA, enabling the identification of critical load cases with high confidence via sparse sampling.

- **Chapter 5** addresses the testing and validation of an active tensioning system and a novel tensioning strategy that replaces the previous fixed-preload method. This chapter advances in investigating and accounting for real-world effects, such as friction, tendon elasticity, and hysteresis, as well as tension delivery, through experimental campaigns. Firstly, experiments are conducted on the robot to quantify the tensioning efficiency at rest and in motion, excluding joint configurations associated with maximum stress conditions, as obtained through the method presented in chapter 4. Furthermore, a simple model is developed to link the commanded tension to the minimum delivered tension in the actuating tendons. Finally, this chapter details the experimental characterisation of robot stiffness: a comprehensive experimental analysis quantifying the relationship between global tendon tension and manipulator stiffness. This involved using a high-precision motion capture tracker to measure the robot's pose with high accuracy.

- **Chapter 6** Details the optimisation and design method for **LORY-8JP**, a scaled version of LORY-5JP, retaining the kinematic configuration and joint geometry of the 5-DOF prototype, but with increased length, starting from the optimisation framework presented in chapter 4. The objective is to adapt the manipulator for

a new, challenging operational domain: the development of a customised design methodology for underwater operations, integrating the previously developed optimisation strategy (chapter 4) with generative design to minimise mass and hydrodynamic drag. This includes the formulation of a modular buoyancy strategy using custom-designed buoyant elements to achieve neutral buoyancy, allowing the system to be deployed on standard Remotely Operated Vehicles (ROVs).

- **Chapter 7** advances the transition towards the future metallic version of the robot by addressing a critical limitation identified during the functional testing of the polymeric prototype: torsional deflection under high lateral loads. This chapter details the design and structural analysis of lightweight stiffener elements specifically customised for the robot's base joint, which withstands the highest cumulative torque. Two distinct geometries, compatible with the existing complex routing, joint movement, and available internal space, are evaluated via FEA to optimise the trade-off between stiffness and mass efficiency. This improvement reduces risk for the future metallic prototype, increasing precision performance while preserving the established routing and assembly layout of the polymeric version.

- **Chapter 8** draws the conclusions and future directions.

The research detailed in the subsequent chapters of this thesis systematically addresses the predecessor's proposed future work while introducing significant new contributions. Collectively, these advancements represent the transition from a virtual concept to a physically realised, experimentally validated, and structurally optimised robotic system ready for operational deployment.

CHAPTER 2

STATE OF ART

Hyper-Redundant (HR) manipulators are characterised by having more DOFs than required for a specific task, resulting in high manoeuvrability, similar to that of biological creatures [6–8], and the capability to navigate in unstructured environments. HR manipulators are particularly useful in environments where reach, slenderness, and manoeuvrability are needed, such as inspection and maintenance [1], as well as in medical procedures where high accuracy and operational safety are required [9].

A systematic literature review was conducted and detailed in [10] and [11]. Two main families of these robotic systems are identified: Continuum Hyper-Redundant Manipulators (CHRMs) and Rigid-Link Hyper-Redundant Manipulators (RLHRMs). CHRMs are defined as: *"They do not contain rigid links and identifiable rotational joints. Instead, the structures bend continuously along their length via elastic deformation and produce motion through the generation of smooth curves"* [12]. Conversely, RLHRMs consist of rigid links and identifiable joints, forming non-continuous curvatures.

Within these families, two categories were defined based on the actuation strategy: extrinsic actuation, where actuators are mounted off the robotic arm, and intrinsic actuation, where actuators are mounted directly on the robotic arm. An additional category, hybrid actuation, contains combinations of different strategies. Among the identified actuation solutions, the Tendon-Driven (T-D) strategy, an extrinsic method that relies on tendons for transmission, emerges as the predominant solution, representing approximately 62% of all identified designs. Specifically, T-D solutions account for 44.7% of CHRMs and 75.9% of RLHRMs.

Since this dissertation focuses on T-D manipulators, this chapter presents an extensive analysis of the state of the art of T-D HR manipulators, with T-D CHRMs presented

in Section 2.1 and T-D RLHRMs presented in Section 2.2, while Section 2.3 briefly discusses alternative actuation approaches found in the literature.

2.1 Tendon-Driven Continuum Manipulators

As mentioned, CHRMs do not contain rigid links and identifiable rotational joints. Their structure bends continuously along their length through elastic deformation, producing motion by generating smooth curves. This manipulator family has various structures: flexible backbone structures, origami-inspired or accordion-like shapes, tube-like flexible structures, and other more particular types. Their compliance provides them with grasping capabilities, given their capacity to adapt to objects with different shapes [13, 14]. While having a low payload capacity and accuracy due to their flexibility, they often offer high manoeuvrability. Their inherent compliance results in higher operational safety [15]. Several mechanical elements typical of the CHRMs were identified, and definitions for each of them are provided. The backbone is the frame of the manipulator, which must be able to bend elastically under the effect of the actuation. Its dual function is to house the other components and to act as a compliant element, allowing the actuation of continuum manipulators through elastic deformation. For such purposes, high-flexibility components with a high length-to-cross-sectional area ratio, such as superelastic Nitinol (NiTi) tubes and wires, or silicone tubes, are employed. The tendon is a transmission element that transmits tensile load only, from the drive system to the body of the manipulator. It consists of a cable made from various materials, including steel and nylon. The disc is an element with the dual function of a connection organ and guide for the passage of parts such as tendons, rods or other components. Our definition of discs is not limited to circular plates but includes different-shaped components. A conceptual design of a CHRM is provided in Figure 2.1. T-D CHRMs are actuated by pulling tendons to bend their intrinsically flexible structure. The body structure typically comprises only the tendons, the discs, and one or more backbones. The frame of such robotic arms is generally composed of a central backbone and/or multiple secondary backbones. The discs serve as guiding elements or anchor points for the tendons; in segmented designs, different robot sections can be controlled separately by tendons fixed at intermediate points on the structure. The tendons are usually thin and lightweight, adding negligible weight to the manipulator compared to other transmission elements, such as gears, which allows the robot's mass to be contained. At the same time, they occupy a limited volume within the robot structure, enabling slender designs. Moreover, the tendons are flexible elements and adapt their shape easily to the deformed configurations of CHRMs. However, the tendons

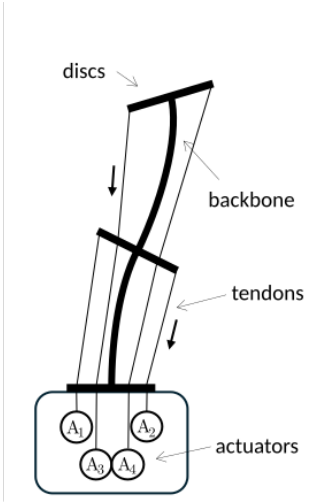


Figure 2.1 A schematic representation of a simple T-D CHRM

introduce friction forces along their routing through the robot's structure, which must be considered in the robotic system's control algorithm. Due to their elasticity, tendons can stretch when subjected to forces, resulting in positioning errors. This necessitates the development of a proper tension compensation system. The tendons can only transmit tensile loads, making it necessary to actuate each robotic arm section with at least two antagonistic tendons. When each tendon is actuated independently, a high number of motors results in segmented designs. This type of actuation is used in various designs of CHRMs, and the backbone element of such a manipulator can comprise different components and materials. In the following, T-D solutions are grouped into subsections that represent the different types of structures identified in the survey, such as CHRMs with NiTi, telescopic, spring, elastic tube backbones, origami-like structures, and soft limbs. The last subsection comprises all works that focus on specific design aspects of T-D manipulators, such as tendon routing, tension loss, and achieving variable stiffness.

2.1.1 NiTi Backbone Manipulators

Nitinol (NiTi) alloy is one of the materials used to make backbones. NiTi can undergo large deformations and return to its original shape, providing flexibility and stiffness. A backbone-based design is proposed by Dai et al. [16], developing a space-grasping system composed of three continuum arms. The robot arms have a central backbone constructed from NiTi alloy, support discs, and driving tendons. Wang et al. [17] proposed a manipulator for the inspection of aero engines in the development of a slender robot

capable of carrying repairing devices. Its structure has two NiTi backbones and discs with twin-pivot revolute joints actuated by stainless steel tendons. The backbones ensure a continuous deformation of the robotic arm, while the discs ensure torsional stability while retaining the flexibility of the structure.

The properties of NiTi enable the creation of a flexible backbone from a single element, simplifying construction and offering good deformation capabilities. However, it is less stiff and withstands lower stresses than other materials used for similar solutions, such as spring steel.

2.1.2 Telescopic Backbone Manipulators

Nguyen et al. [18] developed a T-D manipulator with extensible sections, thanks to a telescopic backbone composed of concentric straight tubes and floating magnetic discs, capable of evenly disposing along the backbone during its elongation and shortening thanks to the mutual magnetic repulsion. This design allows the robot to vary in length, making it suitable for various applications, from medical procedures to search and rescue operations. Zhang et al. [19] also presented a T-D manipulator for neurosurgery with an extensible backbone made of two equally sized tubes, frontal and bottom segments, sliding on a smaller concentric tube, middle segment.

A telescopic backbone can be obtained by combining flexible tubes of different diameters in a concentric configuration. Such a solution introduces the necessity of an actuation strategy for controlling the relative sliding of the tubes. On the other hand, this design solution allows a continuous manipulator of variable length, and the hollow structure of the tubes allows the insertion of tools through the robotic arm. robotic arm.

2.1.3 Spring Backbone Manipulators

Another component used as a backbone is a bar made of spring steel. The planar manipulator built by Gravagne et al. [20] for the study of a large-deflection dynamic model relies on such type of backbone; the arm has four tendons running through equally distanced discs and attached to the end disc. Dumitru et al. [21] designed a trunk comprising a common central elastic spring steel backbone and multiple discs divided into three segments. Also, the manipulator of Lin et al. [22] has a spring steel backbone. The design includes a novel arrangement of tendons and discs to facilitate efficient movement and control.

Spring steel backbones are more rigid and resistant than NiTi ones, providing better stiffness at the cost of inferior flexibility.

Other designs may comprise a series of springs as a backbone. Such a solution is used in the elephant trunk developed by Yang et al. [13], which can continuously bend by pulling the tendons attached to the discs or can also contract by simultaneously pulling all of them, reducing the total length, resulting in a manipulator with grasping capabilities. Mehling et al. [23] designed a manipulator for in-space inspection using a backbone consisting of segments formed by extension and compression springs alternately connected in two pairs, with active and passive bending control functions, respectively.

By combining a series of springs, it is possible to obtain a hollow and flexible backbone with good deformability, capable of varying its total length when the springs are contracted. However, the usage of spring adds the complexity associated with modelling related to the deformation of these elements.

2.1.4 Elastic Tube Backbone Manipulators

A silicone elastic tube can be used as a backbone as well, as in the design of Ye et al. [24]; the robotic arm is divided into segments, each made of a thin and wavy-shaped tube, with a hollow cross-section with enough space for an imaging probe, actuated by two pairs of thin wires. This type of design is suited for Minimally Invasive Surgery (MIS) or other medical applications. Li et al. [25] proposed a manipulator that consists of several identical vertebrae surrounding a backbone made from an elastic tube. An additional rigid or flexible tube is concentrically inserted in the backbone: sliding it inside the backbone reduces the banding segment of the manipulator if rigid or reduces the deformation of the base segment if flexible. The introduction of the translational constraint enhances the ability to follow complex trajectories and workspace of the manipulator, making it a versatile MIS tool. Another MIS instrument, with a tube-like element as a backbone, is proposed by Hu et al. [26]; the endoscope is segmented, with each section composed of an inner structure of discs joined to one another through Universal joints (U-joint) wrapped in a metal mesh that ensures bending stiffness and gives the continuum behaviour.

Elastic tube backbones allow for a hollow structure, which is useful for the insertion of tools, stiffener elements to reduce flexibility, or rigid elements to limit the flexible portion of the manipulator. Moreover, this outer backbone can protect inner components from the external environment.

2.1.5 Origami-Like Manipulators

Alternative designs, distinct from backbone-based ones, are origami-like structures, considered continuum manipulators since they lack identifiable joints and bend continuously.

Origami-like manipulator structures are based on the Japanese art of paper folding and unfolding, known as "Origami". This design is proposed by Santoso et al. [27] and is composed of foldable tube-shaped bodies with triangular sections made of PolyEthylene Terephthalate (PET) material, each segment consisting of a compliant plastic body and an acrylic end disc. A similar design is presented by Zhang et al. [28], in which a spring, acting as a backbone, is inserted between six identical origami-compliant segments. This manipulator can bend in various directions thanks to three actuating tendons, which can also be pulled simultaneously to contract the body of the manipulator. Another similar configuration is introduced by Zhang et al. [29], who developed an accordion-like retractable body structure, which consists of hollow, flexible, worm-like corrugated casings made of thermoplastic polyurethane with three tendons passing through the cable guides made of 3D-printed polylactic acid material and springs as a backbone.

Origami structures are hollow and have inherent variable length. 3D printing of polymeric materials is widely used for producing such robots, allowing the development of lightweight solutions. These designs, however, tend to be bulkier compared to other backbones.

2.1.6 Soft Limbs Manipulators

A soft T-D CHRM for underwater applications is proposed by Emet et al. [14]. The robot, named URSULA, is inspired by squids and includes four soft robotic T-D limbs, a head, a pen, an expandable mantle, a tail, a visible-light communication system, and flexible pectoral fins.

A continuum manipulator designed with soft material favours the compliance of its structure, which is useful for operations such as grasping and palpation.

2.1.7 Other Tendon-Driven Continuum Manipulators

A crucial aspect in designing T-D CHRMs is carefully analysing the tendon routing and configuration. Helical tendon routing is one way to enhance the manoeuvrability and workspace in T-D CHRMs, allowing for more complex shapes and movements. For this purpose, Gao et al. [30] proposed an MIS manipulator with evenly distributed discs with holes and compression helical springs as a backbone and four actuation tendons. The manipulator in this work uses cross-helical tendon routing to achieve omnidirectional S-shapes with only one segment, relying on a single actuation to achieve in-plane bending. It is shown that cross-helical tendon routing offers better manoeuvrability and larger workspace than straight tendons. Helical tendon routing is also considered

by Starke et al. [31], which analysed a multi-segment CHRM and its tendon routing. The study showed that helical tendon routing considerably enhances the workspace and manoeuvrability of continuum robots. Tendon routing in CHRMs can also influence the stiffness, as shown by Oliver et al. [32], who studied how to improve stiffness in T-D manipulators by implementing a non-parallel routing of the tendons.

Tendon routing plays a crucial role in such manipulators, as it influences the workspace and manoeuvrability of the robotic arm, as well as the stiffness and actuation forces.

Cheng et al. [33] offered a unique approach to developing a robust, high-force, and highly articulated manipulator. Such results are achieved by employing a variable stiffness mechanism by jamming granular media actuated by tendons. The manipulator demonstrates a high stiffness-to-weight ratio, enabling it to support weights and manoeuvre in complex environments, and can wrap around objects while maintaining complex shapes. Similarly, Zhao et al. [34] achieved variable stiffness through a unique combination of particle and fibre jamming, allowing the robot to lock its structure into a rigid state or allow flexibility when needed. The robot can adjust its stiffness by controlling the distribution and interaction of the particles and fibres within its structure. The methods mentioned above significantly enhance the adaptability and performance of T-D CHRMs, enabling them to operate effectively in diverse environments that require both flexibility and rigidity.

The material jamming technique achieves continuum T-D HR robots with variable stiffness. On the other hand, such a solution increases the weight of the overall structure and requires additional actuation to achieve the jamming effect.

2.2 Tendon-Driven Rigid-Link Manipulators

RLHRMs are characterised by rigid links of various shapes connected in series by revolute, spherical, prismatic, compliant, or other joint types. They usually have a lower manoeuvrability and motion range than the continuum manipulators due to their non-continuous nature [17]. However, they usually have higher mechanical resistance and structural stiffness, being able to carry a heavier load [15, 35]. This advantage stems from the modular structure, which provides robust structural support and efficient load distribution, allowing it to transport heavier payloads or tools. For this reason, these manipulators excel in tasks that require motion accuracy and payload capacity while manipulating objects with varying shapes and orientations, with precise control of each module's position and orientation [36]. The ease with which the number of modules can be adjusted allows the robot to adapt to the needs of specific tasks or different

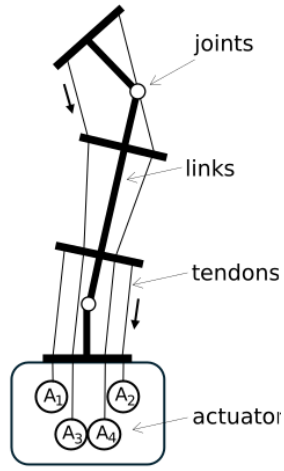


Figure 2.2 A schematic representation of a simple T-D RLHRM

environments, a capability not shared by continuum robots, which are characterised by a continuous, uninterrupted structure, limiting their modularity and adaptability.

The definitions for the mechanical elements specific to RLHRMs are given below. The joint is a connection element that allows relative displacement between the components (e.g. universal or revolute joint). The link is an element that prevents the relative motion of the components connected to it. The tendon and the disc keep the previously provided definition. An example of a T-D RLHRM is provided in Figure 2.2. In the following, T-D RLHRM solutions are grouped into subsections that represent the different types of structures identified in the survey, such as lightweight and long-reach structures, as well as structures with compliant, spring, universal, gear, rolling, and ball joints. The last subsection consists of all the works focused on specific design matters of T-D RLHRM manipulators, such as variable cross-section, tension management, tendon routing, tendon-hole interaction, and achieving variable stiffness.

2.2.1 Lightweight Manipulators

In the design process of RLHRMs, it is essential to keep the rigid links lightweight, maintaining good structural stiffness to increase the maximum payload of the manipulator. Sklyarenko et al. [37] developed a novel lightweight design manipulator named TENDRIM; it comprises three restrained T-D parallel segments, each composed of thin bars mounted in a tetrahedron configuration, appropriately connected with links and bearings to form a movable truss platform with two rotational DOF. The stiffness-to-weight ratio is

also critical in RLHRMs, and structural optimisation of the system is needed to increase it. Al-Khulaidi et al. [38] performed a complex and multi-modal optimisation with the artificial bee colony algorithm to optimise the structure of a manipulator. The optimisation includes adjusting the lengths of the links and the joint angles to minimise errors between the end-effector's actual and desired positions/orientations.

2.2.2 Long-Reach Manipulators

Another advantage of RLHRMs is their potential for long reach. The "Super Dragon" developed by Endo et al. [39] is a 10 m long manipulator designed for decommissioning tasks in nuclear plants. It features seven long cylindrical links, with the proximal four having pitch Revolute joints (R-joints) and the distal three having both yaw and pitch R-joints. Despite its length, the manipulator remains lightweight and capable of handling significant payloads, which is crucial for its intended applications. Another long-reach and slender manipulator has been proposed by Zheng et al. [40]. The robotic arm consists of twelve cylindrical links connected through U-joints. Tang et al. [36] proposed a similar arm design, with twelve cylindrical links connected through U-joints. The manipulator is equipped with a transmission mechanism for tendon tensioning, consisting of a slider fixture linearly actuated by a ball screw connected to the motor. Canali et al. [1] developed a long-reach fully-actuated lightweight manipulator, shown in figure 2.3, which is composed of 12 modules, each consisting of a rigid link and a circular pulley acting as an R-joint driven by tendons. Combined with a strategic choice of materials and a modular design, it provides enhanced reach, manoeuvrability, and operational safety.

By combining rigid elements and tendon transmission, T-D RLHRMs achieve the longest design among HR manipulators. The low weight and encumbrance of the transmission element allow for a high value of slenderness and reduced mass, permitting the design of long robotic arms with satisfying payloads. Long-reach manipulators are highly suited for inspection tasks in hazardous or hard-to-reach environments.

2.2.3 Compliant Joints Manipulators

Another approach to designing a lightweight manipulator is to utilise compliant joints. Chanthasopeephan et al. [41] proposed a robotic arm with modules that utilise compliant joints. The absence of motors on board, combined with the use of flexure-compliant joints and polymeric materials, makes it lightweight. Flexure joints are also used by Jainandunsing et al. [42]: the modules of this manipulator consist of two discs connected by four thin, flexible plates; such a mechanism avoids the friction issues of traditional



Figure 2.3 A long-reach RLHRM prototype [1]

hinge joints. Similar joint types are used in the manipulator for aero-engine maintenance proposed by Dong et al. [43]. A similar use of compliant joints is proposed in the MIS manipulator designed by Wei et al. [44], in which three tendons are used to control the bending of the manipulator. Another RLHRM manipulator with compliant joints developed for aero-engine maintenance is proposed by Yang et al. [45]. T-D structures that contain a series of identical compliant joints can be subject to uneven stress distribution along the robot structure when a variable curvature bending shape is formed, particularly with higher stresses in the compliant joints near the fixation base. To address the issue of uneven stress distribution, Sun et al. [46] proposed a fish-tail-inspired method. This approach optimises the stress distribution along the serial compliant joints of the robot by iteratively modifying their structural parameters based on the biomechanical principles observed in fishtails, starting with a basic structure of discs connected by single thin plates. It is shown that this approach reduces the stress differences in the compliant joints during bending with large deformations. Finally, Liu et al. [47] exploited compliant joints to achieve the development of a T-D manipulator capable of S-shape deformation with a single tendon.

Compliant joints offer lightweight solutions, as they consist of flexible elements. Moreover, since the joint is made of a single element, it has no mechanical play, which provides an advantage in precision. As a drawback, compliant joints have non-linear

behaviour, making it generally necessary to use finite element method analyses to study their deformation.

2.2.4 Spring Joint Manipulators

Another type of flexible joint used in RLHRMs is the spring joint. Such a joint is applied to the manipulators proposed by Li et al. [48], which comprises two segments, each composed of two links connected by helical springs and discs for each link for the passage of tendons. The springs at the distal end are stiffer than those near the base, enabling variable stiffness along the manipulator. A similar manipulator structure is proposed by Choi et al. [49], which designed an endoscope using a helical spring backbone covered by equally spaced aluminium cylindrical links and three tendons for actuation, resulting in a series of rigid link and spring joints.

The principle of spring joints is similar to that of compliant joints, with which they share a lack of mechanical play and light weight. However, unlike a compliant joint, the spring element can be compressed axially, allowing for variable-length design solutions.

2.2.5 U-Joints Manipulators

Many T-D designs are based on U-joints. A manipulator composed of U-joints is the one proposed by Yeshmukhametov et al. [15]. The manipulator is composed of thin links connected by U-joints, combined with helical springs between the links, which offer support and variable stiffness as the arm moves. Further research from the same authors focused on providing this manipulator with a passive pre-tension mechanism, which is then developed to avoid tension loss [50]. The pre-tensioning mechanism consists of compression springs connected to a slider on which the tendons run through pulleys, placed so that the tension of the spring compensates for tensioning losses. A different U-joint design is proposed by Tang et al. [51] for the development of a manipulator for underwater applications. It consists of hollow cylindrical links with small wall thickness, connected by U-joints, and a ring-shaped disc for each joint to allow for tendon passage. Jagadeesan et al. [52] proposed an RLHRM composed of 16 cylindrical links with tendon-passage holes and 15 U-joints. Compression springs are incorporated between each link assembly, aiding the links in restoring them to their original position. U-joints are also used in the manipulator proposed by You et al. [53], consisting of six segments with a total of 18 tendons, with three tendons controlling each segment. A model for studying the friction phenomena is developed, addressing the related critical issue of tension decay in the tendons. Accurately modelling how friction affects the passage of tendons through

the holes provides a more precise understanding of how the tension of the tendons varies throughout the robot. Liu et al. [54] developed an RLHRM with active-passive T-D segments. The manipulator comprises cylindrical links connected by U-joints and a pre-tensioning mechanism. The active tendons control the movement, while the passive ones provide structural support. This design offers a balance between reduced complexity and enhanced stiffness, well-suited for inspection applications. The manipulator developed by Dutta et al. [55] consists of a series of U-joints, each actuated by four tendons and connecting three cylindrical links and a camera as an end-effector. It is designed to inspect the Tokamak nuclear reactor and features enhanced stability and reduced weight. Huang et al. [56] developed a two-segment under-actuated RLHRM with cylindrical discs connected by decoupled U-joints with the two skewed rotational axes. Decoupling the two rotations of the joint by using two R-joints has the advantage of reducing the complexity of the driving mechanism and eliminating tendon slack. Jin et al. [57] developed a robotic arm for MIS applications comprising six links driven by four tendons. Besides having high precision and manoeuvrability, the robust design enables it to handle significant loads while maintaining a slender shape comparable in size to that of a pen, which is beneficial in surgical settings.

U-joints provide two rotational DOF, enabling each segment for spatial movement with a wider workspace to the manipulator and providing valuable stiffness in the constrained directions. On the other hand, they suffer from mechanical play, and if the two rotation axes intersect, they inherently generate tendon slack during the rotation.

2.2.6 Gear Joints Manipulators

Another type of joint that has been studied is the gear coupling. Guardiani et al. [58] presented a fully actuated RLHRM for inspection purposes. During the development process, three different pulleyless joint configurations were analysed: a gear transmission joint, a tendon transmission joint, and an articulated joint. The selection has been based on their performance, specifically their ability to avoid tendon tension loss. The best-performing joint was the gear transmission joint, which was selected to develop a 5-DOF RLHRM. Additionally, a method for optimal tendon routing based on a multi-objective genetic algorithm has been introduced, which can be applied to a generic T-D RLHRM. This study is the foundational work on which this dissertation is based. The manipulator design of the work mentioned above is based on the work of Ludovico et al [59], which presented a bond-graph approach to model T-D joint dynamics, which is a graphical

modelling technique, including a friction model for the interaction of tendons sliding into bushings.

Gear joints provide a valuable alternative to the R-joint. Combined with a rod element in an epicyclic configuration, they are the best at avoiding tendon slack. While offering good precision and reduced mechanical play when well projected, such a solution provides only one rotational DOF, and the joint itself is bulkier than a simpler revolute joint.

2.2.7 Rolling Joint Manipulators

Another joint type is the Rolling Joint (RJ). It consists of two convex rolling surfaces carved into the links, extensively used in manipulators for MIS. Kim et.al. [60] developed a novel MIS T-D RJ manipulator that aims to enhance the workspace of the RLHRM under external load conditions. RJs are also used in the MIS manipulator developed by Dragone et al. [61], actuated by polymethyl methacrylate tendons and with an optical sensing unit embedded into the robot's body. The combination of RJs and T-D actuation can be miniaturised, as shown by the MIS manipulator proposed by Ciurezu et al. [62], which uses 23 vertebrae-like links with curved surfaces to achieve relative rotation through RJs. Kwon et al. [63] designed a MIS manipulator with adjustable stiffness. This MIS manipulator's structure consists of serially stacked rigid links connected by RJs. Between the links, elastic fixtures in the form of flat springs with different thicknesses are placed. These springs play a crucial role in adjusting the stiffness of the joints, thereby affecting the robot's curvature.

RJs allow the minimisation of the structure of RLHRMs, resulting in slender manipulators for MIS with considerable stiffness. While offering similar encumbrance and higher stiffness compared to similar CHRM solutions, it doesn't generally feature a hollow structure and suffers from mechanical play due to undesired sliding between the joints.

A study focusing on improving the performance of the RJ solution by combining it with a gear coupling is carried out by Berthet et al. [64], who developed a 3D-printed MIS manipulator with an optimised RJ solution. This design offers low friction, enhanced joint range, and large force transmission, which is crucial for surgical tasks. Gao et al. [65] developed an MIS manipulator with Engaging Rolling Joints (ERJ) with gear teeth. Another example of geared RJs is presented by Hwang et al. [66], which features gear-transmission RJ, mechanically constraining redundancy with auxiliary elastic fixtures attached to the main links at the centres of the rolling surfaces of two adjacent gears.

The gear teeth enable a more controlled and ideal rolling motion between the joints, preventing mutual slipping under lateral loads.

2.2.8 Spherical Joints Manipulators

A Spherical joint (S-joint) is obtained by pairing a spherical protrusion with a spherical cavity, allowing rotation around three axes of the connected elements. A manipulator for MIS application based on a ball-constrained S-joint is proposed by Ji et al. [67], with the purpose of enhancing accuracy by obtaining constant curvature and increased twist stiffness.

Such a design solution enables the creation of a hollow manipulator with enhanced resistance to twisting deformation, thanks to the ball within the joint and the constant curvature provided by the springs between the segments, resulting in improved accuracy.

2.2.9 Other Tendon-Driven Manipulators

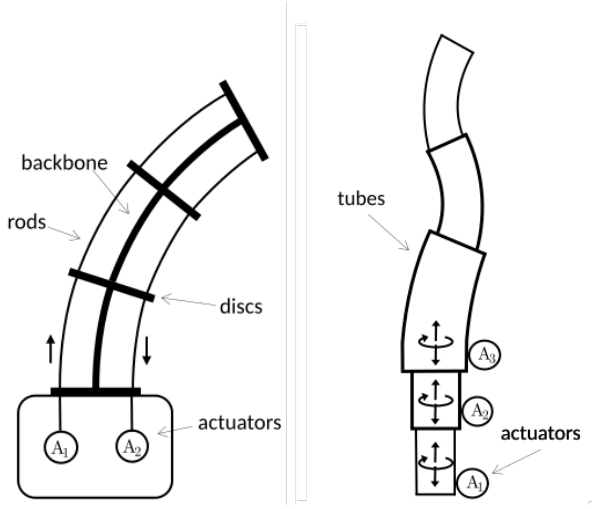
Not having onboard motors allows the development of variable cross-section modules for better manoeuvrability and low weight, as proposed by Qin et al. [68]. The manipulator is inspired by an elephant-trunk structure and comprises five truncated cone-shaped links with decreasing size from the base to the tip, characterised by a decreasing bending radius from the base to the tip of the structure, thereby increasing manoeuvrability and workspace compared to a fixed cross-section structure. Also based on elephant-trunk bionics is the proposed manipulator by Qiang et al. [69], which uses U-joints to connect the links, each actuated by four tendons. Proper tension management is crucial for supporting heavy loads and maintaining structural integrity, as shown by You et al. [70]. The authors designed an RLHRM for MIS applications with RJs and a Σ-shaped tendon path, which consists of a routing with both parallel tendons running on the outer diameter of the arm and skewed tendons that start from the outer diameter of the first links and converge in the tip. This method also increases the overall stiffness of the RJ manipulator. Based on the previous work, Kim et al. [71] developed a MIS manipulator with an almost identical design, slightly changing the Σ-shaped tendon path and enhancing the reinforcement of the RLHRM. T-D systems may suffer from issues like tendon stretch and hysteresis, affecting accuracy and repeatability, which can be improved with the use of a tendon-tensioning mechanism, as analysed by Marais et al. [35] in the design of a robot for confined space inspection. A tensioning mechanism involving tightening bolts that pull on the tendons is developed to maintain the desired tendon tension, thereby improving motion accuracy. Tendon routing is another crucial issue to solve. Wang et al. [72] analysed how tendon

arrangement affects the manipulator's performance and studied the relationship between tendon position, driving force, external force, and joint angles on a model of a manipulator with links connected through U-joints. Li et al. [73] developed an innovative approach for improving the motion accuracy of RLHRMs, studying the tendon-hole interaction. By accurately calculating the tendon hole clearance, the authors addressed a common source of error in tendon length measurement, which, if not corrected, can lead to significant deviations in the manipulator's path and end-effector positioning. While T-D RLHRMs can carry heavier loads compared to CHRMs, the force output may still be limited by the strength and tension capacity of the tendons. However, the load capacity and stiffness can be enhanced with a few improvements, as proposed by Xu et al. [74]. The work presented a tendon tension model based on rigid body static equilibrium principles. It is used to describe the relationship between the manipulator's posture and the tension in its tendons, which can significantly improve the movement accuracy of the manipulator. Jianqing et al. [75] considered the complex coupling among active tendons, passive tendons, joints, and the end-effector, addressing the complex dynamics and stiffness modelling challenges. Another effort is to develop a variable stiffness manipulator using active material embedded in the joints. Diek et al. [76] proposed a 3D-printed RLHRM composed of stiffness-adjustable S-joints. This mechanism allows for selective control in an RLHRM: by immobilising all joints except the one targeted for movement, precise manipulation of a specific joint is achieved. This manipulator can discretely modulate its stiffness, locking and unlocking one or more joints.

2.3 Alternative Actuation Solutions

While tendon-driven systems dominate the field, alternative actuation strategies have been developed to address specific limitations such as stiffness control, miniaturisation, and environmental adaptability. This section explores these alternatives for both CHRMs and RLHRMs. This manipulator family has various structures: flexible backbone structures, origami-inspired or accordion-like shapes, tube-like flexible structures, and other more particular types. An advantage of CHRMs is their inherent compliance, resulting in operational safety, and they are usually smaller and more slender than their rigid-link counterparts [77]. However, they may be prone to high deformations, which can lead to less accurate end-effector positioning. While having a lower payload capacity, they are often able to obtain a low bending radius and high manoeuvrability [78]. In CHRMs, rod-driven and concentric-tube solutions employ extrinsic actuation, while Shape Memory Alloy (SMA), Pneumatic Muscle Actuation (PMA), hydraulic, and magnetic solutions

have intrinsic actuation. The conceptual schematic designs of extrinsically actuated CHRMs are provided in figure 2.4, while figure 2.5 shows the intrinsically actuated CHRMs

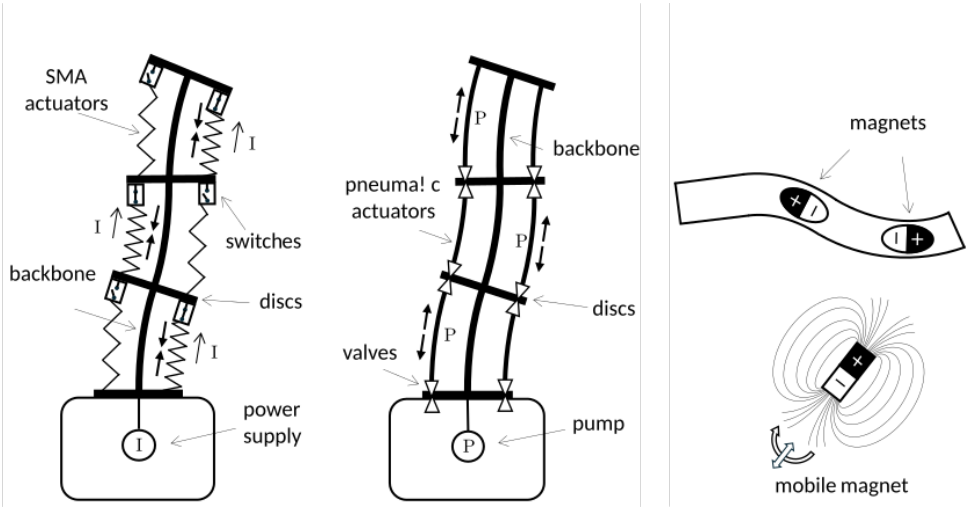


(a) Rod-driven CHRM (b) Concentric-Tube CHRM

Figure 2.4 Conceptual schemes of non-T-D extrinsically actuated CHRMs. In (a), the actuators A_1 and A_2 alternatively push and pull the respective rods that pass through each disc and are attached to the final one, deforming the backbone; in (b), the actuators A_1, A_2, A_3 actuate the respective tube in two directions, in extension and in rotation, flexing the manipulator by combining the pre-deformations of the tubes

The identified RLHRMs with alternative actuation solutions include linear actuation, gear actuation, magnetic actuation, direct tendon actuation, servo actuation, and SMA actuation. Schematic representations of these design solutions are shown in figure 2.6. As mentioned in [10], they usually have a lower manoeuvrability and motion range than the continuum manipulators due to their non-continuous nature [17]. However, they usually have higher mechanical resistance and structural stiffness, being able to carry heavier loads [15]. This advantage stems from the modular structure, which provides robust structural support and efficient load distribution, allowing it to transport heavier payloads or tools. For that reason, these manipulators excel in tasks requiring motion accuracy and payload capacity while manipulating objects with varying shapes and orientations [79].

Table 2.1 presents the alternative actuation solutions found in the literature for each mentioned category. The detailed analysis is presented in [11].



(a) SMA Actuation CHRM (b) Hydraulic/Pneumatic Actuation CHRM (c) Magnetic Actuation CHRM

Figure 2.5 Conceptual schemes of non-T-D intrinsically actuated CHRMs. In (a) the power supply *I* provides the current necessary for the activation of the SMA actuators, which can be individually switched on, deforming the backbone; in (b) the pump/compressor *P* provides the on-board hydraulic/pneumatic actuators with the pressurised fluid; the actuators of each segment can be individually activated through valves by allowing the passage of fluid, deforming the backbone; in (c) an external mobile magnet generates a variable magnetic field, inducing the internal magnets, oppositely polarised, to change their orientation, deflecting the manipulator

Category	Reference
Rod-Driven	[80] [81] [82] [83] [84] [85]
Concentric-Tube	[86] [87] [88]
SMA Actuation	[89] [90] [91] [92] [93]
PMA	[94] [95] [96] [97] [98] [99]
Hydraulic Actuation	[100] [101]
Magnetic Actuation	[102] [103]
Servo Actuation	[104] [105] [106] [107] [7] [108] [9] [109]
Hybrid Actuation	[110] [111] [112] [113] [114] [115] [116] [117]

Table 2.1 Research works that present non-T-D actuation solutions

2.4 Design Considerations for Hyper-Redundant Manipulators

The state-of-the-art analysis highlights a distinct trade-off in the design of HR manipulators. A summary of the advantages of RLHRMs and CHRMs is presented in table 2.2 RLHRMs are generally preferred for applications that require precision, high stiffness,

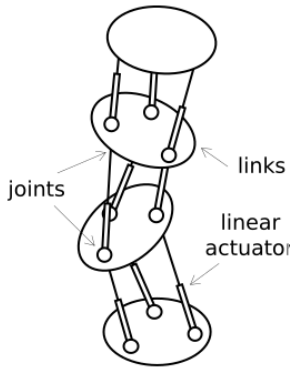
RLHRMs	**CHRMs**
Good Precision	High Flexibility
High Payload	Small size
High Stiffness	Good Maneuverability
Long reach	Inherent compliance

Table 2.2 Advantages of T-D RLHRMs and CHRMs

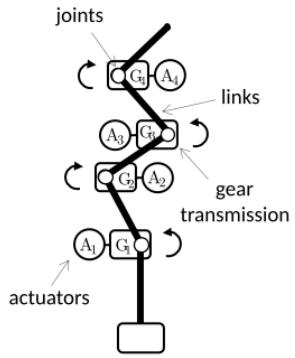
and heavy payloads, such as industrial inspections. In contrast, CHRMs excel in manoeuvrability and inherent compliance, making them ideal for medical applications and tasks requiring safe interaction.

Regarding actuation, T-D solutions represent the majority of designs because they successfully decouple actuator weight from the arm, enabling the long, slender, and lightweight structures required for hyper-redundancy. However, the implementation of T-D systems introduces significant challenges that remain active areas of research, and some form the basis for this thesis. There is a clear need for active tensioning strategies that dynamically adjust tendon tension, removing slack and adjusting stiffness and positioning accuracy. Furthermore, unmodeled phenomena such as friction distribution, cable elasticity, and hysteresis necessitate physical validation and estimation through prototypes. Finally, the structural optimisation of mass and volume, as well as adaptation to specific applications, remains a challenge.

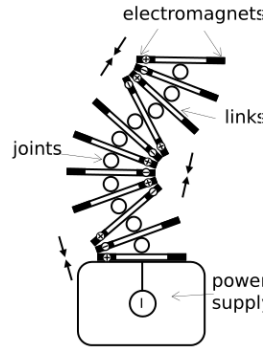
Alternative actuation strategies solve specific subsets of these issues, such as stiffness or compliance, but often at the cost of increased bulkiness or reduced controllability. Consequently, this thesis focuses on advancing Tendon-Driven RLHRMs, exploiting their superior payload-to-weight ratio while explicitly addressing their primary weaknesses through novel design, actuation, and optimisation.



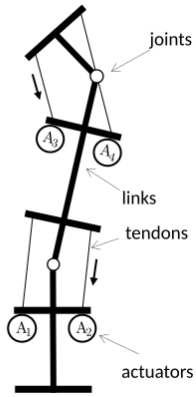
(a) Parallel Mechanism



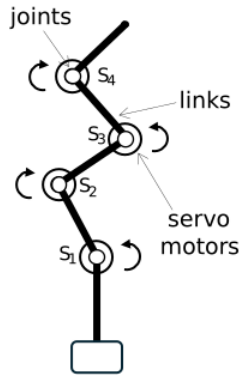
(b) Gear Transmission



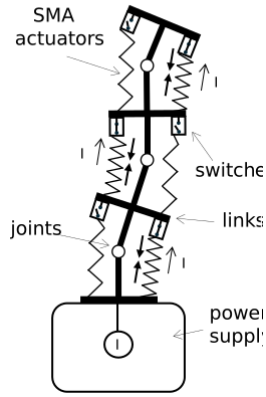
(c) Magnetic Actuation



(d) Direct-Tendon



(e) Servo Actuation



(f) SMA Actuation

Figure 2.6 Conceptual schemes of intrinsically actuated non-T-D RLHRMs. In (a), each module is a parallel mechanism with three linear actuators connected to the lower and upper discs by U-joints or spherical joints; in (b), each joint has a gear mechanism (G) coupled to an actuator (A), allowing individual joint rotation; in (c) the power supply I provides the necessary current for the electromagnetic actuators; each subsequent pair of electromagnets can be individually switched on, rotating the joints; in (d) the two revolute joints are actuated through a pair of antagonist tendons, each of them attached to one of the on-board actuators (A_1, A_2, A_3 and A_4); in (e) each joint is coupled to a servo motor (S), allowing individual joint rotation; in (f) the power supply I provides the current necessary for the activation of the SMA actuators, which can be individually switched on, rotating the joints

CHAPTER 3

LORY-5JP DESIGN AND IMPLEMENTATION

This chapter presents the polymeric prototype *LORY-5JP*, which is the main experimental platform developed in this thesis to study long tendon transmissions under realistic operating conditions. The prototype comprises $n = 5$ serial modules for a total length of $L = 1$ m, is designed to minimise size while preserving structural integrity, and is manufactured by Selective Laser Sintering (SLS) in PA12 (Nylon).

The design builds upon the kinematic architecture and tendon-routing principles established in previous work (Appendix B and [118, 58]). In particular, each module employs a gear-based joint with tendon-driven actuation and off-board motors while keeping the joint compact. The foundational joint architecture relies on an internal transmission constraint with an effective transmission ratio $\tau = 2$, which motivates modelling each physical module as two coupled internal rotations, named $q_{1,j}$ and $q_{2,j}$, shown in the previous work and in Chapter 1. This reflects the gear-joint kinematics, in which the internal rotations are not independent, and the output joint motion follows a fixed gear coupling.

The objective of this prototype is twofold. First, it provides a small-sized and lightweight design that supports repeatability and scaling towards a future metallic version intended for field deployment. Second, it serves as an experimental platform for the actuation and active tensioning system analysed in the following chapters, where tendon friction, elasticity, and slack become measurable system-level effects.

The following sections detail the design methodology and manufacturing constraints, the tendon routing and its structural implications, the embedded sensing, and the distributed SPI architecture used for joint-angle acquisition.

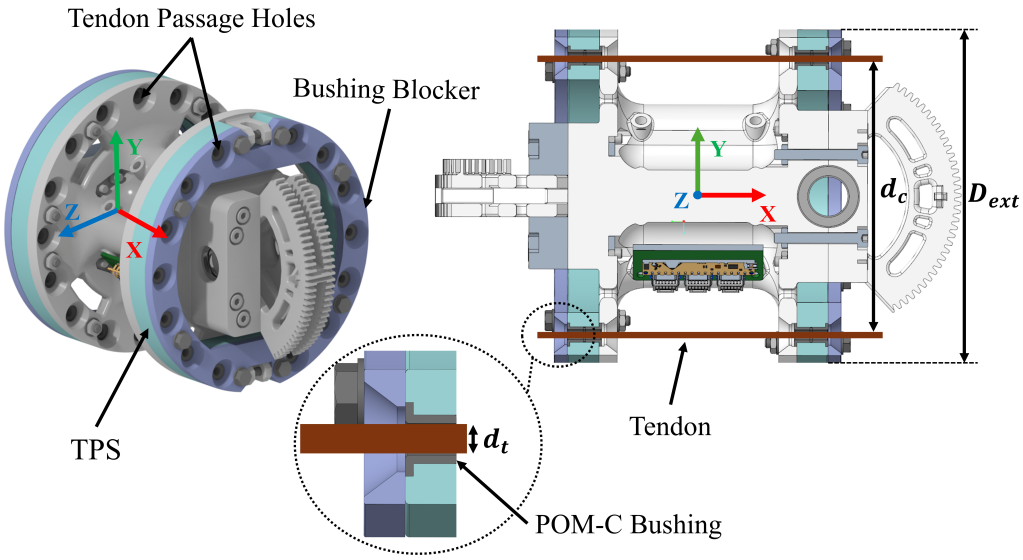


Figure 3.1 Rendered picture of a robot link representing the TPS, flanges, tendon anchoring pins, and tendon-passage holes.

3.1 LORY-5JP Design Methodology

LORY-5JP is a modular TD HR manipulator developed as an experimental platform for tension-transfer characterisation, active tensioning, and stiffness regulation. The prototype uses five identical modules to simplify fabrication, assembly, and repeatable testing. Despite the reduced number of modules, the mechanical layout of each module is dimensioned to remain compatible with the longer target design (LORY-8JP), in which the same module is replicated to increase reach without redesigning the joint internals or tendon routing.

All the mentioned geometric parameters and component names in this section are shown in figure 3.1.

The outer diameter D_{ext} is driven by tendon routing requirements and by the internal packaging of joint components. A TD serial chain requires multiple tendons to pass through proximal modules, and the proximal tendon passage must be sized to handle the maximum number of tendons specified by the scalable design. As the number of modules increases, the number of routed tendons increases accordingly, imposing a minimum circumference for tendon passage. The tendons pass through a structural element referred to as Tendon Passage Support (TPS), defined as the ring-shaped component hosting the tendon passage holes and setting the tendon pitch circle around the joint, as shown in figure 3.1.

Four aspects set the minimum allowable tendon passage circumference d_c: (i) the tendon passage hole diameter d_t, (ii) a minimum wall thickness between adjacent holes to limit stress concentration in the TPS, (iii) space for low-friction bushings and their retention features, (iv) a minimum free inner volume for the joint internal components.

In this design, the tendon passage hole diameter is set to $d_t = 4$ mm to match the bushing inner diameter and to remain compatible with SLS manufacturing tolerances. Hole spacing is constrained by the local stresses generated in the TPS during joint rotation. A dedicated structural analysis of the TPS and tendon-hole loading is reported in the following section, and is used to verify the selected hole spacing and safety margin. In parallel, the inner volume enclosed by the TPS must contain shafts, bearings, rods, gears, and joint rotation-sensing elements. Considering $d_c = 115$ mm and the space allocation for the internal components, the minimum module outer diameter obtained is $D_{ext} = 130$ mm.

The mechanical structure is designed around Design for Assembly (DfA) principles to reduce part count and allow precise assembly. Selective Laser Sintering (SLS) in PA12 (Nylon) is selected for rapid prototyping and to integrate features that would otherwise require multi-part machining and alignment. This approach allows monolithic 3D-printed components with integrated routing, mounts, and pre-aligned reference features, reducing the need for fasteners and manual adjustment.

Nylon is selected due to its mechanical resistance, enabling repeated mechanical testing without brittle failure. The actuation tendons are made of Zylon (PBO)[1] fibres, selected for high tensile strength and stiffness. Material properties of Nylon and Zylon fibres are reported in Appendix A. To reduce friction and wear at the tendon interfaces, Acetal resin (POM-C) bushings are inserted into the flanges and tendon passage holes.

Each module is composed of two functional sub-assemblies: a joint sub-assembly responsible for the transmission and rotation, and a link sub-assembly responsible for tendon guidance and structural continuity between joints. Table 3.1 reports the components within each sub-assembly, which can be visualised in figure 3.2. Figure 3.2 shows a rendered view of one module and the corresponding exploded views, highlighting the integration of tendon routing elements, joint transmission components, and embedded electronics.

For completeness, the kinematic model of the manipulator is defined through the DH parameters reported in Table 3.2. Each physical joint module is represented in the DH chain as two consecutive revolute rotations, identified as joint i and joint i_c, with

[1] https://www.toyobo-global.com/seihin/kc/pbo/

Joint Sub-Assembly	Link Sub-Assembly
2 Shafts [1]	Link + 2 Flanges + 2 Gears [6]
2 Rods (intermediate link) [2]	2 TPS [7]
4 Bearings [3]	36 Bushings for tendon passage [8]
2 Torsional stiffeners [4]	2 Bushing blockers [9]
1 Sensor [5]	4 Bearing supports [10]
	1 Microcontroller [11]

Table 3.1 Components within each sub-assembly. The numbers in square brackets represent the component reference number for visualisation in figure 3.2.

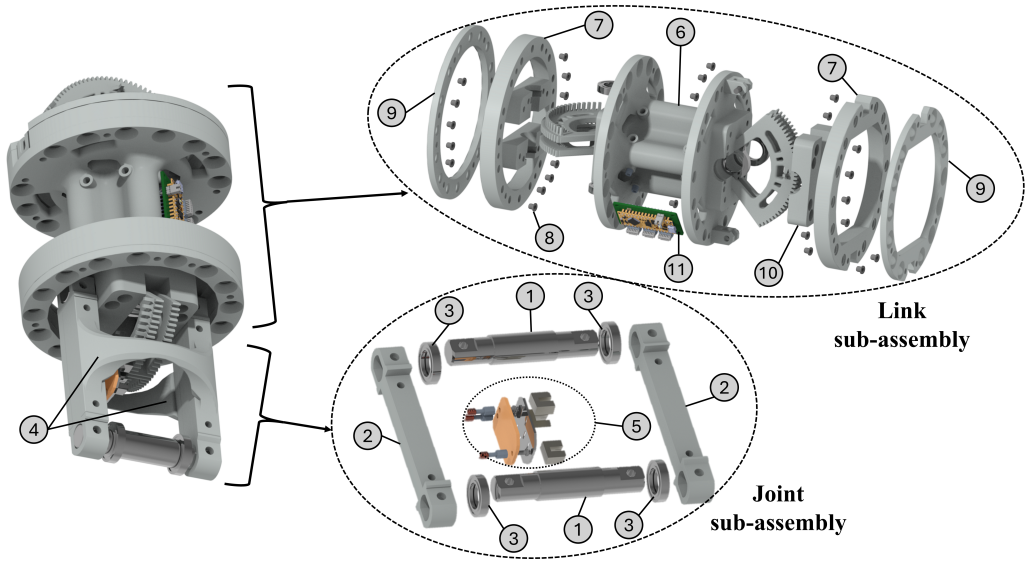


Figure 3.2 Rendered representation of a single module from the virtual prototype, along with exploded views of its sub-assemblies and their individual components.

Joint	$\boldsymbol{a}$ [mm]	$\boldsymbol{\alpha}$ [rad]	$\boldsymbol{d}$ [mm]	$\boldsymbol{\theta}$ [deg]
1	0	$\pi/2$	0	$q_{1,1}$
1_c	100	0	0	$q_{2,1}$
2	100	$-\pi/2$	0	$q_{1,2}$
2_c	100	0	0	$q_{2,2}$
3	100	$\pi/2$	0	$q_{1,3}$
3_c	100	0	0	$q_{2,3}$
4	100	$-\pi/2$	0	$q_{1,4}$
4_c	100	0	0	$q_{2,4}$
5	100	$\pi/2$	0	$q_{1,5}$
5_c	100	0	0	$q_{2,5}$
EE	100	0	0	0

Table 3.2 DH parameters of the robot.

associated variables $q_{1,j}$ and $q_{2,j}$. Since the two internal rotations are mechanically coupled by the gear mechanism, the effective joint coordinate used in the rest of this thesis is treated as a single rotation variable per module.

Considering the DH parameters presented in table 3.2 and the design considerations, the final virtual prototype of LORY-5JP is shown in figure 3.3. Each joint rotates around its local Z axis, allowing to achieve 3D movements in space by combining joint rotations.

The design choices reported in this section define the mechanical structure and the system's integration approach for the subsequent chapters. Section 3.2 details the tendon passage design and verifies the TPS mechanical limits under worst-case tendon loading.

3.2 Tendon Routing

Long tendon transmissions require a repeatable and low-friction tendon path through each module. The tendon routing must satisfy three constraints. First, every tendon that drives a distal joint has to pass through the proximal modules; as a result, the tendon passage in the proximal section must be sized to carry the complete set of tendons. Second, the tendon path should remain close to the ideal kinematic routing to limit positioning errors and tension loss caused by geometric offsets. Third, contact friction at each passage interface must be minimised to reduce force dissipation and wear and maintain consistent tension transfer.

The module geometry is dimensioned to remain compatible with the scalable design (LORY-8JP). For an n-joint TD arm, $2n$ tendons run along the structure (one antagonistic pair per joint). Consequently, the first module directs the largest number of tendons.

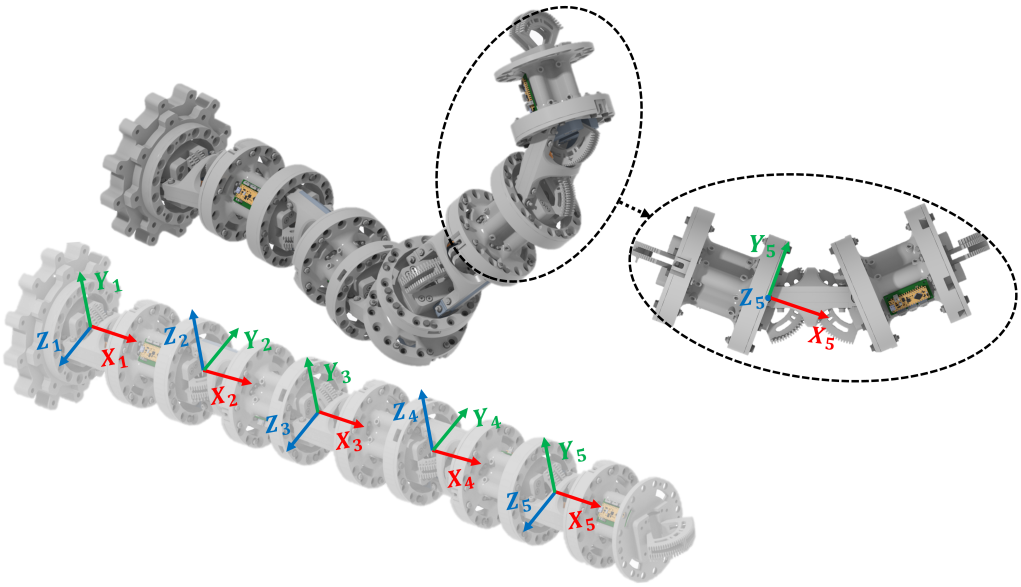


Figure 3.3 Virtual prototype of $LORY-5JP$ with all its components assembled. The rendered picture shows the robot's local coordinate frames and a random configuration in space.

In the present prototype (LORY-5JP), this corresponds to 10 routed tendons, while the extended LORY-8JP layout would route 16 tendons. This scalability requirement sets a lower bound on the tendon passage circumference and therefore contributes to the selected module outer diameter D_{ext} introduced in the previous section.

Each tendon passes through a dedicated hole in the TPS and link flanges. The passage diameter is selected to satisfy assembly feasibility and low sliding resistance while keeping clearance limited. A small clearance reduces deviations from the ideal tendon path during joint rotation and limits local slack at the tendon passage interface. In this design, the passage diameter is set to $d_t = 4$ mm to match the bushing inner diameter. Despite the low-friction bushings, residual friction remains due to tendon curvature and normal contact forces at the passage interface. Minimising clearance is nevertheless preferred because it limits tendon lateral motion inside the passage hole, keeping the effective routing path closer to the nominal geometry and improving repeatability.

Hole spacing on the TPS is limited by stress concentrations around adjacent passage holes, which increase as the holes move closer together. A structural analysis is performed using the maximum tendon force expected at the first joint, then applied to all passage holes simultaneously to obtain a conservative upper bound. This loading assumption overestimates the real distribution because distal joints experience lower tendon forces. The worst-case orientation is evaluated at a joint angle of 45°, where the lateral component

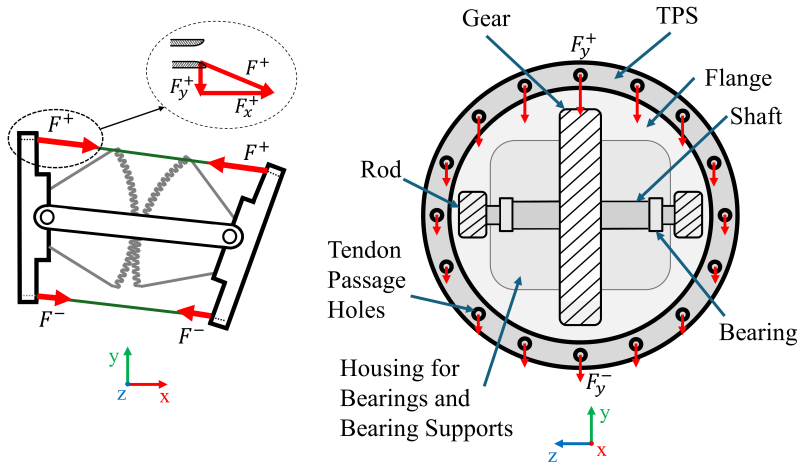


Figure 3.4 Tendon passage through the joint. On the left, tendons exert forces within the passage holes as the joint rotates. On the right, the joint inner components are shown together with the force directions (red) applied to the TPS during rotation.

of the tendon load acting on the hole surface is maximised. Under these assumptions, the maximum equivalent Von Mises stress at the TPS is 32.9 MPa, which remains well below the material limit when compared with the tensile strength of PA12. Figure 3.4 illustrates the tendon force directions and the TPS loading mechanism.

3.3 Sensor Integration

The sensor used for the joint rotation is a *TCST*1300 [2] compact transmissive, through-beam optical sensor that integrates an infrared (IR) light-emitting diode (LED) and a phototransistor detector in a single package. In its internal structure, the IR emitter and phototransistor are arranged face-to-face along a common optical axis, with a gap between them through which an opaque object can pass. When a pin enters the gap, it interrupts the IR beam between the emitter and detector; the phototransistor switches state in response to the beam being blocked or clear, creating a binary optical switch. This type of sensor is small and reliable. The overall package is small (approximately $11.9 \times 6.3 \times 10.8$ *mm*), making it suitable for tight fitting inside a robot joint. The optical gap between the LED and phototransistor is 3.1 *mm*, allowing clearance for small pins to pass through. In the *TCST*1300 variant, the active optical slit is only 0.25 *mm*. This narrow gap defines the sensor's sensing zone with high spatial precision. Electrically, the *TCST*1300 behaves like a digital optical switch. These features make the *TCST*1300

[2] https://www.vishay.com/

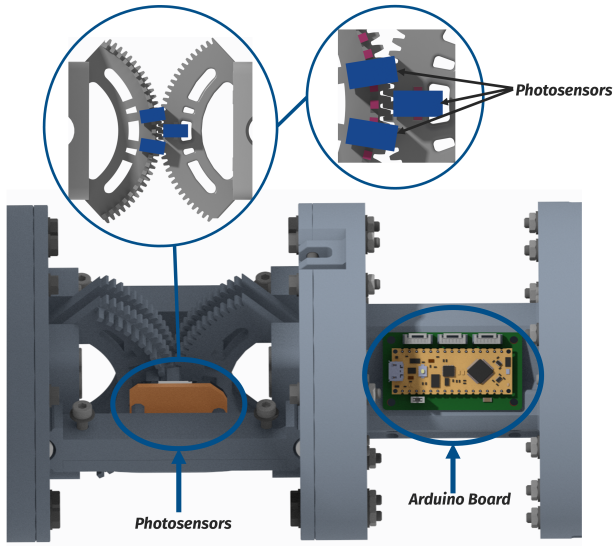


Figure 3.5 Implementation of the sensors into the joint module

particularly well-suited for detecting gear pins on a rotating gear. In the robot joints, each joint has a gear with 2 *mm* square extruded pins on its side. Two *TCST*1300 modules are mounted facing the gear, forming the two channels of a quadrature encoder. As the internal gear turns, its pins alternately break the IR beam of each sensor, producing two pulse trains that are offset in phase. A single reference pin is placed on the external gear; a third sensor is aligned with this pin to generate a pulse once per revolution. The internal gear and its pins serve as an indexed wheel for incremental sensing, while the index pin provides a zero reference and rotation direction. The output is a clean binary waveform corresponding to the presence or absence of a pin. This signal is fed directly into the Arduino [3] Nano board. The sensor is connected to a digital input pin with a pull-up resistor, providing discrete HIGH/LOW readings.

Figure 3.5 shows how the sensors and the microcontroller are implemented into the joint module.

3.4 Distributed SPI Daisy-Chain Control Logic

The distributed control architecture for LORY-5JP employs a daisy-chained Serial Peripheral Interface (SPI) bus to synchronise data acquisition from photodiode sensors at each joint. This design minimises wiring complexity while allowing coordinated readings from

[3]https://www.arduino.cc/

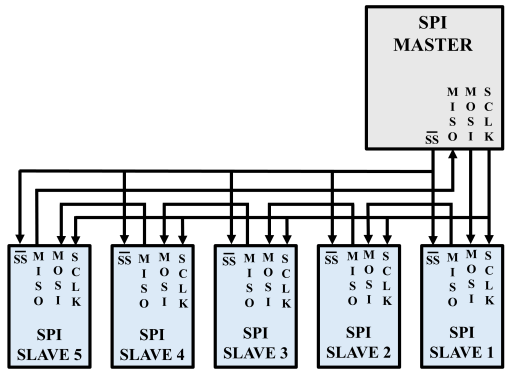


Figure 3.6 SPI wiring scheme

all eight sensors. An NI *Compact*RIO [4] (cRIO) acts as the SPI master, serially connecting to five Arduino Nano boards, each of which is attached to an optical sensor.

Each Arduino Nano on each joint interfaces its photosensor output using an analogue input and converts it into a digital signal. A shared SPI structure carries digital data between the cRIO and the Arduinos. The structure comprises:

- **Serial Clock (SCLK)**: driven by the cRIO at a programmable rate, here set to 1 MHz. Rising edges shift one bit of data; falling edges may also register data depending on the clock phase.
- **Master-Out, Slave-In (MOSI)**: the cRIO outputs on MOSI to introduce configuration and dummy bytes into the chain. Each Arduino samples this line into its SPI Data Register (SPDR) each time the clock signal changes from one logic level to another (rising or falling edge of the signal).
- **Master-In, Slave-Out (MISO)**: each Arduino drives MISO based on its SPDR output. Through software shift logic, data from downstream Arduinos goes back to the cRIO.
- **Slave Select (SS)**: a single line held low to "wake" all Arduinos into SPI transfer mode. Its activation starts the SPI shift registers on every Arduino simultaneously. When SS is set to low, the Arduinos are ready to communicate; when high, all Arduinos stop communicating.

Figure 3.6 details the wiring scheme. Downstream propagation on MOSI follows the labelling chain: cRio $\rightarrow$ Slave 1 $\rightarrow$ Slave 2 $\rightarrow$ ... $\rightarrow$ Slave 5. Upstream on MISO

[4] https://www.ni.com/

reverses: Slave 5 $\rightarrow$ ... $\rightarrow$ Slave 1 $\rightarrow$ cRIO. Each Nano's MOSI-in pin ties to the previous device's MOSI-out. Likewise, MOSI-out pins feed the next device's MOSI-in. MISO signals mirror this arrangement in reverse. All grounds are common, and 5 V is supplied to each Arduino from a regulated bus.

This chapter defined the mechanical structure and routing constraints of LORY-5JP, establishing the physical configuration and the tendon transmission used throughout this dissertation. The next step is to ensure structural safety under all plausible loading conditions. Chapter 4 addresses this by identifying worst-case load combinations using a data-driven approach coupled to FEA.

3.5 Design Challenges and Limitations

During the design of LORY-5JP, one of the critical challenges was determining the load conditions under which structural components would be dimensioned. Several robot elements, such as rods and tendon anchors, are subjected to clearly defined uniaxial loads under predictable worst-case conditions (e.g., maximum axial tendon tension and maximum axial reaction force). The maximum values of these loads can be directly inferred from the statics model (Appendix B) under the payload and gravity. However, for other elements, particularly the link structure and load-transfer interfaces, the load state emerges from a complex combination of forces and moments whose simultaneous interactions are not trivial to resolve.

In initial design stages, a conservative approach was adopted: each load component (reaction forces R_x, R_y, R_z and joint torques M_x, M_y) was individually maximised using statics simulations (according to the model in Appendix B). The maximum value of each component was then assumed to occur simultaneously and used as input for the link mass optimisation in the CAD software. While this strategy guarantees safety, it results in excessive overdesign. The robot's actuation space imposes physical coupling between loads: reaction forces and moments depend on joint angles, payload pose, and routing interactions. As a result, load components are not independent. Their feasible combinations lie on a constrained, nonlinear hypersurface in load space, and not all combinations of maxima can occur simultaneously. When multiple loads act together, their effects on stress can counteract each other. For instance, axial force may reduce stress caused by bending or torsion, depending on direction and location. This means the highest stress may occur under complex load combinations, not simply at the maximum of each load. Furthermore, the robot configuration that generates a simultaneous combination

of all maximum loads might not even be feasible. This means that the joint would be reinforced against non-physical load combinations that never occur in practice.

This mismatch between physical reality and design input results in a wasteful structure, where mass is added to prevent hypothetical worst-case combinations. This way, the actual worst-case stress configuration (i.e., the true combination of loads that maximises stress in a given region) is not being determined. Without this information, both mass reduction and structural validation are limited.

To overcome this, a method was required to efficiently identify the true worst-case load configuration. Such a method must:

- Explore the full 5D load space (forces and moments) without assuming independence between load components.
- Account for the real structural response (stress) of the joint elements.
- Be efficient, avoiding computationally expensive search over all robot configurations.
- Be applicable to both pre-design (for optimising a new geometry) and post-design (for verifying the safety of an existing design).

The data-driven approach described in Chapter 4 was developed to address this need. It provides a systematic, efficient way to search for the worst-case stress under load uncertainty. Rather than treating each load independently, it models the stress function $f(\mathbf{x})$ over the 5D load space $\mathscr{X}$, and uses Bayesian Optimisation combined with Gaussian Process regression to predict high-stress regions and manage sampling. This allows finding the most critical configurations without testing every pose. Furthermore, the same tool can not only be used for design optimisation but also adapted to find safe operating regions in the actuation space, as in Chapter 5.

Although LORY-5JP was already fabricated by the time this method was developed, the process validates and strengthens its structural design. In particular, it shows which regions are unsafe, informs future design iterations, and provides a solid base for scaling (e.g., LORY-8JP).

CHAPTER 4

BAYESIAN OPTIMISATION OF WORST-CASE LOADS

Structural design optimisation aims to use minimal material while meeting performance constraints, resulting in lightweight, strong structures [119]. Common approaches include topology optimisation to distribute material within a domain, and shape/size optimisation for components. Classical gradient-based methods provide efficient solutions for convex or small-scale problems, but they struggle with high-dimensional or nonconvex design spaces. Evolutionary and heuristic algorithms are widely used for global searches in such complex spaces, but they often require many function evaluations [120]. More recently, machine–learning surrogate models and hybrid methods have been introduced to predict performance and to accelerate optimisation by reducing the number of simulation runs. These advances have enabled practical optimisation in engineering domains such as aerospace, automotive, and civil structures, balancing objectives like weight minimisation, strength, and sustainability [121, 119].

In robotic and multibody system design, optimisation must account for coupled dynamics, kinematics, and control. Multibody components can be optimised using system-level approaches: a dynamic multibody simulation provides realistic loads and motions, and a level set of each component is optimised via gradient-based methods under these conditions [122].

Bayesian optimisation (BO) is a gradient-free, probabilistic framework for optimising expensive black-box functions. BO builds a surrogate model, typically a Gaussian Process (GP), of the unknown objective and iteratively refines it by sampling promising designs [123]. Because GPs quantify uncertainty, BO can strategically propose samples that either improve the best-known solution or reduce uncertainty around high-variance

regions. This makes BO especially useful when each evaluation (e.g. FEA or dynamic simulation) is costly or noisy.

In recent years, BO and GP surrogates have been successfully applied to structural and robotic design. For instance, Tran et al. [124] used BO to drive a moving-morphable-bar topology optimisation, finding better solutions than gradient-based methods in highly nonlinear design spaces while requiring fewer analyses. In robotics, BO has been used for co-design of mechanics and behavior [125].

Compared to traditional optimisation, BO/GP methods achieve high sample efficiency and global search capability. They model the objective as a stochastic function, greatly reducing the number of expensive simulations needed [126], and have the ability to handle high-dimensional optimisation problems by using Gaussian process priors [127]. For example, BO-based topology optimisation consistently outperforms genetic algorithms and particle swarm optimisation in both solution quality and the number of analyses required [128, 129]. BO's probabilistic surrogate can also avoid getting trapped in local minima, handling multimodal or non-smooth objectives that confound gradient methods [130].

Bayesian Optimisation with Gaussian Processes is a state-of-the-art approach: it learns a predictive model of performance, adapts sampling, and has demonstrated superior performance and efficiency on expensive-to-evaluate black-box functions.

4.1 Mechanical Context and Problem Formulation

In structural engineering, each load case can vary in magnitude, direction, and probability, affecting the structure's stress, strain, and deformation differently. Considering all relevant load cases is important for preventing overdesign and underdesign, ensuring the structure meets safety standards without unnecessary material use. With hundreds or thousands of load scenarios, or in the case of serial robotic systems, ∞^n, where n represents the number of joints, each load combination can lead to different structural responses, especially when considering nonlinear, dynamic, or stochastic behaviours influenced by material properties, geometrical factors or mechanism configurations. Traditional optimisation approaches often struggle to manage this level of complexity because each evaluation requires substantial computational time and resources, particularly when FEA is involved; this motivates the method proposed here.

4.1.1 Robot worst-case stress objective

The robotic system examined is the LORY-5JP manipulator. Each manipulator configuration, defined by joint angles $\mathbf{q} = [q_1, \ldots, q_5]$, produces a unique set of internal loads on the structure. In particular, a given robot configuration in space induces reaction loads at the base link, represented as a 5-dimensional load vector:

$$\mathbf{x} \;=\; [M_x, M_y, R_x, R_y, R_z] \tag{4.1}$$

where M_x and M_y are the moments in the X and Y direction, respectively, while R_x, R_y, and R_z represent the reaction forces in the X, Y, and Z directions. The moment M_z is near zero since, as mentioned in Chapter 3, the robot joints rotate around their local z axis, so almost no reaction torque is generated along this axis. These loads generate structural stress in the base link. The component of interest is the first link of LORY-5JP. Each load vector $\mathbf{x}$ is applied to the link through the same boundary conditions used in the structural simulations (fixed base interface and applied forces/moments at the joint interface). The scalar output of interest y is the peak Von Mises stress in the component of interest under that load state. The engineering goal is to find the load combination $\mathbf{x}$ (equivalently, worst-case robot configuration) that maximises this peak stress. The objective is to identify the load vector within the feasible load domain that maximises the peak stress. Let $\mathscr{X} \subset \mathbb{R}^5$ denote the feasible set of allowable load vectors, defined by lower and upper bounds derived from the statics analysis, detailed in Appendix B. The worst-case load is defined as:

$$\mathbf{x}^\star \in \arg\max_{\mathbf{x}\in\mathscr{X}} f(\mathbf{x}) \tag{4.2}$$

where $\mathbf{x}^\star$ denotes the load combination that produces the maximum peak Von Mises stress, and the objective function is $f(\mathbf{x}) = \sigma_{\mathrm{VM}}(\mathbf{x})$, which is the maximum Von Mises stress predicted by structural analysis under a load vector $\mathbf{x}$: The optimisation target becomes identifying the load combination that maximises σ_{VM} over the feasible load domain.

This corresponds to the maximum structural stress the manipulator can experience under static loading, a critical scenario for design verification. Identifying this worst case is essential for guaranteeing the robot's structural integrity under all poses and load conditions.

4.1.2 BLACK-BOX OPTIMISATION SETTING

Several factors make this an especially challenging optimisation task. First, the manipulator has a continuum of possible poses, so the space of loads $\mathbf{X}$ is also continuous and high-dimensional. Brute-force simulation of random poses using FEA over a 5D load hyper-box is impractical. Furthermore, deriving a closed-form analytical model is insufficient for this application because such methods rely on simplified geometric assumptions and linear elasticity, which fail to grasp the non-linear material behaviour of nylon and the critical stress concentrations that occur within complex geometries. While FEA is necessary to resolve this, simulating the infinite configuration space of a manipulator is computationally prohibitive. This requires a surrogate modelling approach, where Bayesian Optimisation (BO) with Gaussian Processes (GP) offers an advantage over alternatives such as neural networks, which require large datasets [131]. This setup is a classic expensive black-box optimisation problem: the mapping $\mathbf{x} \mapsto \sigma_{VM}$ is not known in closed form and can only be obtained by running a detailed simulation.

BO is well-suited for scenarios involving expensive and unknown objective functions. BO methods utilise a data-driven surrogate model of the objective and an acquisition strategy to select new sample points, thus balancing the exploration of unknown regions and the exploitation of high-performing regions [132]. Compared to uniform grid sampling or purely random search, BO can reach near-optimal values with far fewer function evaluations [133]. In this application, a GP regression model is employed as the surrogate for the stress function $f(\mathbf{x})$. The BO loop alternates between (i) fitting or updating the GP on available data, (ii) using an acquisition function (Expected Improvement) to propose the next load vectors to evaluate, and (iii) validating those proposals with the FEA solver, which provides new stress data to refine the model. This closed loop repeats until a suitable stopping criterion is met, e.g. when the model's predictions are sufficiently accurate, or the improvement becomes negligible. The ultimate objective is to converge to the maximum stress and identify the corresponding worst-case load configuration, with high confidence, in as few FEA calls as possible.

4.1.3 LOAD BOUNDS AND FEASIBLE DOMAIN

Each component of $\mathbf{x}$ is bounded between a lower and upper limit derived from the robot's static analysis presented in Appendix B. In this case study, the bending moments M_x, M_y at the base were bounded on the order of $\pm(35\text{-}46)$ Nm, while the axial and shear forces ranged up to order 10^3 N. The outcome of this static analysis is a bound on each load

component, defining the domain $\mathscr{X} = \{\mathbf{x} \in \mathbb{R}^5 : \ell_j \leq x_j \leq u_j\}$, with $j = 1, \ldots, 5$. This domain $\mathscr{X}$ provides the search space for the optimisation.

4.2 Data Preparation and Scaling

4.2.1 Initial training dataset

Before fitting a machine learning model, it is critical to preprocess the data into a suitable numerical form. The initial training dataset $D_0 = (\mathbf{x}_i, y_i)$, with $i \in [1, n_0]$, is obtained by sampling a number of representative manipulator configurations q_i, computing their corresponding load vectors $x_i = S(q_i)$ using the statics model $S(\cdot)$, and running an FEA simulation to obtain the peak Von Mises (VM) stress $y_i = \sigma_{\max}^{VM}(x_i)$. In this case, $x_i \in \mathbb{R}^5$ represents the five load components as described, and $y_i \in \mathbb{R}$ is the scalar stress result. These raw data can have widely varying scales and units, e.g. bending moments in Nm vs. forces in N, and stresses in MPa. Features with large numerical ranges would numerically dominate those with smaller ranges if left unscaled, which can restrict the training process. Likewise, the output stress values might cover several orders of magnitude or have an arbitrary offset, which could slow the convergence of the model. For these reasons, a standard normalisation of inputs and outputs was performed prior to modelling.

4.2.2 Normalisation of inputs, outputs, and bounds

A per-feature z-score standardisation was applied to each input dimension, and a global standardisation to the output. Let $\mu_X \in \mathbb{R}^5$ and $\sigma_X \in \mathbb{R}^5$ be the mean and standard deviation of the input vectors in D_0, and μ_y, σ_y be the mean and standard deviation of the output stresses in D_0. The data is transformed as:

$$\tilde{x} = \operatorname{diag}(\sigma_X)^{-1}(x - \mu_X) \tag{4.3}$$

$$\tilde{y} = \frac{y - \mu_y}{\sigma_y} \tag{4.4}$$

This standardises every feature and the output to a zero mean and unit variance. All 5 inputs and the output are therefore on a common scale. The bounds of the search space are also transformed accordingly: if ℓ and u are the physical lower/upper bounds for the

load vector, then in the normalised space it is used:

$$\tilde{\ell} = \mathrm{diag}(\sigma_X)^{-1}(\ell - \mu_X) \tag{4.5}$$

$$\tilde{u} = \mathrm{diag}(\sigma_X)^{-1}(u - \mu_X) \tag{4.6}$$

This guarantees the optimisation is performed on a nicely scaled domain $[\tilde{\ell}, \tilde{u}]$ in $\mathbb{R}^5$. Clearly, after the GP model is trained and predictions in the normalised output scale are obtained, the results are always mapped back to physical units for interpretation.

4.3 Gaussian Process Surrogate Model

4.3.1 GP prior, mean function, and kernel

GPs are a flexible class of non-parametric models that define a distribution over functions, providing both predictions and uncertainty estimates [134]. It is assumed that the stress function $f : \mathbb{R}^5 \to \mathbb{R}$ is a sample from a GP prior, and that the observations are noisy samples of this function. Mathematically:

$$f \sim \mathcal{GP}(m,k), \quad y = f(\mathbf{x}) + \varepsilon, \quad \varepsilon \sim \mathcal{N}(0, \sigma_n^2) \tag{4.7}$$

Here $m(\mathbf{x})$ is the mean function, prior mean of f at input $\mathbf{x}$, and $k(\mathbf{x}, \mathbf{x}')$ is the covariance function (kernel), evaluated between two load vectors $\mathbf{x}$ and $\mathbf{x}'$ in the same input space. A constant mean $m(\mathbf{x}) = \beta$ is chosen, reflecting an unbiased prior with an unknown constant offset that will be learned from data. The kernel encodes prior assumptions about the function's smoothness and variation. For this application, an Automatic Relevance Determination (ARD) Matérn 5/2 covariance function was used. The ARD Matérn-5/2 kernel is defined as [135]:

$$k(x,x') = \sigma_f^2 \left(1 + \sqrt{5}r + \frac{5}{3}r^2\right) \exp\left(-\sqrt{5}, r\right), \qquad r = \sqrt{\sum_{j=1}^{5} \frac{(x_j - x'_j)^2}{\lambda_j^2}} \tag{4.8}$$

This kernel has the following hyperparameters: a length-scale λ_j for each input dimension and an overall signal variance σ_f^2. The sensitivity of the function to changes in input dimension j is controlled by λ_j: a small λ_j means $f(x)$ can vary rapidly, which means that the feature is relevant to predictions, whereas a large λ_j implies $f(x)$ varies slowly with x, indicating a feature possibly less influential. The Matérn-$5/2$ form is a popular choice in engineering design and BO because it produces sample functions that are

twice differentiable, hence moderately smooth but not overly smooth [136]. In contrast, the ubiquitous squared-exponential (RBF) kernel assumes infinite differentiability, very smooth functions, which may be too restrictive if the true stress response has sharp changes. The Matérn family includes a parameter ν controlling smoothness; $\nu = 5/2$ gives a smoother process than Matérn-$3/2$ or $1/2$, but less smooth than the RBF (which is equivalent to Matérn-$\nu \to \infty$). This makes the Matérn-$5/2$ kernel robust to modest fluctuations in the underlying function, which is appropriate here since the stress response may not be perfectly smooth over the load space; for example, small discontinuities or nonlinear jumps could appear. ARD further provides interpretability: after training, the relative magnitudes of λ_j indicate which load components have the most significant effect on stress, with shorter length scales meaning greater relevance.

4.3.2 Hyperparameter learning via marginal likelihood

The Gaussian prior with the chosen $m(\mathbf{x})$ and $k(\mathbf{x},\mathbf{x}')$ implies that, before seeing any data, any collection of function values $(f(\mathbf{x}^{(1)}),\dots,f(\mathbf{x}^{(n)}))$ has a joint multivariate normal distribution. Once observations are included, the GP posterior will also be Gaussian and can be obtained in closed form. The hyperparameters $\theta = \beta, \sigma_f^2, \lambda_1, \dots, \lambda_5, \sigma_n^2$ are not fixed a priori; they are determined from the data by maximising the Log Marginal Likelihood (LML) on the training set. The LML, also known as evidence, for observations $(\tilde{X}, \tilde{y})$ in the normalised space is:

$$L(\theta) = -\frac{1}{2}(\tilde{y}-\beta)^\top K_\theta^{-1}(\tilde{y}-\beta) - \frac{1}{2}\log\left|K_\theta\right| - \frac{n}{2}\log(2\pi) \tag{4.9}$$

$$K_\theta = K_f + \sigma_n^2 I \tag{4.10}$$

where K_f is the $n \times n$ kernel matrix of all training points, with entries $[K_f]_{ij} = k(\tilde{x}_i, \tilde{x}_j)$. $L(\theta)$ is optimised with respect to θ to find a set of hyperparameters that best explains the data. This procedure is known as a type-II maximum likelihood estimation or evidence maximisation for the GP [137]. The first term in 4.9 measures the model's ability to fit the training data. A better fit gives a higher value. The $\log|K_\theta|$ term acts as a penalty for making the model too complex. If the model is too flexible and tries to follow every small detail in the data, this term increases, discouraging overfitting. Thus, maximising $L(\theta)$, the GP finds a good trade-off between accuracy and simplicity, fitting the data well without becoming too sensitive to noise. Once this optimisation is done, a fully trained GP model is obtained, and can be used to make predictions.

4.3.3 Posterior prediction and uncertainty

Once the GP is trained, the predictive distribution at a new candidate load vector $\tilde{\mathbf{x}}_* \in \mathbb{R}^5$ is Gaussian with mean μ_* and variance σ_*^2. The posterior mean and variance are given by:

$$\mu_* = \beta + \mathbf{k}_*^\top K_\theta^{-1}(\tilde{\mathbf{y}} - \beta \mathbf{1}) \tag{4.11}$$

$$\sigma_*^2 = k(\tilde{\mathbf{x}}_*, \tilde{\mathbf{x}}_*) - \mathbf{k}_*^\top K_\theta^{-1} \mathbf{k}_* \tag{4.12}$$

where $K_\theta \in \mathbb{R}^{n \times n}$ is the kernel matrix of the training inputs with noise on the diagonal, $[K_\theta]_{ij} = k(\tilde{\mathbf{x}}_i, \tilde{\mathbf{x}}_j) + \sigma_n^2 \delta_{ij}$, $\tilde{\mathbf{y}} = [\tilde{y}_1, \ldots, \tilde{y}_n]^\top$, and $\mathbf{k}_* \in \mathbb{R}^n$ is the kernel vector between each training point and the new point:

$$\mathbf{k}_* = \left[k(\tilde{\mathbf{x}}_1, \tilde{\mathbf{x}}_*), \ldots, k(\tilde{\mathbf{x}}_n, \tilde{\mathbf{x}}_*) \right]^\top \tag{4.13}$$

Equation 4.11 shows that the predicted mean is a linear combination of observed residuals $(\tilde{y}_i - \beta)$, weighted by their covariance with $\mathbf{x}$; thus predictions interpolate the data and extrapolate in between. Equation 4.12 also shows that the predictive variance is the prior variance at x_* minus the amount explained by the data; it will be small near training points and larger in unexplored regions. As mentioned earlier, (μ, σ) is then converted back to physical units $(\hat{y}, \hat{\sigma})$. The GP not only provides an estimate of the peak stress at any load, but also a quantitative uncertainty of that estimate. This uncertainty will be essential for informing the BO, as it is preferred to sample where the GP is unsure, as that might hide a higher stress than currently predicted.

4.3.4 Computational considerations and model choice

It is worth noting the computational complexity of GP modelling. GP training and inference scale cubically $O(n^3)$ in the number of training points n, due to the inversion of the $n \times n$ kernel (covariance) matrix, and quadratically in memory $O(n^2)$. In practice, this limits exact GPs to a few thousand data points on a single machine before computations become impractical. In the structural stress application, the number of afforded FEA samples is relatively small; initial data plus iterative additions, usually n in the low hundreds at most, so an exact GP is feasible. This surrogate will form the core of the Bayesian optimisation loop, as it enables the computation of an acquisition function that determines where to sample next, without actually running the FEA at every candidate point.

If the true stress function had strong non-stationarities or varying smoothness in different regions, more advanced models like Deep GPs, multiple GP layers that can learn input warpings, could be considered [138].

4.4 Bayesian Optimization

4.4.1 Acquisition function: Expected Improvement

With a trained GP model for $f(\mathbf{x})$, BO proceeds by repeatedly asking: "Where should we sample the FEA simulation next to discover higher stress?" BO addresses this by using an acquisition function $\alpha(x)$ that quantifies the utility of sampling any given point x, based on the model's current predictions. The acquisition function is designed to balance exploration, by sampling regions where model uncertainty is high, and exploitation, by sampling regions where the model's mean prediction is high. This balance is important: if it only exploits, it risks getting stuck in a local optimum and missing the true worst-case scenario; if it only explores, evaluations are wasted in areas that may not induce higher stress than what was already observed.

For the maximisation problem, the Expected Improvement (EI) acquisition function was employed, a widely used choice in BO [139]. At any iteration, let f_{best} be the current best observed value of the stress in the normalised scale, i.e. the maximum $y^{\sim}$ among all evaluated points so far. For a candidate x, the improvement would be $(f(x) - f_{\text{best}})^+$, where $(z)^+ = \max(z, 0)$. Since $f(x)$ is a random variable under the GP, the Expected Improvement (EI) can be written in closed form as:

$$\text{EI}(x) = \mathbb{E}\left[(f(x) - f_{\text{best}})^+\right] = (\mu_* - f_{\text{best}})\,\Phi(Z) + \sigma_*\,\phi(Z), \tag{4.14}$$

where:

$$Z = \frac{\mu_* - f_{\text{best}}}{\sigma_*} \tag{4.15}$$

and $(z)^+ = \max(z, 0)$. Here $\mu_* = \mathbb{E}[f(x)]$ and $\sigma_* = \text{Std}[f(x)]$ are the GP predictive mean and standard deviation at x, while $\phi(Z)$ and $\Phi(Z)$ are the standard normal probability density and cumulative distribution functions. EI increases when the predicted mean is high or when uncertainty is high, thus balancing sampling in promising regions and reducing uncertainty in unexplored regions. The EI expression contains two contributions. The factor $\Phi(Z)$ represents the probability of improving over the current best observation f_{best}, since Z measures how far the predicted mean is above f_{best} in units of the predictive

standard deviation. The term $(\mu_* - f_{\text{best}})\Phi(Z)$ represents the expected improvement when the mean prediction is already above the current best. The term $\sigma_*\phi(Z)$ represents the contribution of uncertainty, since large σ_* can lead to improvement even when $\mu_* < f_{\text{best}}$. As a result, EI favours points with either high predicted stress (exploitation) or high uncertainty (exploration), providing an automatic trade-off between the two without requiring an explicit exploration parameter.

4.4.2 Batch Bayesian optimisation with q-EI

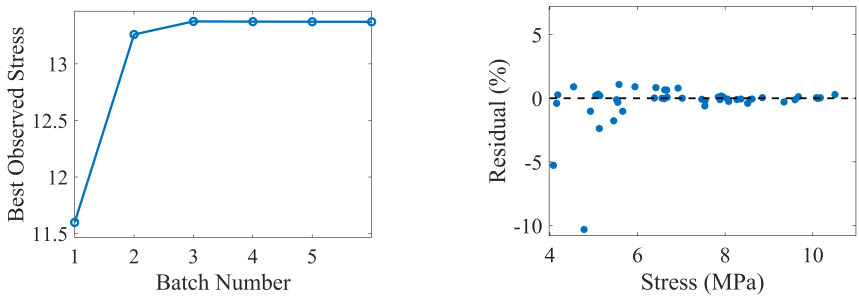
To identify the worst-case stress configuration, a batch BO strategy was employed using a GP model and an EI acquisition function. Rather than querying one load at a time, a set of q points $X_{\text{batch}} = x^{(1)}, x^{(2)}, \ldots, x^{(q)}$ was selected to evaluate in parallel. The batch EI (q-EI) acquisition function is defined as the EI obtained by evaluating all q points collectively. Formally, for a batch X_{batch}:

$$\alpha_{\text{qEI}}(X_{\text{batch}}) = \mathbb{E}\left[\max\left(0, \max_{i=1,\ldots,q}\left(f(x^{(i)}) - f_{\text{best}}\right)\right)\right] \tag{4.16}$$

This is the expected increase in the best-observed stress after simultaneously sampling the set X_{batch}. The q-EI criterion evaluates the joint distribution of $(f(x^{(1)}), \ldots, f(x^{(q)}))$ under the GP, so that the q points are chosen together to maximise their collective expected improvement. In effect, the acquisition function accounts for correlations between points in the batch and rewards by selecting a diverse set of points that maximally explores high-stress regions of the input space. All q proposed load configurations are run in the same finite element simulation, generating q new observations per iteration.

Computing q-EI for $q > 1$ is challenging because there is no closed-form expression for the expectation of the maximum of q correlated outcomes. In the current implementation, a model utilising Monte Carlo simulation was employed to approximate $\alpha_{\text{qEI}}(X_{\text{batch}})$. Essentially, the GP posterior is sampled repeatedly to estimate the expected improvement of a given batch. An inner optimisation loop, using a multi-start gradient-based method, is then employed to find the optimal batch X^*_{batch} that maximises the q-EI acquisition over the domain. This produces q promising load points to evaluate next. These are chosen such that each point targets a high predicted stress region, an uncertain region, or both.

After proposing a batch, all q load configurations are evaluated through the FEA solver. The resulting stress values $y^{(1)}, \ldots, y^{(q)}$ are the true outputs for those inputs. Then these new data points are included in the dataset, and the GP model is updated, refitting the model to include the new observations. In this closed-loop manner, the BO alternates



(a) BO optimisation convergence

(b) Residuals vs. Stress

Figure 4.1 Model performance plots

between surrogate modelling & acquisition optimisation, and evaluations on the FEA solver. With each iteration, the GP model becomes more accurate in the high-stress regions, and the value of f_{best} increases. This process continues until a stopping criterion is met. One convenient convergence test is to monitor the GP's prediction error on newly acquired points, to verify whether the model accurately predicts the FEA results. For example, if the maximum relative error on the last batch is below a tolerance τ, then further exploration is unlikely to deliver significantly higher stresses. At that point, the algorithm terminates, returning the highest observed stress and the corresponding load configuration as the solution.

4.4.3 Model Performance Evaluation

The model was trained and evaluated in the context of a case study focused on the first link of the LORY-5JP manipulator. Since this prototype was designed to withstand future higher stresses from the addition of modules (LORY-8JP) and the high tension forces generated by the tensioner during testing (Chapter 5), the links are significantly overdesigned. For this reason, the stress values are very low on this component. Nevertheless, it serves as a validation platform for this optimisation method. An initial dataset of 200 load configurations was used to fit the GP model. Subsequently, the model was refined over 6 BO iterations. The final model's performance was assessed on a separate test set of 50 previously unseen load cases. Over the course of 6 BO batches, the model progressively predicts higher stress configurations, as shown in Figure 4.1a.

Figure 4.1b shows the residuals, revealing no significant bias and a slight underprediction tendency in lower-stress regions, which decreases in higher-stress regions. This trend is mainly statistical rather than physical. All stresses lie within the linear elastic

range of $PA12$, so the slightly larger residuals at lower stresses are derived from the BO sampling strategy, which concentrates training points and, therefore, model accuracy in the high-stress region. As a result, the GP fit is intentionally prioritised near maxima, where decision quality matters most for worst-case identification. The Relative Error (ε), the Root Mean Squared Error (RMSE), the Mean Absolute Error (MAE) and the Determination Coefficient (R^2) are calculated and defined as:

$$\varepsilon_{\text{rel}} = \frac{|y_{\text{pred,i}} - y_{\text{test,i}}|}{y_{\text{test,i}}} \times 100\%$$

$$\text{RMSE} = \sqrt{\frac{1}{n}\sum_{i=1}^{n}(y_{\text{test},i} - y_{\text{pred},i})^2}$$

$$\text{MAE} = \frac{1}{n}\sum_{i=1}^{n}\left|y_{\text{test},i} - y_{\text{pred},i}\right|$$

$$R^2 = 1 - \frac{\sum_{i=1}^{n}(y_{\text{test},i} - y_{\text{pred},i})^2}{\sum_{i=1}^{n}(y_{\text{test},i} - \bar{y}_{\text{test}})^2}$$

where n is the total number of samples, $y_{\text{test},i}$ is the actual observed value for the ith point in the test set, $y_{\text{pred},i}$ is the predicted value for the ith data point in the test set, and $\bar{y}_{\text{test}}$ is the mean of the actual values in the test set. Quantitatively, the model achieved good metrics, as shown in Table 4.1. Relative errors are significantly low, with a mean of only 0.95% and a maximum of 10.3%, confirming the model's suitability for guiding the FEA-based stress optimisation process. Table 4.2 presents the GP model configuration parameters and hyperparameters, all reported in the normalised input space defined by Eq. 4.3. The key learned hyperparameters include a low noise variance, indicating high confidence, and different ARD length scales for each input. These length scales provide insight into the relative sensitivity of the output to changes in each input direction.

This chapter presented a computationally efficient technique for identifying worst-case load combinations for a manipulator component using a limited number of FEA evaluations. The key output is the best-observed stress value and its associated load vector $\mathbf{x}^\star$, which provides a conservative upper bound within the feasible load envelope $\mathscr{X}$. These results provide a quantitative reference for the stress levels expected under high-load conditions, which is used to define safe experimental payloads and tension ranges.

In fact, the same BO-GP framework can be applied directly in configuration space by setting the input as $\mathbf{q}$ and the output as the corresponding peak stress $\sigma_{\max}^{VM}(\mathbf{q})$. This allows

Metric / Parameter	**Value**
Preprocessing Configuration	
Input Features	5
Training Samples	200
Total BO Samples	260
Standardization Method	Standard Scaler
Output Mean (before scaling)	7.11 MPa
Output Std Deviation (before scaling)	1.78 MPa
Model Performance (Test Set)	
MAE	0.05 MPa
RMSE	0.14 MPa
Mean ε	0.95%
Maximum ε	10.3%
R^2	0.993

Table 4.1 Summary of data preprocessing parameters and GP performance metrics.

Component	**Value**
Noise Variance (σ^2)	1.0×10^{-4}
Output Scale	0.62
Mean Constant	1.28
Lengthscales (per input feature)	
Features 1 to 5	3.80 - 1.03 - 3.74 - 2.17 - 2.90
Lengthscale Mean	2.73
Lengthscale Std Dev	1.04
MLL Optimizer	L-BFGS-B (BoTorch)

Table 4.2 Gaussian Process Model Configuration and Hyperparameters

direct identification of worst-case robot configurations with an available configuration-to-stress dataset. In Chapter 5, this method is used to obtain exactly that, by simply training the model on a dataset made of joint angles (with each combination giving a specific robot configuration) instead of loads, and stresses obtained by each specific robot configuration.

This optimisation framework focuses on peak Von Mises stress as the scalar objective; therefore, other failure types (fatigue, wear, or local contact damage) are outside the scope of this work.

CHAPTER 5

TENDON TENSIONING, SYSTEM VALIDATION AND STIFFNESS CONTROL

Chapters 3 and 4 established the physical system (LORY-5JP) and a method to analyse worst-case structural loading. The next limiting factor is tendon transmission itself. In long routings, friction, elasticity, and slack degrade the delivered tension along the arm, leading to reduced trajectory-tracking performance and lower reliability of tension-prediction models.

This chapter introduces and validates an active global tensioning system that maintains a guaranteed minimum tension along the tendon routing during static loading and motion. The chapter first presents the actuation and tensioning concept, then quantifies tension-transfer efficiency and hysteresis through rigorous experiments, and finally demonstrates how a single global tension input modifies the manipulator's stiffness. These outcomes provide reference performance trends for consideration of future adaptations of TD HR systems.

5.1 TENSIONING SYSTEM

The LORY-5JP manipulator prototype and its actuation unit, which includes the tensioning system, are visualised in figure 5.1. Actuation hardware specifics and motor control details are reported in Appendix C.

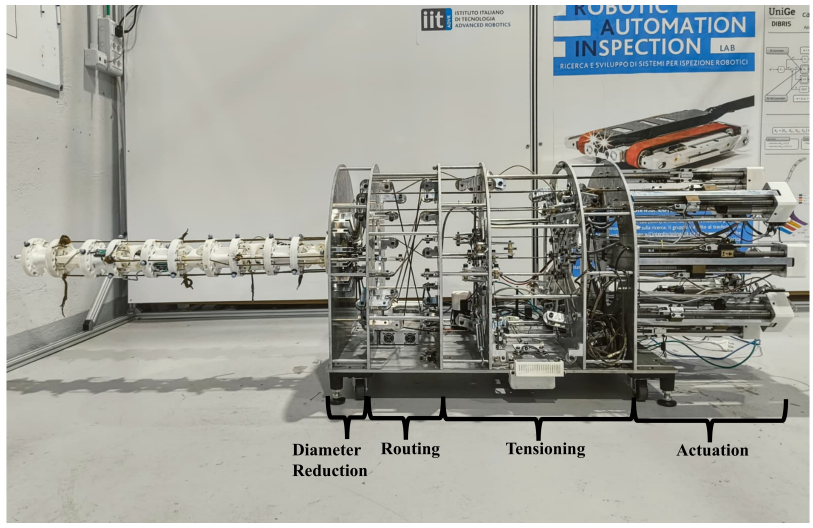


Figure 5.1 LORY-5JP and its actuation and tensioning system

5.1.1 Tensioning System Overview

This section provides a brief overview of the tensioning system and its operating principle, used for the new active tensioning method for the robot tendons. A detailed account of the design and construction can be found in [140]; however, these specifics are not relevant for this study. The actuation box, shown in Figure 5.1, comprises a chassis with cart wheels that house the actuators, active tensioning system, and electronics. The base can be divided into four stages: actuation, tensioning, routing, and diameter reduction. The actuation stage is dimensioned for the future scaled 8-joint configuration (LORY-8JP) presented later in this dissertation, and consists of eight linear actuators evenly distributed along a circular path, allowing the tendons to be arranged on a 500 *mm* diameter, which enables the base to drive up to eight joints. Once they leave the motors, the tendons pass through the active tensioning stage.

The active tensioning system comprises a motor, a tendon, and two tensioning plates with parallel support pulleys, spaced to allow attachment of sliders via additional pulleys. Tightening the routed tendon pulls sliders inward to tension slack tendons. The tensioning tendon is pulled by the tensioner motor through a hoist.

The working principle of the tensioning system is presented in Figure 5.2. During joint actuation, the motor tensions one tendon of the pair while the other is simultaneously slack. The pulled tendon is subject to the ΔF_i actuation force difference necessary to generate the required torque τ at the joint. Since $\Delta F_i \gg F_t$, with F_t the tensioner force setpoint, the slider of the pulled tendon remains essentially stationary (aside from tendon

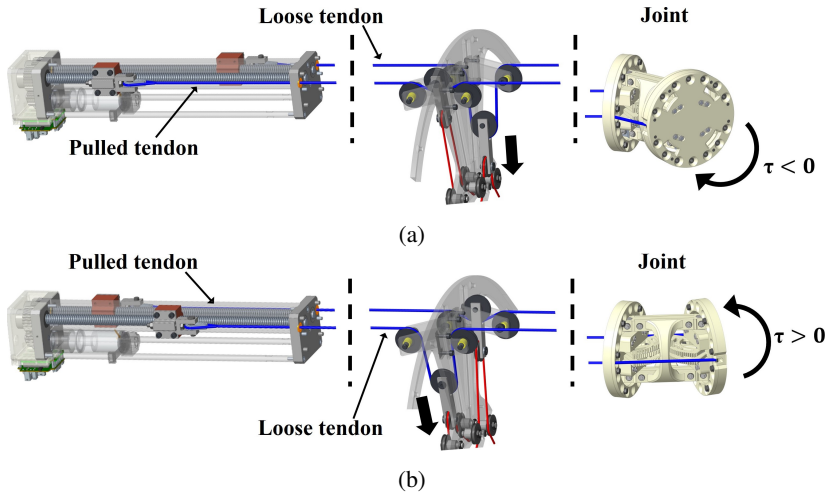


Figure 5.2 Working principle of the active-tensioning system. In (a) and (b) respectively, according to the applied moment, the slider on the loose tendon (blue) is pulled by the slider under the action of the tensioning-tendon (red), avoiding slack by imposing the minimum tension F_t.

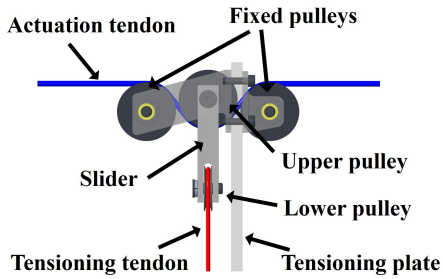


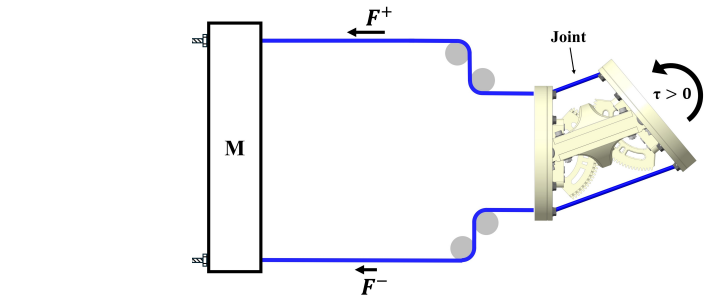
Figure 5.3 Side view of a tensioning slider. It has no support and is held in position solely by the forces exchanged by the tendons: actuation one on the upper pulley, and tensioning one on the lower pulley.

deformation), resulting in a state where the tension force is equilibrated by the actuation force. The slack tendon is tensioned by the corresponding slider, as shown in figure 5.3, which retracts the excess length and restores tensile force F_t.

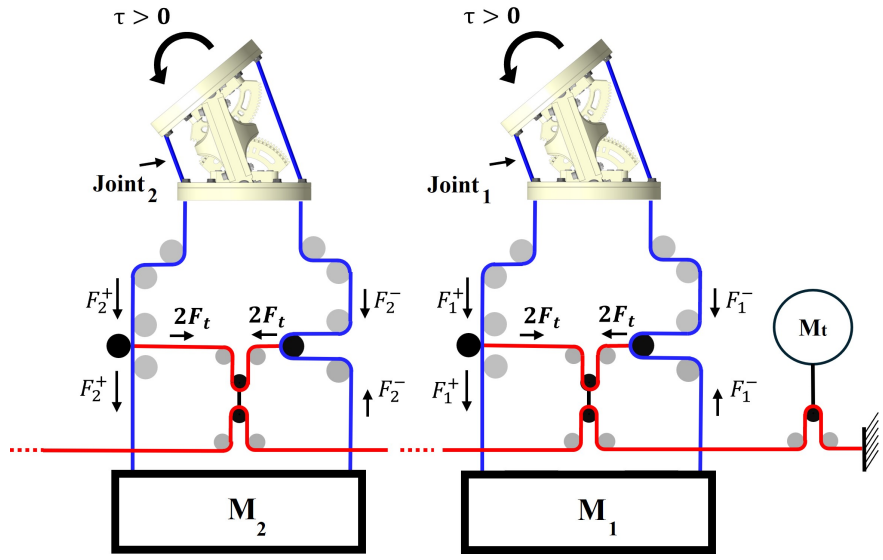
5.1.2 New Static Model Considering Active Tension

In the original concept (Appendix B and [118]), as shown in figure 5.4a, tendons in each antagonistic pair were considered to have a fixed pre-tensioning load F_t, while joint torque was generated by a force difference ΔF_i so that

$$F^+ = F_t + \Delta F_i/2\,, \quad F^- = F_t - \Delta F_i/2 \tag{5.1}$$



(a)



(b)

Figure 5.4 Working principle of the proposed active tensioning system with the case of necessary actuation torque $\tau > 0$. In (a), representing the original concept, considerable pre-tensioning is applied to the tendons to ensure no slack in any geometrical configuration. In (b), a single tensioner motor M_t pulls the loosened tendon of each joint i (i.e. F_i^-), guaranteeing a minimum tension force F_t.

where F^+ and F^- are the actuating tendon forces and $F^+ > F^- \Rightarrow \Delta F_i > 0$. This keeps the total pair force $F^+ + F^- = 2F_t$ constant at all times, so the structure has to withstand high compression loads even when external demand is low, and slack may still appear when $|\Delta F_i| > 2F_t$ unless F_t is unnecessarily high.

To address this issue, the active tensioning system dynamically maintains tendon tension. The tensioning system must apply a baseline tension F_t to each tendon at all times and allow tension to increase above this baseline when necessary. With the active tensioning system, the static equilibrium equations retain the same form as in the previous work for net torque, but the relationship between F^+, F^- and ΔF_i is fundamentally changed. The critical difference is that F_i^+ and F_i^-, where $i \in [1,...,n]$ (assuming n joints), are no longer expressed symmetrically around a fixed average. Instead, the tensioning system maintains a minimum tension F_t in each tendon and permits the other tendon's tension to rise to provide the required torque. The conditional equations are:

$$
\begin{aligned}
F_i^+ &= \begin{cases} F_t + \Delta F_i & \text{if } \Delta F_i > 0 \\ F_t & \text{if } \Delta F_i \leq 0 \end{cases} \\
F_i^- &= \begin{cases} F_t & \text{if } \Delta F_i > 0 \\ F_t - \Delta F_i & \text{if } \Delta F_i \leq 0 \end{cases}
\end{aligned}
\tag{5.2}
$$

If a positive force difference is required, the upper tendon carries the additional load ($F^+ = F_t + \Delta F_i$) while the lower tendon remains at the baseline ($F^- = F_t$). Similarly, if $\Delta F_i < 0$, the lower tendon carries the excess ($F^- = F_t - \Delta F_i$) and the upper tendon stays at F_t. These relations replace the single linear constraint of the original model. To derive the joint equilibrium equations under this new scheme, the torque relation:

$$
(F_i^+ - F_i^-) r_i = \tau_i \tag{5.3}
$$

where r_i is the joint lever arm radius and τ_i is the ith joint torque, is combined with the conditional definitions (5.2). There are two sub-cases for each joint i.

In **Case** 1: $\Delta F_i > 0$, the governing equation for joint i is:

$$
\begin{bmatrix} 1 & -1 \\ 0 & 1 \end{bmatrix} \begin{pmatrix} F_i^+ \\ F_i^- \end{pmatrix} = \begin{pmatrix} \tau_i / r_i \\ F_t \end{pmatrix} \tag{5.4}
$$

which replaces the original $(F_i^+, F_i^-) = 2F_{t_i}$ constraint with the new condition.

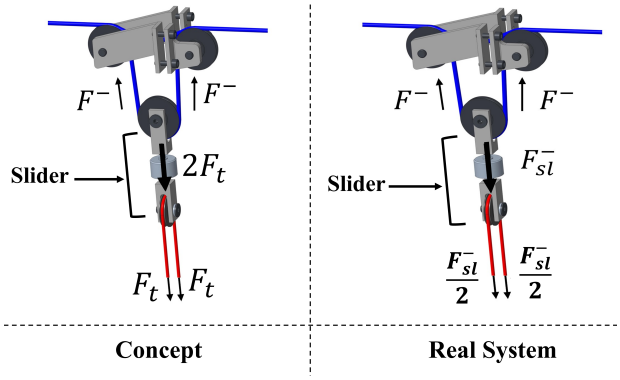


Figure 5.5 Measured forces. The output force F_{sl} is measured in both the sliders of a single joint (the figure shows the tendon that transmits the tension F^-).

In **Case** 2: $\Delta F_i < 0$, the joint equation becomes:

$$\begin{bmatrix} 1 & -1 \\ 1 & 0 \end{bmatrix} \begin{pmatrix} F_i^+ \\ F_i^- \end{pmatrix} = \begin{pmatrix} \tau_i / r_i \\ F_t \end{pmatrix} \tag{5.5}$$

In both cases, in the equilibrium equation $\tau_i = \Delta F_i r_i$, the assignment of ΔF_i to either the upper or lower tendon's excess tension is made according to the sign of τ_i. In practice, the sign of τ_i, which is determined by the direction of the external load on joint i and the coordinate frame orientation, determines directly which tendon must bear the extra tension. In static configurations under gravity, typically one side of each joint (e.g., all "upper" tendons) consistently carries the additional load. However, the conditional formulations 5.4 and 5.5 are general and can handle scenarios where the loading directions of different joints vary.

The new baseline tension at the tensioner can be set lower than the one in the original concept, since it is no longer necessary to accommodate the worst-case $\Delta F_i/2$ with F_t. Under low external loads, the robot's joints are under less internal tension, reducing unwanted compressive forces and potentially improving efficiency and lifespan. When a joint experiences a high load, the tensioning system increases the total tension in that joint's tendons (one tendon goes higher, the other remains at F_t) to react to the load. This means the internal force is applied "on demand" rather than being always on.

In theory, the tensioning force F_t applied by the active tensioning system should be transmitted equally to both the upper and lower tendons at each joint, as shown in figure 5.5 (left). However, due to friction in the pulley mechanism connecting the tensioner motor to the actuation tendons, the effective tension delivered to the upper vs.

the lower tendon differs, causing one side to experience higher tension than the other. As a result, the tension input F_t can no longer be treated as a single scalar value equal for all the tendons; instead, it must be represented as a pair of values for each joint. These values are denoted as $F^+_{sl_i}/2$ and $F^-_{sl_i}/2$, as presented in figure 5.5 (right), corresponding to the tensioning force in the upper tendon and lower tendon for the ith joint, respectively. Equivalently, F_t becomes an $n \times 2$ matrix, with n equal to the number of joints, where each row $\left[\frac{F^+_{sl_i}}{2}, \frac{F^-_{sl_i}}{2}\right]$ contains the tensioning forces for the two tendons at the ith joint. The statics model uses the appropriate value from this pair depending on which tendon is active in the equilibrium: if the net force difference $\Delta F > 0$ at a joint, indicating the upper tendon is carrying load, the model uses $F^+_{sl}/2$ for that joint ($F_t = \frac{F^+_{sl}}{2}$); if $\Delta F \leq 0$, indicating the lower tendon is active, then F^-_{sl} is used instead ($F_t = \frac{F^-_{sl}}{2}$). So equation 5.2 becomes:

$$F_i^+ = \begin{cases} \frac{F^+_{sl}}{2} + \Delta F_i & \text{if } \Delta F_i > 0 \\ \frac{F^+_{sl}}{2} & \text{if } \Delta F_i \leq 0 \end{cases}$$
$$F_i^- = \begin{cases} \frac{F^-_{sl}}{2} & \text{if } \Delta F_i > 0 \\ \frac{F^-_{sl}}{2} - \Delta F_i & \text{if } \Delta F_i \leq 0 \end{cases} \tag{5.6}$$

5.2 Tensioning System Performance in Static Condition

The first test is performed on a 5-joints prototype in static conditions, with all the joints in a fixed zero pose. The full experimental setup, measurement parameters and measurement accuracy are presented in [140]. Two values of forces have been measured, as shown in Figure 5.5: the input value of the tensioning force F_t imposed by the tensioner motor, used to control the system, and the output forces F^+_{sl} and F^-_{sl} measured in the two sliders of each joint i.

5.2.1 Tension Experiments and Data Acquisition

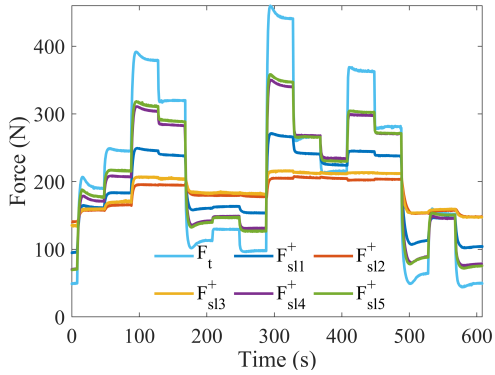
In the preliminary testing phase, the tendons manifested a strong dependency on the previous load condition. More specifically, once a tensioning force is applied and then removed, the slider shows a non-zero measurement. To address this issue, an initial tensioning warm-up cycle was applied to ensure the system started from a repeatable condition. During this warm-up phase, the tensioner force F_t was ramped smoothly from

a baseline of 50 N up to 510 N, and then back down to 50 N. The forces are measured with using load-cells model $KM26z-500N$ from ME Systeme [1], inserted into the sliders shown in figure 5.5. They have a rated force of $500\,N$ and a measuring error $\varepsilon_c = \pm 5\,N$, and were kept below 110% of the nominal capacity (i.e., $550\,N$) as recommended by the manufacturer to preserve calibration accuracy. The maximum tensioning force has been set to prevent mechanical failure in the load cell. This process removes some of the hysteresis in the tendons of the tensioner mechanism, bringing the system to a stable, consistent starting state for subsequent measurements. During the experiments, it was observed that after a series of warm-up cycles, the measured tensions at the two ends (F_{sl}^{+} and F_{sl}^{-}) consistently returned to nearly the same values as the previous cycle. This confirms that the warm-up effectively resets the system, preparing the tendons for a more reliable and efficient test by mitigating initial transient effects. After the warm-up procedure, two types of force input profiles were applied at the tensioner to characterise the system's behaviour. In each case, the tensioner force F_t was driven through a sequence of setpoint values, and the corresponding responses at F_{sl}^{+} and F_{sl}^{-} are measured by the load cells. The data were recorded at a constant sampling rate of 20 ms (50 Hz), giving roughly $4 \cdot 10^4$ data points for each complete test run, which has a duration of 800 seconds. Each target force level was held for a duration $\tau_{hold} = 40\ s$ to allow the system to settle to a quasi steady-state before moving to the next tension level. This hold time was chosen based on the observed settling time of the output tensions while performing preliminary tests, ensuring that F_{sl}^{+} and F_{sl}^{-} had sufficient time to stabilise near constant values before the next step change in F_t. The two input profiles are chosen for the tests: stepped and randomised. The first is a monotonic stepwise ramp starting from 50 N, which is the baseline tension. The tensioner force was increased in increments of 50 N, up to a maximum of 450 N. Each level was maintained for the time τ to reach a near steady state. After reaching 450 N, the process was reversed with stepwise decreases, symmetric to the increasing path, down to $50\,N$ again, with the same hold duration at each step. The second profile followed a random sequence of tension levels to generate a rich dataset for system identification. Beginning at the 50 N baseline, the tensioner force was commanded to jump to various arbitrary values within the range $[50, 450]\,N$. Each new level was again held for τ. This randomised step path excites a wide spectrum of the system's dynamics, identifying both linear and non-linear response characteristics across different loading conditions.

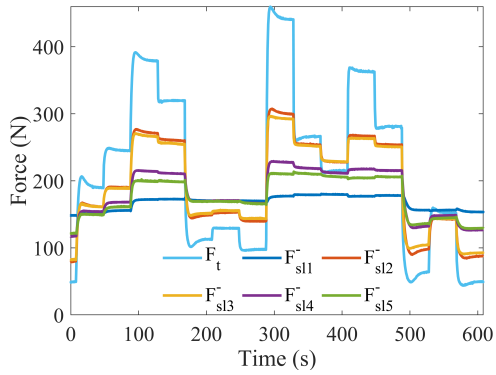
[1] https://www.me-systeme.de/en/km-load-cell

5.2.2 TENSIONING SYSTEM PERFORMANCE

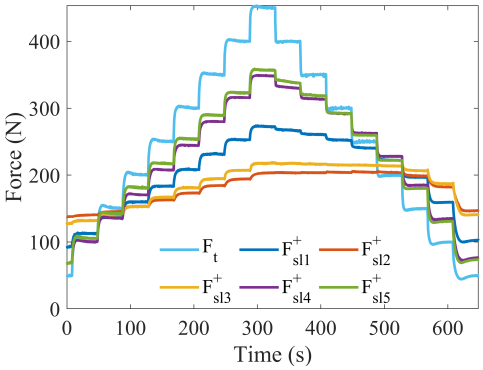
Figure 5.6 shows the tension levels reached by each slider for incremental and decremental stepwise force F_t. It is clear that the tension does not distribute uniformly along the tendon



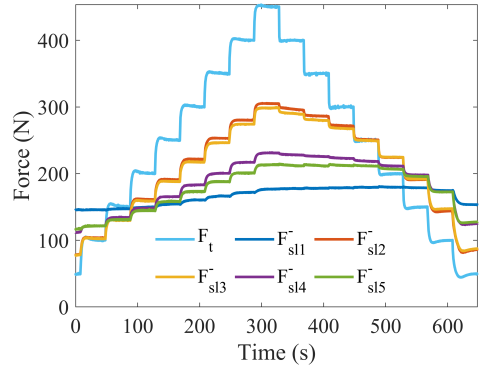
(a) F_t and F_{sl}^{+} for all joints - random path



(b) F_t and F_{sl}^{-} for all joints - random path



(c) F_t and F_{sl}^{+} for all joints - stepped path



(d) F_t and F_{sl}^{-} for all joints - stepped path

Figure 5.6 Comparison of slider tensions F_{sl}^{+} and F_{sl}^{-} against tensioner force F_t under (a,b) random and (c,d) stepped F_t paths.

path: some sliders reach higher tension values, while others appear less sensitive to the tensioner. Examining the plots, it is evident that some sliders, during the unloading phase, do not release the acquired tension until the tensioner drops below their actual tension value, and when unloading is completed, all the sliders maintain a tension value higher than that of the tensioner. To quantify the efficiency of the tendon tensioning system in static conditions, the transmission efficiency η_{static} is defined as the ratio between the tension received by the least loaded tendon and the commanded reference tension:

$$\eta_{static} = \frac{F_{\mathrm{sl}}^{min}}{F_t} \tag{5.7}$$

where F_{sl}^{min} is the minimum force measured among the sliders at the moment the system reaches steady state, and F_t is the global reference tension set by the tensioning actuator.

To ensure robustness against measurement noise, a conservative 5 N margin is applied: F_{sl}^{min} is reduced by 5 N, and F_t is increased by 5 N before computing η_{static}. During experiments using a randomised load path, the lowest measured efficiency is:

$$\eta_{static}^{min} = \frac{162\ \mathrm{N}}{(456+5)\ \mathrm{N}} \approx 36.7\%$$

while the average efficiency on the least tensioned tendons across all tendons is:

$$\eta_{static,avg}^{min} = \frac{F_{sl}^{min,avg}}{F_t} \approx 37.1\%$$

where $F_{sl}^{min,avg}$ is the average across all joints of the minimum achieved tension on the slack tendon slider. This means that, at the worst point, only 36.7% of the commanded tendon tension was transmitted to the most unloaded slider tendon, while an average of 37.1% is achieved considering all unloaded sliders. These values represent a lower bound for system performance under non-ideal routing and distributed friction.

Despite being conservative, this estimate highlights the limits of force transmission across passive routing paths and motivates the design improvements discussed in the following sections.

These results demonstrate that the system can guarantee a minimum tension with an effectiveness defined with the mean value of 37.1%, but it suffers from permanent tension in the tendons due to friction effects from the pulleys and within the tendons themselves. In the next section, this issue will be addressed through the system's hysteresis.

5.2.3 Tensioning System Hysteresis and Mechanical Efficiency

The tensioning system presents intrinsic effects, including damping and friction elements that dissipate a portion of the input energy. By analysing hysteresis, it is possible to quantify the system's overall efficiency. This value is obtained by comparing the work performed over a loading-unloading cycle, specifically as the ratio between the energy released by the tensioner during unloading and the energy supplied during loading. This approach treats the tensioner as an elastic element with internal friction (hysteresis), where any difference in the returned energy represents a loss. This phenomenon produces a characteristic hysteresis loop in the force-displacement plane. Quantitatively, the hysteresis loop can be observed by plotting the tension F_t against actuator linear displacement

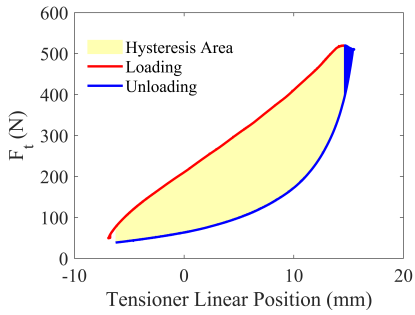


Figure 5.7 Loading and unloading F_t trends representing the hysteresis loss at the tensioner

x of the tensioner linear actuator for a complete loading-unloading cycle. Regarding this system, the measured actuator displacement, x, and tendon tension F_t, are considered for the loading (increasing force) and unloading (decreasing force) branches. The loading and unloading portions of the cycle are identified by locating the maximum displacement point (turnaround point) within a selected interval corresponding to a complete loading-unloading cycle. The area enclosed by this loop corresponds to the energy dissipated per cycle due to irreversible losses. Mathematically, if $F_{\uparrow}(x)$ and $F_{\downarrow}(x)$ represent the force during loading and unloading, respectively, at each displacement x, then the energy lost to hysteresis over a full cycle is:

$$E_{\text{hyst}} = \oint F_t(x)\,dx = W_{in} - W_{out} \tag{5.8}$$

Where:

$$W_{\text{in}} = \int_{x_{\min}}^{x_{\max}} F_{\uparrow}(x)\,dx\,; \qquad W_{\text{out}} = -\int_{x_{\min}}^{x_{\max}} F_{\downarrow}(x)\,dx \tag{5.9}$$

are the input work during loading and the useful returned work during unloading, respectively, performed on the system. Here, $x_{\min}$ and $x_{\max}$ are the actuator's limits for that cycle.

So the energy lost to hysteresis is then simply the difference:

$$E_{\text{hyst}} = \int_{x_{\min}}^{x_{\max}} \left[F_{\uparrow}(x) - F_{\downarrow}(x)\right] dx \tag{5.10}$$

Figure 5.7 shows the area representing the losses due to hysteresis on the tensioner tendon as a function of the linear position of the tensioning actuator. The two branches are interpolated onto a common displacement vector to ensure one-to-one correspondence for area calculations. The work input W_{in}, work output W_{out}, and hysteresis loss E_{hyst} are then calculated using the trapezoidal integration over the respective branches. The average

energy loss at the tensioner, after having performed 5 identical loading-unloading tests, is $L = W_{in} - W_{out} = 3.6\,J$. The mechanical efficiency of the tensioning system is defined as: $\eta = W_{out}/W_{in}$. In this case, the average efficiency is $\eta = 41.4\%$. This metric represents the intrinsic mechanical energy dissipation of the tendon-tensioner transmission under operational loading conditions.

5.3 Tensioner Effectiveness During Robot Motion

The previous section analysed the tensioner system performance under static conditions, where the robot joints were held stationary, and the motors were inactive. In practice, however, the robot executes trajectories while the tensioner maintains tendon pretension. This section extends the analysis to dynamic conditions, investigating the tensioner's effectiveness during robot motion.

5.3.1 Trajectory Generation and Experimental Protocol

For better robot control, a rigorous mathematical framework is established to map desired joint-space motions to actuator velocities, explicitly accounting for the mechanical coupling inherent in tendon routing. To generate the experimental trajectories used for data collection, it was necessary to implement a kinematic model that reflects the physical routing of the tendons. In this system, the tendons are not routed independently for each joint; rather, there is mechanical coupling, meaning the motion of proximal joints affects the tendon lengths required for distal joints.

In LORY-5JP, each actuator pulls a tendon routed through a series of joints. Due to the serial routing, each tendon influences its own target joint and all upstream joints it passes through. This coupling is captured by the routing matrix $\mathbf{T}_{routing} \in \mathbb{R}^{5\times5}$ [58]. Each entry T_{ij} specifies the port index at which the j-th tendon crosses the i-th joint:

$$\mathbf{T}_{routing} = \begin{bmatrix} 4 & 8 & 3 & 7 & 5 \\ 0 & 4 & 0 & 3 & 1 \\ 0 & 0 & 4 & 8 & 5 \\ 0 & 0 & 0 & 4 & 0 \\ 0 & 0 & 0 & 0 & 4 \end{bmatrix} \tag{5.11}$$

Because tendons only affect joints at or before their target, the matrix is upper triangular.

Each routing index corresponds to a physical tendon port location. A value of zero means there is no interaction To obtain the mechanical effect of tendon routing, we

compute the effective lever arm length at each crossing. These are stored in the distance matrix $\mathbf{D} \in \mathbb{R}^{5\times5}$, whose entries are derived from the tendon port geometry. Assuming the tendon ports are placed evenly around a circle of diameter $d_c = 0.115$ m and indexed at angular increments of $\theta_\pi = \pi/8$, the effective moment arm for tendon j acting on joint i is:

$$d_{ij} = \begin{cases} d_c \cdot \sin(T_{ij} \cdot \theta_\pi) & \text{if } T_{ij} \neq 0 \\ 0 & \text{otherwise} \end{cases} \tag{5.12}$$

This converts routing indices into geometric distances, generating an upper triangular matrix $\mathbf{D}$.

To convert joint velocities into actuator velocities, we need to project these lever arms onto the direction of joint rotation. For a revolute joint, the effective contribution of a tendon depends on the cosine of the joint angle. This results in the actuation Jacobian $\mathbf{J}(\boldsymbol{\theta}) \in \mathbb{R}^{5\times5}$, which maps joint velocities $\dot{\boldsymbol{q}}$ to tendon linear velocities $\dot{\mathbf{L}}$:

$$J_{ji}(\boldsymbol{\theta}) = \begin{cases} d_{ij} \cdot \cos(q_i) & \text{if } i \leq j \\ 0 & \text{otherwise} \end{cases} \tag{5.13}$$

Here, the index j refers to the actuator (tendon), and i refers to the joint. Each actuator must compensate for the motion of all joints it passes through (from 1 to j), leading to a lower-triangular Jacobian.

Finally, the differential kinematics linking joint and actuator space is given by:

$$\dot{\mathbf{L}} = \mathbf{J}_{ji}(\boldsymbol{q}) \cdot \dot{\boldsymbol{q}} \tag{5.14}$$

Here, $\mathbf{J}_{ji}$ represents the influence of the i-th joint velocity on the j-th actuator velocity. The lower-triangular nature of $\mathbf{J}$ reflects the cumulative effect of the serial chain: the j-th actuator must compensate for the motion of all joints i from 1 up to j. This expression is used in trajectory generation and feedforward control to compute the tendon velocities needed to follow a joint trajectory while accounting for routing interactions. To control the motors, this linear velocity must be converted into rotational velocity ($\boldsymbol{\omega}$) in RPM. This conversion accounts for the lead screw pitch ($p = 0.003$ m) and the transmission ratio ($N_{tr} = 1.5 \times 26 = 39$). The final command equation is:

$$\boldsymbol{\omega}_{RPM} = \dot{\mathbf{L}} \cdot \left(\frac{60 \cdot N_{tr}}{p} \right) \tag{5.15}$$

This formulation enables precise actuator command generation that maintains kinematic consistency during motion, preventing physically induced slack or excessive tension caused by geometric errors.

To collect a comprehensive dataset for tension analysis, a point-to-point trajectory generator was implemented. The trajectory was defined by a series of setpoints in the 5-dimensional joint space, spanning a representative volume of the robot's workspace. The motion between setpoints was generated using linear interpolation over a fixed movement time ($t_{move} = 30$ s) followed by a hold time ($t_{hold} = 40$ s). For each time step k with duration $\Delta t = 0.02\ s$, the joint position $\boldsymbol{q}_k$ is computed by linearly interpolating between the start vector $\boldsymbol{q}_{start}$ and target vector $\boldsymbol{q}_{target}$. Then the joint velocity is approximated using finite differences:

$$\dot{\boldsymbol{q}}_k = \frac{\boldsymbol{q}_k - \boldsymbol{q}_{k-1}}{\Delta t} \tag{5.16}$$

The computed $\boldsymbol{q}_k$ and $\dot{\boldsymbol{q}}_k$ are fed into the Jacobian formulation to generate the actuator velocity profile.

The robot trajectory is determined by selecting several random final poses for the robot to reach, while avoiding configurations that could cause high stress on the robot's weakest component.

To maintain structural safety during these experiments, the model developed in Chapter 4 is employed as a predictive safety constraint. Rather than simply identifying the single worst-case scenario, the trained GP model provides a rapid stress estimation for any candidate configuration. The procedure for generating the trajectory is carried out according to the following protocol:

1. A random target joint configuration $\mathbf{q}_{target}$ is sampled from the manipulator's workspace.

2. The corresponding static load vector $\mathbf{x}$ at the base is computed using the static model (Appendix B).

3. This load vector is queried against the GP surrogate model to predict the peak Von Mises stress.

4. The configuration is accepted only if the predicted stress remains below a conservative safety threshold (e.g., $\sigma_{safe} < 0.6 \cdot \sigma_{yield}$).

This active filtering verifies that the random exploration of the workspace is confined to the structurally safe subset of the configuration space, effectively bypassing regions of

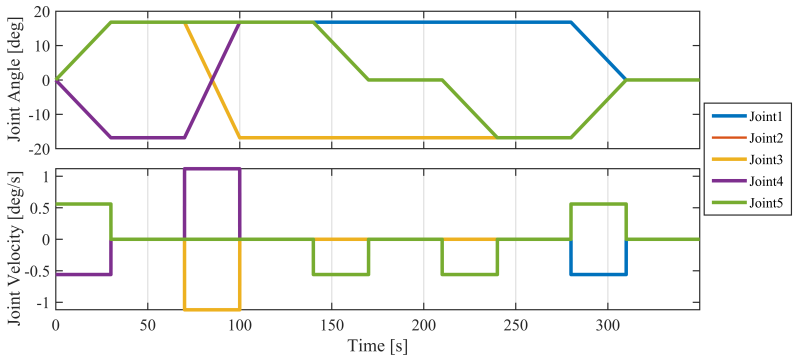


Figure 5.8 Joint angles and their velocities as a function of time.

high mechanical risk. The trajectory that the robot follows for this experiment is shown in figure 5.8.

A total of 7 (one per tension level) motion tests were conducted with the robot executing a trajectory while the tensioner maintained constant force levels $F_t \in \{0, \ldots, 300\}$ N with 50 N increments. The $F_t = 0$ N condition serves as the baseline, representing the tendon tension achievable through motor control alone (without tensioner assistance). For each configuration, joint angles, motor velocities, and tensions (F_{sl}^{+}, F_{sl}^{-}) were recorded at 50 Hz, generating 17500 samples per test, and a total duration of 350 s. The trajectory covered the operational workspace of all five joints. The full set of experimental results for tendon force trends across all joints and tensioner force levels is presented in the plots in Appendix D. At each tensioner level, the mean of instantaneous minimum tendon tensions and the 5th percentile (95% confidence guarantee) were computed.

To evaluate tensioner performance across a representative range of operating conditions, a trajectory that activates all five joints through various motion directions and magnitudes was generated. The trajectory consists of six setpoints, with the robot moving between consecutive positions, as reported in table 5.1. Each segment of the trajectory

Setpoint	θ_1 [rad]	θ_2 [rad]	θ_3 [rad]	θ_4 [rad]	θ_5 [rad]
1	0.209	0.209	0.209	−0.209	0.209
2	0.168	0.168	0.168	−0.168	0.168
3	0.293	0.293	0.293	−0.293	0.293
4	0.293	0.000	−0.293	0.000	0.000
5	0.293	−0.293	0.293	−0.293	−0.293
6	0.000	0.000	0.000	0.000	0.000

Table 5.1 Target joint positions for the motion test trajectory

comprises a motion phase of 30 s of coordinated joint movement and a hold phase of 40 s of static position maintenance at the target setpoint.

5.3.2 Tension Analysis

In an antagonistic tendon-driven joint, two tendons work in opposition. At any instant, the tension in each tendon depends on multiple factors, including motor torque, joint position, external loads, and tensioner force.

A first baseline test in which the tensioner is not active ($F_t = 0$ N) was conducted. A critical finding from this first test is that all joints experience zero minimum tendon tension during the trajectory. This means that without tensioner assistance, the tendons go completely slack at some point during the motion, even though the motors are actively controlled. This observation confirms that the tensioner is essential for preventing tendon slack during dynamic operation, as motor control alone is insufficient.

When a joint moves in a particular direction, one tendon must provide the driving force while the other follows passively.

This means that during motion, the relevant tendon for evaluating tension maintenance is the passive tendon that is not being actively pulled by the motor, as it only has tension provided by the tensioner. So for each joint, the relevant tension is:

$$T_{\text{rel}}(t) = \begin{cases} F_{sl}^{+}(t) & \text{if } \dot{\theta}(t) < 0 \\ F_{sl}^{-}(t) & \text{if } \dot{\theta}(t) > 0 \\ \min(F_{sl}^{+}(t), F_{sl}^{-}(t)) & \text{if } \dot{\theta}(t) = 0 \end{cases} \tag{5.17}$$

The motion phases are defined as those parts of the trajectory in which at least one joint is rotating. Table 5.2 presents the minimum relevant tendon tension (T_{rel}) observed during the motion phases for each joint and tensioner force level. The tension T_{rel} represents the tension on the relevant tendon, defined as the minimum between F_{sl}^{+} and F_{sl}^{-} for each joint. The relevant tendon is selected according to Equation 5.17, based on the direction of motion. The motion phase efficiency is defined as:

$$\eta_{\text{motion}} = \frac{T_{rel,min}(F_t)}{F_t} \times 100\% \tag{5.18}$$

Table 5.2 presents the motion phase efficiency for each joint. The motion efficiency has an average of 61.6% and a worst-case average of 51.9%. These values are significantly

F_t [N]	$T_{rel,min}$ [N]	$\eta_{motion}[\%]$
50	T_{rel4} =22.4	44.8
100	T_{rel3} =48.3	48.3
150	T_{rel3} =82.9	55.3
200	T_{rel3} =120.9	60.5
250	T_{rel4} =129.8	51.9
300	T_{rel1} =152.0	50.7

Table 5.2 Minimum relevant tendon tension during motion phases. The middle column reports the joint with the minimum tension and its corresponding value.

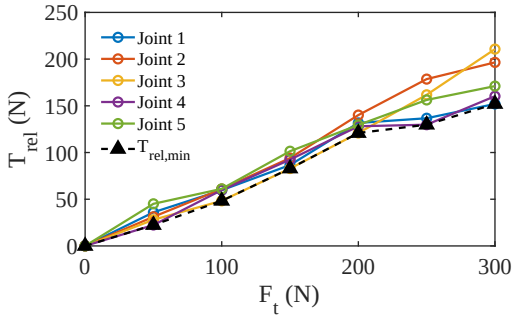


Figure 5.9 Relevant tendon tension T_{rel} during motion phase as a function of tensioner force for each joint. The black triangles represent the $T_{rel,min}$ across all joints (e.g. the $T_{rel,min}$ at 50 N corresponds to $T_{rel4} = 22.4$ N as shown in table 5.2.

higher than the static efficiency of 37.1%. Figure 5.9 illustrates the relationship between F_t and T_{rel} for each joint.

The hold phases are the parts of the trajectory in which all the joints are set to rest. The 40 second hold phases at each setpoint represent quasi-static conditions in which the robot maintains a fixed position with the motors actively engaged. During these periods, joint velocities are nominally zero ($\dot{\theta} \approx 0$), both tendons contribute to position holding and stiffness, and the motors provide holding torque in addition to tensioner force

The hold-phase efficiency provides a validation point against static efficiency and reveals how quickly the system settles after motion.

During hold phases, both tendons should maintain tension, so $\min(F_{sl}^{+}, F_{sl}^{-})$ are evaluated. Table 5.3 presents the hold phase efficiency for each joint.

Figure 5.10 shows the relationship between hold minimum tension and tensioner force during the hold phases.

The hold-phase efficiency is high, with an average of 74.0% and a worst-case average of 63.9% across all tension levels.

F_t [N]	$T_{rel,min}$ [N]	$\eta_{hold}[\%]$
50	T_{rel2} =40.7	81.4
100	T_{rel3} =60.7	60.7
150	T_{rel1} =92.0	61.3
200	T_{rel5} =145.3	72.7
250	T_{rel5} =135.3	54.1
300	T_{rel1} =159.6	53.2

Table 5.3 Minimum relevant tendon tension during hold phases. The middle column reports the joint with the minimum tension and its corresponding value.

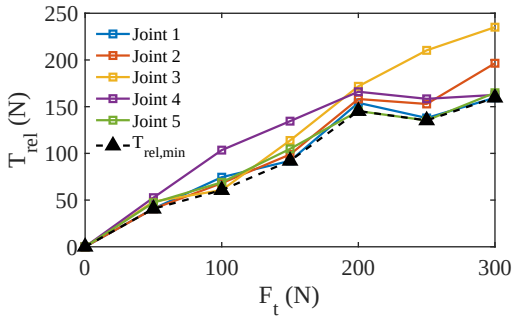


Figure 5.10 Relevant tendon tension T_{rel} during hold phase as a function of tensioner force for each joint. The black triangles represent the $T_{rel,min}$ across all joints (e.g. the $T_{rel,min}$ at 50 N corresponds to $T_{rel2} = 40.7$ N as shown in table 5.3.

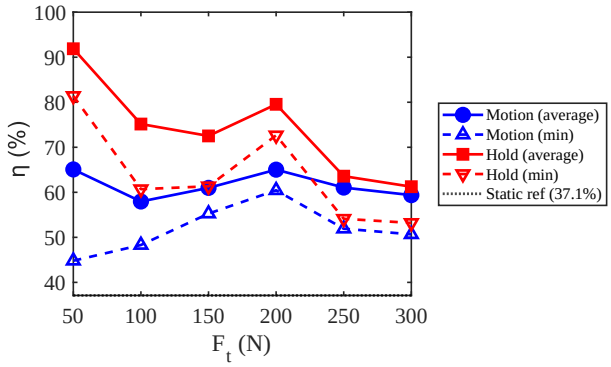


Figure 5.11 Efficiency comparison between motion and hold phases. Both average (solid) and worst-case (dashed) values are shown. The static reference (37.1%) is indicated by the dotted line. Both operating modes exceed the static reference.

Figure 5.11 illustrates the efficiency comparison across all tensioner force levels. The plot reveals a striking result: both motion and hold efficiency during active robot operation exceed the static efficiency measured with motors disabled.

The data confirm that the worst-case (minimum) tension values occur during the steady-state portion of each segment, not specifically at the transitions. This is because during acceleration, while the motor actively engages the loaded tendon, the joint also pulls the passive tendon. Instead, during the hold phases, the only tension experienced by the tendons is the one provided by the tensioner. At cruising speed, the friction load is steady, and tension is maintained, whereas during deceleration, torque reduces gradually. When a joint reverses direction between segments, the reversal occurs during the 40-second hold phase, and both tendons experience tension as the motor prepares to move in the new direction. The new direction's tendon becomes loaded only when motion actually begins.

This means reversals occur in a controlled manner during hold phases, and the motion analysis correctly reflects the post-reversal behaviour by selecting the appropriate tendon for the new direction.

5.3.3 Trajectory Tracking Performance vs Tensioner Force

While the tensioner prevents tendon slack, it introduces a fundamental control challenge: the tensioner force acts as a position-dependent disturbance that the motor controller must counteract. Consequently, there needs to be a trade-off between slack prevention (requiring a higher F_t) and trajectory tracking accuracy (favouring lower F_t). The tensioner

pulleys introduce friction and inertia into the tendon system. Higher tensioner forces increase friction losses and joint coupling, making the system dynamics more complex and position-dependent. As F_t increases, the disturbance grows, making trajectory following progressively more difficult.

For each joint $j \in \{1,\ldots,5\}$, the instantaneous tracking error at time t_i is the difference between the reference trajectory and measured encoder position:

$$e_j(t_i) = q_j^{\text{ref}}(t_i) - q_j^{\text{act}}(t_i) \tag{5.19}$$

where q_j^{ref} is the reference angle of joint j and q_j^{act} is the actual measured angle at joint j. Positive values indicate undershoot; negative values indicate overshoot. Performance is characterised using the RMS error, which is the typical tracking deviation over N samples, converted to degrees for interpretability:

$$e_{j,\text{RMS}} = \sqrt{\frac{1}{N}\sum_{i=1}^{N} e_j^2(t_i)} \tag{5.20}$$

RMS is used because it summarises the tracking error over the entire trajectory in a single value, accounting for both constant offsets and fluctuations. Experimental data were recorded at 50 Hz for $F_t \in \{0,50,\ldots,300\}$ N. Observed errors originate from physical phenomena, including cable elasticity, friction, motor dynamics, and kinematic coupling.

The data reveals a clear correlation between tensioner force and tracking error. At $F_t = 300$ N, the mean $e_{j,\text{RMS}}$ accross joints (1.15°) is 86% higher than at $F_t = 0$ N (0.62°).

The results show that lower F_t (0-50 N) have good trajectory tracking ($< 0.7°$ RMS), but low slack prevention. Moderate F_t (50-150 N) provides a good balance between tracking accuracy (0.7°-0.85° RMS) and slack prevention. This range provides sufficient minimum tendon tension (> 40 N) to avoid slack, while maintaining controller effectiveness. Figure 5.12 presents these results. High F_t (200-300 N) provides maximum slack prevention (minimum tension > 100 N), but tracking error exceeds 1°. Large disturbances degrade the controller's capacity, resulting in poor trajectory following.

The analysis identifies $F_t = 0$ N as optimal if slack were not a concern, highlighting that any non-zero tensioner force is a compromise to prevent tendon failure. However, at $F_t = 0$ N there is tendon slack, so based on the quantitative analysis and operational requirements, it is recommended $F_t = 50 - 100$ N during motion. During hold times, the only limit on the tensioner force increase is the robot's structural limit. At $F_t = 50$ N, the tracking error is 0.69° RMS ($< 0.7°$), representing only a 12% degradation compared

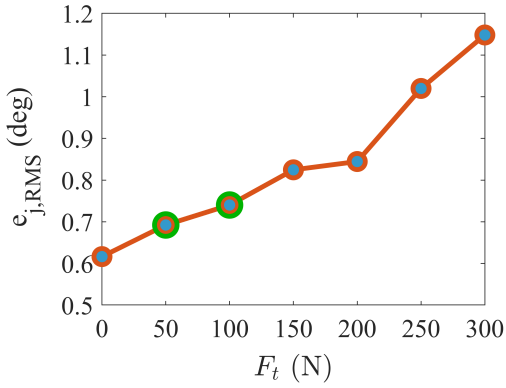


Figure 5.12 Mean Trajectory Tracking Error vs. F_t. Green circles indicate the recommended tension range for good slack removal while maintaining tracking error relatively low.

to the ideal case ($F_t = 0$ N). This is acceptable for most manipulation tasks and remains well below typical joint position accuracy requirements ($< 1^\circ$).

For applications requiring higher position stiffness or involving large external forces, F_t can be increased to 150-200 N, accepting the moderate tracking degradation (0.83°-0.85° RMS).

The results above show that increasing the global pretension reduces slack but also introduces drawbacks in tracking disturbances and tension-transfer hysteresis. The next concern is not only whether higher pretension prevents slack, but also how much stiffness it adds at the end-effector and how this effect is distributed along the arm. Section 5.4 answers this by quantifying stiffness modulation as a function of payload and pretension, establishing the trade-off between stiffness gains and tensioning.

5.4 Stiffness Modulation on LORY-5JP

Modern robotic systems often require adjustable stiffness to cover tasks ranging from safe interaction in uncertain environments to precise manipulation under load. For this reason, a large body of research has focused on Variable Stiffness Actuators (VSAs) [141], including approaches based on lever arms [142], elastic elements [143], or antagonistic drives [144]. In TD HR manipulators, stiffness regulation is often achieved through joint-level elastic mechanisms or by increasing the fixed pretension, which can increase actuation complexity and amplify transmission losses.

In LORY-5JP, the active tensioning architecture introduced in this chapter enables stiffness modulation without adding joint-level mechanisms. By increasing the baseline

tendon tension through a single global tensioning actuator [140], the same input used for slack mitigation also modifies the effective stiffness of the tendon-driven structure. This section quantifies how end-effector stiffness varies with payload and pretension, and relates these gains to the earlier practical limitation of tension-transfer losses [145].

5.4.1 Theoretical Framework

To systematically evaluate the efficacy of this global tensioning approach, a precise definition of stiffness metrics and a reliable method for extracting joint kinematics from marker data are required.

The tip translational stiffness K_{tip} is defined as the secant stiffness under a given payload W applied at the end-effector,

$$K_{\text{tip}}(W, F_t) = \frac{F_g(W)}{\Delta z_{\text{tip}}}; \qquad F_g(W) = Wg \tag{5.21}$$

where Δz_{tip} is the vertical deflection of the end-effector relative to its unloaded pose.

While K_{tip} provides a macroscopic performance metric, characterising the internal stiffening behaviour requires isolating the contribution of individual joints; this requires a precise method to reconstruct joint angles from surface markers.

To accurately measure joint stiffness, precise measurement of joint rotation is required. In principle, joint rotations can be obtained by computing the relative orientation between rigid-body frames attached to each link via quaternion-based pose reconstruction. In practice, two issues emerge in the present experiments: (i) markers are mounted at arbitrary locations on the link surfaces, so the reconstructed link frames are not exactly aligned with the mechanical joint axes; and (ii) distal joints undergo small rotations, so the extraction of a single Euler angle from the full 3D rotation matrix becomes extremely sensitive to small pose errors. When stiffness is computed as $\tau_i/\Delta\theta_i$, this amplifies measurement noise, especially at joints 3 and 5. To reduce this sensitivity, the fact that all tests are conducted in a nominally planar configuration is utilised. For each link, the markers are first translated in the x direction so that their mean longitudinal position matches the ideal link centre. The rotation of link i is then obtained from the slope of a best-fit straight line through the centred marker cloud in the (x,z) plane. Joint angles are derived as differences between adjacent link slopes. Because the same planar fit is applied to both the unloaded and loaded recordings, static misplacement of markers along the link cancels out when forming $\Delta\theta_i$. This purely geometric, planar method produces smooth and monotonic joint stiffness curves with tight dispersion.

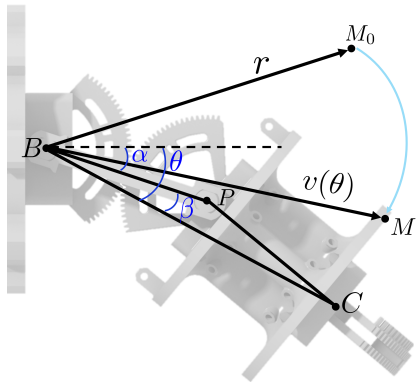


Figure 5.13 Joint geometry and joint angle representation

The joint-level stiffness analysis requires an estimate of the rotation of each bending joint between the unloaded initial configuration and the loaded configuration. In an ideal setting, one would place a marker exactly at each joint centre and measure the rotation of the link axis directly. In practice, this is not possible: reflective markers are mounted on the outer surface of the links, at arbitrary positions that are convenient for visibility and cluster attachment. Consequently, the measured deflections correspond to the motion of these off-centre marker points rather than to the motion of the link centres, and they need to be converted into actual joint angles.

This subsection shows that, under the assumption of rigid links, the change of the effective link angle can be recovered exactly from the motion of a single off-centre marker, without knowing its precise offset from the joint centre. Then the specific geared geometry of the joints is exploited to convert this effective link angle into the true joint angle used for stiffness identification.

The attention is restricted to the sagittal plane where gravity acts, which is the world X-Z plane, with Z vertical and X horizontal. The Y coordinate is ignored in the following derivation. Consider one generic bending joint with centre B and its adjacent link of length L. With reference to Figure 5.13, θ is the angle between the reference horizontal and $\overline{BC}$. The link centre at a distance $L = |\overline{BC}|$ from the joint along the link axis has coordinates

$$C(\theta) = \begin{bmatrix} X_C(\theta) \\ Z_C(\theta) \end{bmatrix} = \begin{bmatrix} Lc_\theta \\ Ls_\theta \end{bmatrix} \tag{5.22}$$

in the joint frame, where c_θ, s_θ represent $cos(\theta)$ and $sin(\theta)$, respectively. In the experiments, θ is not measured directly. Instead, a reflective marker is mounted at a point on the link surface that is arbitrary. Let M_0 denote the marker position when $\theta = 0$ and M

the marker position when $\theta \neq 0$. The marker position when $\theta = 0$ can be expressed by

$$r = \begin{bmatrix} x_0 \\ h \end{bmatrix} \tag{5.23}$$

where x_0 is the horizontal offset from the joint centre and h is the vertical offset (positive upwards). The exact values of x_0 and h depend on how the marker cluster is mounted and are not known a priori, but they are constant over the whole experiment because the marker is rigidly attached to the link.

When the link rotates by an angle θ, the vector from the joint centre to the marker is simply the rotated version of r:

$$v(\theta) = R(\theta)\, r = \begin{bmatrix} c_\theta & -s_\theta \\ s_\theta & c_\theta \end{bmatrix} \begin{bmatrix} x_0 \\ h \end{bmatrix} = \begin{bmatrix} x_0 c_\theta - h s_\theta \\ x_0 s_\theta + h c_\theta \end{bmatrix} \tag{5.24}$$

where $R(\theta)$ is the planar rotation matrix. Equation (5.24) describes what the Motion Capture (MoCap) system actually measures (up to the measurement noise): the marker coordinate in the joint frame is the vector $v(\theta)$.

Considering now the orientation of $v(\theta)$, the direction angle is defined as:

$$\phi(\theta) = \operatorname{atan2}\big(v_z(\theta),\, v_x(\theta)\big) = \operatorname{atan2}\big(x_0 s_\theta + h c_\theta,\; x_0 c_\theta - h s_\theta\big) \tag{5.25}$$

with v_x and v_z the X and Z components of $v(\theta)$. Similarly, the direction of the offset vector r when $\theta = 0$ is

$$\phi_r = \operatorname{atan2}(h, x_0) \tag{5.26}$$

Because $v(\theta) = R(\theta) r$, the vector $v(\theta)$ is exactly the vector r rotated by θ. Therefore, its direction is simply the sum of the apparent link angle and a constant offset:

$$\phi(\theta) = \theta + \phi_r \tag{5.27}$$

This relationship is independent of the particular values of x_0 and h; they only affect the constant bias ϕ_r. In other words, the marker always lies on a ray whose direction differs from the true link centreline by a fixed angular offset. Equation (5.27) can be inverted as: $\theta = \phi(\theta) - \phi_r$. So if ϕ_r were known, the absolute apparent angle θ from the marker direction can be computed. However, for stiffness identification, the absolute angle is not necessary; only the change in angle between the initial and loaded configurations is required.

Let θ_{init} denote the apparent link angle in the unloaded initial pose for a given (W, F_t) condition, and θ_{load} the corresponding angle in the loaded trial pose. The change of apparent angle is defined as: $\Delta\theta = \theta_{\text{load}} - \theta_{\text{init}}$.

From (5.27), the marker directions in the two poses are

$$\phi_{\text{init}} = \phi(\theta_{\text{init}}) = \theta_{\text{init}} + \phi_r \tag{5.28}$$

$$\phi_{\text{load}} = \phi(\theta_{\text{load}}) = \theta_{\text{load}} + \phi_r \tag{5.29}$$

Subtracting these expressions gives

$$\phi_{\text{load}} - \phi_{\text{init}} = (\theta_{\text{load}} + \phi_r) - (\theta_{\text{init}} + \phi_r) = \Delta\theta \tag{5.30}$$

Equation (5.30) is the first key result: the change of apparent link angle $\Delta\theta$ is exactly equal to the change in marker direction between initial and loaded poses. The unknown offset angle ϕ_r cancels out. Therefore, the precise position of the marker on the link does not affect $\Delta\theta$ as long as the link is rigid and the marker is rigidly attached.

The geared rotational joints of the robot do not rotate as a simple pin joint: the motion is generated by a symmetric isosceles linkage between the joints centre B, an intermediate point P on the gear mechanism, and the outer link centre C (Figure 5.13). Let the horizontal through B be the reference direction. Consider α the true joint angle at the geared mechanism, which is the deflection of the coupler at P with respect to the reference, and β the base angle at B and C inside the isosceles triangle. By the exterior angle theorem applied at P, the exterior angle α equals the sum of the two opposite interior angles: $\alpha = \beta + \beta = 2\beta$.

At B, the angle between the reference horizontal and the link centreline BC is the sum of the joint angle and the base angle: $\theta = \alpha + \beta$.

Combining the two relations gives

$$\theta = 2\beta + \beta = 3\beta \quad \Rightarrow \quad \beta = \frac{\theta}{3} \tag{5.31}$$

and therefore

$$\alpha = 2\beta = \frac{2}{3}\,\theta \rightarrow \Delta\alpha = \frac{2}{3}\Delta\theta \tag{5.32}$$

This relation is linear and does not depend on the actual value of β, so the same factor $2/3$ applies to both absolute angles and angle changes. In the stiffness identification, it is therefore used

$$\Delta\alpha = \frac{2}{3}\left(\phi_{\text{load}} - \phi_{\text{init}}\right) \tag{5.33}$$

as the estimate of the true joint rotation for each trial. In the multi-joint chain, the same construction is applied to each joint, and the resulting joint rotations $\Delta\alpha_1$, $\Delta\alpha_3$ and $\Delta\alpha_5$ are used to compute the rotational stiffness.

With the kinematic changes $\Delta\theta_i$ identified, they can now be related to the applied gravitational torques to define the rotational stiffness of each joint.

Once the rotation $\Delta\theta_i(W,F_t)$ has been identified for joint i under payload W and tension F_t, the apparent rotational stiffness is computed as:

$$k_{\theta i}(W,F_t) = \frac{\tau_i(W)}{\Delta\theta_i(W,F_t)} \tag{5.34}$$

where the torque $\tau_i(W) = F_g(W)\, r_i$ is obtained from the known lever arm r_i and gravitational force $F_g(W)$.

To understand how these individual joint stiffnesses aggregate to determine the total end-effector deflection, the manipulator is analysed as a series of compliant elements.

Because the joints bend in the same vertical plane and deflections are small, each bending joint can be modelled as a linear torsional spring. A rotation $\Delta\theta_i$ at joint i produces an approximately vertical displacement of the tip

$$\Delta z_i \approx r_i\, \Delta\theta_i. \tag{5.35}$$

Summing the contributions of all bending joints gives

$$\Delta Z_{\text{tip}} \approx \sum_{i=1}^{N} \Delta z_i \approx \sum_{i=1}^{N} r_i\, \Delta\theta_i = F_g \sum_{i=1}^{N} \frac{r_i^2}{k_{\theta i}} \tag{5.36}$$

A convenient way to interpret the joint contributions is using the *effective vertical compliance* (C_i) of joint i:

$$C_i(W,F_t) := \frac{\Delta z_i(W,F_t)}{F_g(W)} \approx \frac{r_i^2}{k_{\theta i}(W,F_t)} \quad [\text{m/N}] \tag{5.37}$$

and the corresponding *compliance share*

$$\gamma_i(W,F_t) = \frac{C_i(W,F_t)}{C_{\text{tip}}(W,F_t)} = \frac{\dfrac{r_i^2}{k_{\theta i}(W,F_t)}}{\displaystyle\sum_{j\in\{1,3,5\}} \frac{r_j^2}{k_{\theta j}(W,F_t)}} \tag{5.38}$$

which satisfies $\sum_{i\in\{1,3,5\}} \gamma_i = 1$.

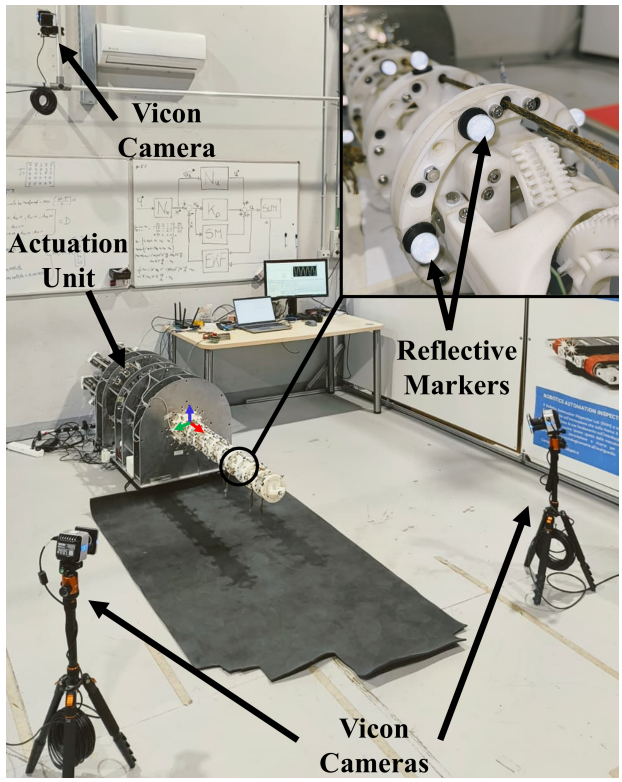


Figure 5.14 Experimental setup for stiffness testing. The red, green, and blue arrows represent the x, y, and z axis.

With the analytical definitions established, the following section outlines the physical setup and procedure for collecting the necessary kinematic data for validation.

5.4.2 Experimental Protocol

To measure the manipulator positioning error under the influence of gravity, a set of experiments was performed by applying different weights to the end-effector and increasing the tension levels at the tendons. The experimental setup is shown in figure 5.14.

The positioning error was captured using a Vicon Motion Capture (MoCap) system, which provides high accuracy and reliability. As the experiment measures steady-state deflection, the system's static positioning accuracy is the relevant metric, which is reported as a Mean Absolute Error (MAE) of 0.15 mm with variability < 0.025 mm [146].

The tested payloads are $W_1 = 236\ g, W_2 = 671\ g$, and $W_3 = 1047\ g$, with a scale resolution of ± 1 g. Reference tensioner forces are $F_t \in \{0, 50, 150, 250, 350\}$ N and are monitored by a KM26z load cell with Full Scale (FS) of 500 N, rated output 1 mV/V,

accuracy class 1%, relative linearity error 0.3% FS and hysteresis error 0.2% FS [147]. For each weight-tension condition, $N = 10$ independent trials were executed, each paired with its own initial pose. Steady-state vertical deflections and joint rotations were computed as the mean of the last 25% of frames in each trial. Furthermore, before each test trial, the manipulator was moved along a predefined path, ensuring that each joint moved in both directions and returned to its original position. This allows the tendon tensions to return to their initial, repeatable condition. This way, no measure is affected by the previous load applied to the robot, which might affect the tension on the tendons and make them appear stiffer than they are, thus affecting the measure. The deflection measure ΔZ is the change in the vertical position along the arm relative to the paired initial pose.

Once the raw motion data is obtained, statistical processing is required to filter noise and extract consistent deflection metrics.

Each experiment condition is defined by the end-effector payload W and a reference tendon tension F_t. Vicon recordings are down-selected to the last quarter of frames to remove transients. Let the total frames in a trial be N_{tot} and the retained portion be $q = 0.25$, so the number of frames used per signal average is $N_f = qN_{\text{tot}}$. For trial $n \in \{1,...,N\}$ and link $\ell \in \{1,\dots,5\}$ (with $\ell = 0$ denoting the base), the per-trial vertical position mean in the last N_f frames is

$$\begin{aligned} \bar{Z}^{\text{load}}_{n,\ell} &= \frac{1}{N_f} \sum_{t \in \mathscr{I}_{\text{last 25\%}}} Z^{\text{load}}_{n,\ell}(t) \\ \bar{Z}^{\text{init}}_{n,\ell} &= \frac{1}{N_f} \sum_{t \in \mathscr{I}_{\text{last 25\%}}} Z^{\text{init}}_{n,\ell}(t) \end{aligned} \tag{5.39}$$

where *load* and *init* denote, respectively, the loaded and the initial unloaded recordings paired to the same trial.

The raw deflection for trial n and link ℓ is the difference of means

$$dZ_{n,\ell} = \bar{Z}^{\text{load}}_{n,\ell} - \bar{Z}^{\text{init}}_{n,\ell} \tag{5.40}$$

To cancel any global platform/camera drift, all links are referenced to the base:

$$\Delta Z_{n,\ell} = dZ_{n,\ell} - dZ_{n,0} \qquad \Delta Z_{n,0} \equiv 0 \tag{5.41}$$

For a fixed condition (W, F_t), the reported deflection per link is the mean across trials

$$\mu_{W,F_t,\ell} = \frac{1}{N}\sum_{n=1}^{N} \Delta Z_{n,\ell} \qquad \ell = 1,\ldots,5 \tag{5.42}$$

Repeatability across the N trials is summarised by the sample standard deviation

$$\sigma_{W,F_t,\ell} = \sqrt{\frac{1}{N-1}\sum_{n=1}^{N}\left(\Delta Z_{n,\ell} - \mu_{W,F_t,\ell}\right)^2} \tag{5.43}$$

and by the Standard Error (SE) of the mean:

$$\mathrm{SE}_{W,F_t,\ell} = \frac{\sigma_{W,F_t,\ell}}{\sqrt{N}} \tag{5.44}$$

If the reported MoCap error is modelled as zero-mean noise with standard deviation $\sigma_{\mathrm{V}} \approx 0.15\,\mathrm{mm}$ on Z at each frame, then averaging N_f frames reduces the standard deviation of each mean position to $\sigma/\sqrt{N_f}$. The base-referenced deflection for one trial

$$\Delta Z_{n,\ell} = (\bar{Z}^{\mathrm{load}}_{n,\ell} - \bar{Z}^{\mathrm{init}}_{n,\ell}) - (\bar{Z}^{\mathrm{load}}_{n,0} - \bar{Z}^{\mathrm{init}}_{n,0})$$

is a difference of four such means, so its measurement noise variance is

$$\mathrm{var}\left[\Delta Z_{n,\ell}\right]_{\mathrm{Vicon}} \approx \frac{4\,\sigma_{\mathrm{V}}^2}{N_f} \qquad \sigma_{\Delta Z,\mathrm{Vicon}} \approx \frac{2\,\sigma_{\mathrm{V}}}{\sqrt{N_f}} \tag{5.45}$$

For the present experiments $N_f \approx 0.25\,N_{\mathrm{tot}}$ is on the order of a few hundred frames, so $\sigma_{\Delta Z,\mathrm{Vicon}}$ is approximately $10^{-2}\,\mathrm{mm}$. The total standard deviation of $\Delta Z_{n,\ell}$ can therefore be written as

$$\sigma^2_{\Delta Z,\mathrm{tot}} \approx \sigma^2_{W,F_t,\ell} + \sigma^2_{\Delta Z,\mathrm{Vicon}} \tag{5.46}$$

i.e. as the quadrature sum of trial-to-trial scatter and the Vicon measurement floor. In practice $\sigma_{\Delta Z,\mathrm{Vicon}}$ is much smaller than both the mean deflections and the empirical spread across trials, so

$$\sigma_{\Delta Z,\mathrm{tot}} \approx \sigma_{W,F_t,\ell} \qquad \sigma_{\mu,\mathrm{tot}} = \frac{\sigma_{\Delta Z,\mathrm{tot}}}{\sqrt{N}} \approx \mathrm{SE}_{W,F_t,\ell} \tag{5.47}$$

The reported uncertainty on the mean deflections is therefore dominated by trial-to-trial variability.

Uncertainties on the joint stiffnesses are obtained by first quantifying the uncertainty on the identified joint rotations $\Delta\alpha_i(W, F_t)$ and then propagating it through the stiffness

Link	**Tension F_t [N]**				
	0	50	150	250	350
			W = 236 *g*		
L_1	-0.33 ± 0.03	-0.21 ± 0.03	-0.13 ± 0.03	-0.11 ± 0.03	-0.09 ± 0.03
L_2	-0.78 ± 0.03	-0.51 ± 0.04	-0.32 ± 0.04	-0.24 ± 0.03	-0.20 ± 0.03
L_3	-1.47 ± 0.05	-0.86 ± 0.07	-0.55 ± 0.05	-0.42 ± 0.05	-0.35 ± 0.04
L_4	-2.03 ± 0.05	-1.20 ± 0.08	-0.77 ± 0.05	-0.60 ± 0.05	-0.52 ± 0.03
L_5	-2.84 ± 0.12	-1.63 ± 0.09	-1.06 ± 0.05	-0.81 ± 0.05	-0.72 ± 0.03
			W = 671 *g*		
L_1	-1.03 ± 0.03	-0.89 ± 0.04	-0.57 ± 0.04	-0.39 ± 0.03	-0.34 ± 0.04
L_2	-2.43 ± 0.04	-2.08 ± 0.06	-1.28 ± 0.08	-0.91 ± 0.05	-0.80 ± 0.05
L_3	-4.44 ± 0.06	-3.47 ± 0.12	-2.27 ± 0.11	-1.64 ± 0.07	-1.41 ± 0.07
L_4	-6.33 ± 0.08	-4.96 ± 0.15	-3.16 ± 0.15	-2.31 ± 0.09	-1.97 ± 0.08
L_5	-9.87 ± 0.54	-6.69 ± 0.21	-4.27 ± 0.20	-3.12 ± 0.10	-2.67 ± 0.12
			W = 1045 *g*		
L_1	-1.68 ± 0.04	-1.51 ± 0.19	-1.17 ± 0.05	-0.78 ± 0.05	-0.58 ± 0.05
L_2	-3.95 ± 0.07	-3.70 ± 0.09	-2.68 ± 0.06	-1.77 ± 0.14	-1.39 ± 0.07
L_3	-7.25 ± 0.09	-6.54 ± 0.14	-4.62 ± 0.08	-3.11 ± 0.25	-2.41 ± 0.09
L_4	-10.43 ± 0.12	-9.17 ± 0.20	-6.35 ± 0.15	-4.48 ± 0.22	-3.38 ± 0.13
L_5	-17.69 ± 0.55	-12.52 ± 0.28	-8.55 ± 0.19	-6.02 ± 0.33	-4.83 ± 0.24

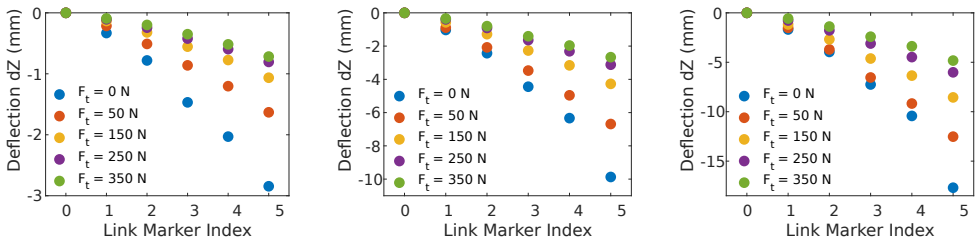
Table 5.4 Mean deflections (Δz) and their respective uncertainty for each link marker and all tested weights. Δz is expressed in *mm*. Subscript 1,...,5 represent the link index.

equation by first-order linearisation. For each joint and condition (W, F_t) the empirical standard deviation $\sigma_{\Delta\alpha_i}(W, F_t)$ across the N trials is computed and added in quadrature to a measurement term $\sigma_{\Delta\alpha_i,\mathrm{V}}$ obtained by propagating the Vicon positional accuracy through the atan2 mapping and the linear gear relation $\Delta\alpha_i = \frac{2}{3}\Delta\theta_i$. In the present experiments $\sigma_{\Delta\alpha_i,\mathrm{V}}$ is much smaller than $s_{\Delta\alpha_i}$, so the errors on $k_{\theta i}$ are effectively dominated by trial-to-trial variability.

The application of this protocol produced a comprehensive dataset characterising the manipulator's behaviour, starting with the raw vertical deflections.

5.4.3 Manipulator Deflection and Stiffness Analysis

Table 5.4 shows the robot deflections for each one of its links under different weights and pretension values, while Figure 5.15 shows the vertical displacement of each marker placed in each link of the manipulator for each W at each F_t.



(a) W = 236 g (b) W = 671 g (c) W = 1046 g

Figure 5.15 Marker displacements for each link, with different weights for each tension level. Index=0 represents the marker at the base of the robot, while Index=5 represents the marker at the tip of the last link of the robot. The plots are not to scale.

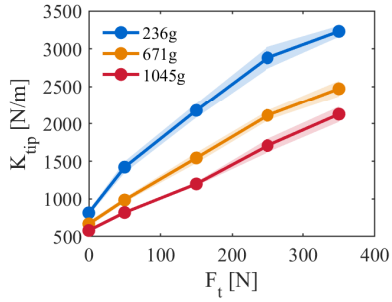


Figure 5.16 Tip translational stiffness $K_{\text{tip}}(W, F_t)$ versus tensioner force F_t for the three payloads. Error bars indicate 1σ over 10 trials.

As shown in the table and plots, the robot deflection under weight decreases significantly with tendon tension. The results show that the end-effector vertical deflection with a payload of 1.045 kg, decreases by almost 52 % with only 150 N of tensioning force applied by the tensioner actuator. This reduction becomes almost 73 % if the tensioner delivers a tensioning force of 350 N, which would bring the manipulator to deflect by only 4.8 mm.

For this system, $F_t = 150$ N is a good compromise, since at that pretension value the deflection is reduced by half, while deciding to increase pretension to 350 N would double the internal structural stresses while providing only an additional 20% deflection reduction.

By combining these deflection measurements with the applied payload values, the effective translational stiffness at the tip can be quantified.

Figure 5.16 shows the measured K_{tip} as a function of the global tension command F_t for three payloads (236 g, 671 g, 1045 g) with the coloured shades indicating the uncertainty. Uncertainties on K_{tip} are obtained by propagating the total vertical deflection

uncertainty $\sigma_{\Delta Z,\text{tot}}$ through Eq. (5.4.1) using a first-order linearisation. For each condition (W, F_t) the approximation is

$$\sigma^2_{K_{\text{tip}}} \approx \left(\frac{\partial K_{\text{tip}}}{\partial F_g}\right)^2 \sigma^2_{F_g} + \left(\frac{\partial K_{\text{tip}}}{\partial \Delta z_{\text{tip}}}\right)^2 \sigma^2_{\Delta Z,\text{tot}} \tag{5.48}$$

$$\approx \left(\frac{\sigma_{F_g}}{\Delta z_{\text{tip}}}\right)^2 + \left(\frac{F_g\, \sigma_{\Delta Z,\text{tot}}}{\Delta z^2_{\text{tip}}}\right)^2 \tag{5.49}$$

where σ_{F_g} is the uncertainty of the weight measurements.

At $F_t = 0$ the arm is highly compliant, especially under the heaviest payload. Increasing F_t produces a strong stiffening effect: in the low-tension regime, modest increases in F_t lead to large gains in K_{tip}. For instance, raising F_t from 0 to 150 N roughly quadruples the tip stiffness for the heaviest payload.

Physically, this is the regime in which slack and free play are being removed: tendon slack is taken up, tendon paths are straightened, and joints are pulled into a tighter configuration. Once the tendons are fully taut, further increases in F_t mainly stretch the tendons and links elastically. This leads to diminishing returns: beyond about 150 N the slope $\partial K_{\text{tip}}/\partial F_t$ decreases, and additional 100 N of tension yield progressively smaller stiffness gains. The resulting "steep then saturating" nonlinearity is typical of tension-based stiffening: the system transitions from a geometry-dominated regime (high gain in stiffness) to a material-dominated regime (low gain).

To quantify the achievable range, a tip stiffness modulation index is defined as

$$M_{\text{tip}}(W) = \frac{K_{\text{tip}}(W, F_t^{\max})}{K_{\text{tip}}(W, 0)} \tag{5.50}$$

For the lightest non-zero payload (W_1), $M_{\text{tip}} \approx 4$ is obtained, and for W_2 and W_3, $M_{\text{tip}} \approx 3.5$. Thus, the single tensioner can increase tip stiffness by a factor of three to four over the tested range, which is substantial for a purely tendon-based mechanism.

Payload influences not only the absolute stiffness but also the modulation gain. At low payloads, friction and intrinsic structural stiffness provide a baseline rigidity even with $F_t = 0$, so $K_{\text{tip}}(W, 0)$ is relatively large and additional tension acts on an already "pre-loaded" structure. At high payloads, gravity fully sags the arm when untensioned, so much of the tensioner's effort goes into supporting the weight rather than eliminating play, and M_{tip} is slightly smaller. In practice, this means that the mapping $F_t \mapsto K_{\text{tip}}$ is load-dependent: the same change in F_t produces different stiffness gains depending on W.

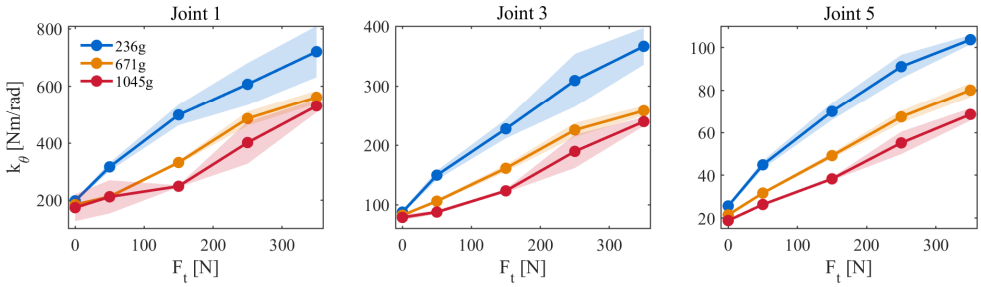


Figure 5.17 Rotational stiffness of joints 1, 3, and 5, for the three payloads. The coloured bands represent 1σ, while the points represent the median.

While the tip stiffness demonstrates the tensioner's global efficacy, analysing the internal distribution of stiffness requires examining rotational stiffness trends at the joint level.

Figure 5.17 reports $K_{\theta i}$ versus F_t for joints 1, 3, and 5, using the geometric method. Each curve shows the median over the N trials, with error bars representing 1 standard deviation and individual trial points overlaid.

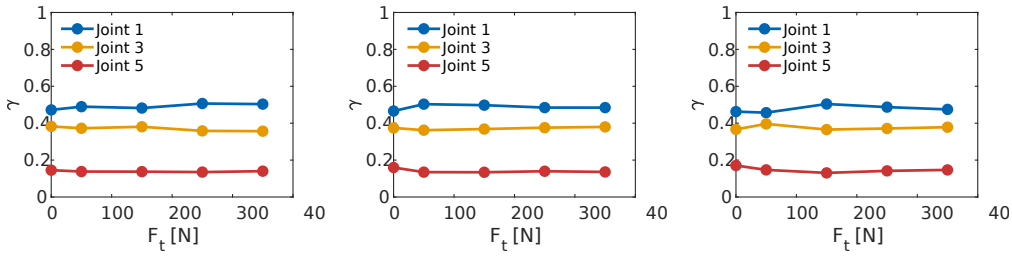
In terms of absolute values, Joint 1 shows a clear, almost linear and monotonic increase in stiffness with F_t for all payloads. Joint 3 also stiffens with increasing F_t, with stiffness values that are systematically lower than those of joint 1 but follow a similar near-linear trend, while Joint 5 is consistently much softer than joints 1 and 3. Physically, the distal joint stiffens monotonically under global tensioning but remains comparatively compliant in absolute terms.

While the absolute stiffness values follow the expected structural order (base stiffer than tip), the relative impact of the tensioning system reveals a different trend. Table 5.5 presents the percentage increase in stiffness for each joint across the tested payloads.

Joint	$\Delta K_{\%w1}$	$\Delta K_{\%w2}$	$\Delta K_{\%w3}$
J1	264.7	204.5	205.4
J3	317.2	212.1	203.5
J5	304.1	272.7	264.4

Table 5.5 Percentage increase in stiffness for each joint and payloads W_1, W_2, W_3.

As shown in the table, joint 5 has the biggest percentage increase in stiffness, while joints 1 and 3 have comparable increases, with joint 3 being slightly more efficient. This inversion of efficiency compared to absolute stiffness can be attributed to the specific routing of the tensioning system. In this prototype, the tensioning tendon path to Joint 1 is the longest, whereas the path to Joint 5 is the shortest. Since friction and hysteresis



(a) Compliance share for W_1 (b) Compliance share for W_2 (c) Compliance share for W_3

Figure 5.18 Compliance share vs. Tension for all payloads and joints

losses accumulate with tendon length and contact surface area, the efficiency of tension transmission inevitably degrades for longer routes. Consequently, the global tensioner is actually most effective at stiffening the distal joints in relative terms, even though their absolute stiffness remains limited by their mechanical design.

To determine whether the tensioning force alters the relative flexibility distribution along the arm or simply scales it, the compliance share, γ_i, is analysed. Compliance share is reported because serial elements add in compliance ($C_{eq} = \Sigma C_i$), allowing a direct comparison of how each joint contributes to global flexibility under different pretension levels.

Figure 5.18 reports γ_i for all payloads. Across all (W, F_t) conditions, the way tip compliance is shared between the three bending joints is very stable. Joint 1 always provides the largest fraction of tip compliance, with γ_1 staying roughly between 0.45 and 0.52 for all payloads and tensions. Joint 3 contributes a similar amount, typically $\gamma_3 \approx 0.35$-0.40, whereas joint 5 has the smallest tip compliance share, with γ_5 in the range 0.12-0.18. The dependence of γ_i on F_t is weak: the curves shift by only a few percentage points and do not show a clear trend with the payload.

This behaviour is easier to interpret together with the rotational stiffness curves in Figure 5.17. Although $K_{\theta 1}$, $K_{\theta 3}$ and $K_{\theta 5}$ vary strongly and nonlinearly with both F_t and W, the effective tip compliances change in a nearly proportional way across joints. Global tensioning therefore acts mainly as a uniform gain on the overall stiffness: it scales all C_i up or down while keeping their ratios almost constant, so that the compliance distribution along the arm remains close to 50% for joint 1, 35% for joint 3 and 15% for joint 5. In absolute terms, joint 5 is the softest joint (lowest K_{θ_i}), but its short lever arm makes its contribution to tip motion modest; the base joint dominates the tip compliance share, with the mid-joint still carrying a substantial and essentially constant share. The experimental compliance distribution remains invariant across tension levels and aligns

with the analytical series-compliance model, which predicts that the proximal joint contributes approximately 50% of the deflection due to lever-arm scaling. This result, combined with the percentage increase in stiffness, indicates that the global tensioning strategy uniformly scales the entire chain's rigidity. The distal joints are not "left behind" by the tensioner; rather, their lower absolute stiffness results from intrinsic structural geometry, not a lack of actuation efficiency. This consistency validates the efficiency of the tensioning and the optimised tendon routing, confirming that critical stiffening forces are successfully transmitted to the distal joints without significant degradation due to frictional losses along the robot structure.

The experimental analysis produces key insights that simplify the system's control design and mechanical optimisation. A central result is the observed invariance of the compliance shares, γ_i, across all tension levels and payloads. This invariance shows that the global tensioning input behaves as a scalar gain, scaling the system's stiffness uniformly while leaving its spatial pattern unchanged. This reduces the complex multi-joint compliance model to a single scalar function. This stable compliance pattern indicates that proximal joint deflection can reliably predict the deflection state of distal segments.

The findings also demonstrate that the tensioning architecture successfully transmits the stiffening effect to the distal joints, as evidenced by their marked increase in stiffness. Consequently, in later design stages, actuation and structural geometry can be optimised separately: the tensioning system can be scaled to meet overall force demands, while the link lever arms can be adjusted to set the local compliance distribution, without concern that transmission losses will negate these geometric changes.

This chapter experimentally characterised tension-transfer behaviour, hysteresis, tracking error, and load-dependent stiffness modulation. The findings establish practical pretension ranges and underscore the trade-off of relying solely on tensioning to achieve high stiffness. Chapter 6 introduces an underwater-focused design workflow in which mass reduction and buoyancy-aware design reduce the necessary pretension while maintaining structural integrity.

CHAPTER 6

LORY-8JP: OPTIMISATION AND UNDERWATER ADAPTATION

In collaboration with the Marine Technology department at Delft University of Technology, a review of current underwater robotics and HR manipulators revealed that research on HR or snake-like robots for offshore, marine, and underwater applications remains limited. Traditional underwater robotic systems, such as Autonomous Underwater Vehicles (AUVs) and Remotely Operated Vehicles (ROVs), play an essential role in subsea maintenance, repair, and inspection [148, 149]. However, these technologies often struggle with the precision and adaptability needed to operate in tight spaces, such as between closely spaced underwater pipelines or within shipwrecks [150]. Underwater, snake-like robots can help overcome these challenges. Their adaptable, elongated, and highly manoeuvrable structures make them well-suited for tasks such as inspection and maintenance in offshore energy installations [151, 152]. Unlike conventional ROVs or AUVs, these robots can access hard-to-reach areas, including the interiors of complex underwater structures, where traditional systems would struggle.

This study addresses these challenges by providing a design framework for a tendon-driven HR manipulator optimised for underwater deployment. This study is also detailed in [153]. The aim is to design an underwater manipulator that can be attached to an ROV or AUV, combining the underwater vehicle's speed and water navigation capabilities with the HR manipulator's manoeuvrability and reach. This work advances prior research by integrating data-driven stress prediction with hydrodynamic shape optimisation for underwater HR manipulators while introducing modular buoyancy strategies.

Before going into the detailed design and optimisation analysis, a state-of-the-art overview of underwater serial robots is presented.

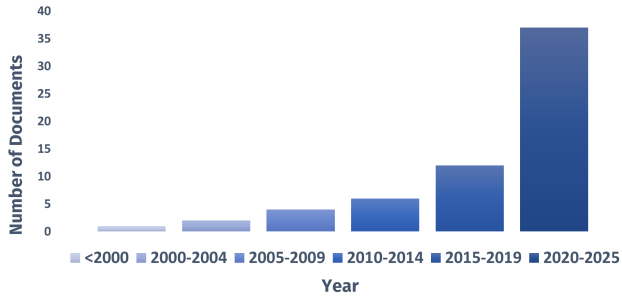


Figure 6.1 Number of yearly documents on snake-like underwater robots

6.1 State of the Art on Underwater Manipulators

As discussed in the detailed survey presented by the author [154], two families of underwater robots have been identified: Tethered and Untethered Underwater Robots. Untethered mobile robots can navigate without being fixed to a platform, allowing them to move like eels. On the contrary, tethered robots rely on a fixed platform and can not navigate without an external thrust base, acting as robotic arms. In the family of untethered robots, two categories of different types of robots have been classified: Thrusted Robots (TR) and Swimming Robots (SR). Within these categories, a further classification into sub-categories was made based on fundamental characteristics of the actuation system. Regarding TRs, two subcategories were recognised: thrusted robots with rigid joints and thrusted robots with soft joints. Regarding SRs, four sub-categories were identified: swimming robots with rigid joints, swimming robots with compliant joints, swimming robots with soft joints, and a sub-category including a few other particular types of swimming robots. Likewise, three categories have been identified within the family of tethered robots: Compliant Robotic Arms (CRA), Rigid-Joint Robotic Arms (RJRA), and Soft Robotic Arms (SRA). This classification was based on the design, actuation, and motion transmission strategies. Figure 6.2 shows the percentages of documents found in each category of both robot families.

This field of robotics is relatively new, and began to be explored in the 1990's, as demonstrated by the survey results, and shown in figure 6.1. It is shown that before the year 2015, research in this field remained quite stagnant, then a significant rise in research papers began from 2021.

While all the mentioned underwater robot categories were extensively analysed in [154], this dissertation considers only underwater manipulators (tethered robots), as they are relevant to the project's scope.

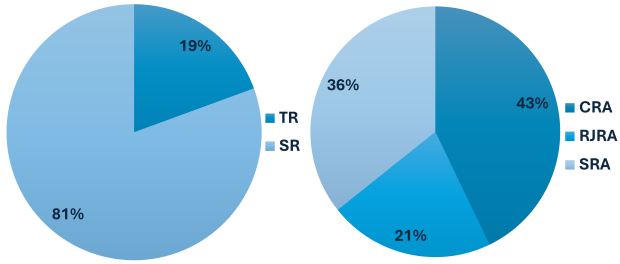
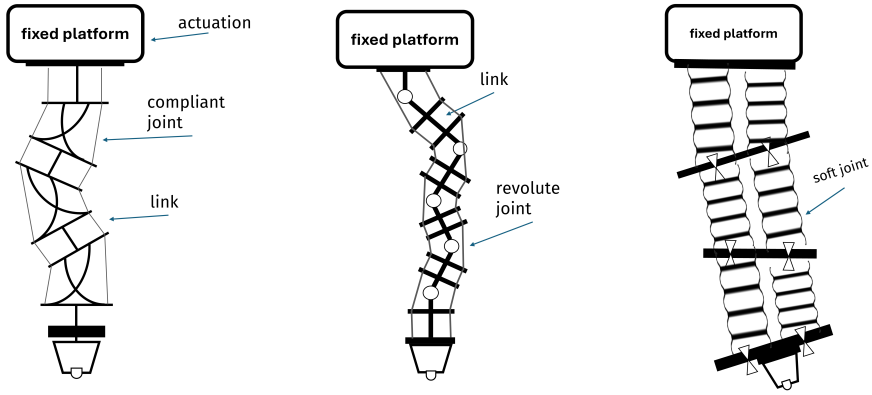


Figure 6.2 Percentages of research papers found on underwater robot designs for each category. Left: Untethered Robots. Right: Tethered Robots.



(a) CRA (b) RJRA (c) SRA

Figure 6.3 Schematic representations of tethered underwater robots

This category includes underwater manipulators, which are robotic arms fixed to a platform: CRAs, RJRAs, and SRAs. Designed for tasks that require dexterity and precision, such manipulators are often driven by tendons, allowing continuous bending and a high degree of control in constrained underwater spaces while offering high payloads. Figure 6.3 shows the conceptual schematic designs for each category of tethered underwater robots.

6.1.1 Compliant Robotic Arms

CRAs are typically designed as continuum snake-like robots with compliant joints, usually actuated by tendons to maintain a lightweight profile. These systems often prioritise structural flexibility to navigate complex, unstructured marine environments. By employing continuous backbones and inherent compliance, these systems offer superior

adaptability for operations in confined spaces and provide safe interaction with delicate subsea infrastructure.

Xue et al. [155] presented an underwater snake arm robot composed of 10 modular segments, each with a cross-axis universal flexure joint that allows for two rotational DOF per segment. Each segment is connected via a series of tendons running through holes in the joint discs. The robot employs a driving motor-synchronous belt-cable system located at the base to actuate the tendons. This system allows a single motor to control two tendons simultaneously, providing precise movement. Similarly, Sitler et al. [156] introduced a modular, tendon-driven continuum manipulator for underwater ROV operations, designed to be open-source and reconfigurable, aiming to lower development challenges while maintaining precise manoeuvrability. Guglielmino et al. [157] and Jia et al. [158] presented hydraulically actuated continuum arms for subsea inspection, offering a fluidic alternative to tendon-driven systems, with a focus on compliant motion, onboard water-powered actuation and pressure-force analysis to enhance bending flexibility and output efficiency. Another tendon-driven manipulator with compliant joints is proposed by Xue et al. [159]. It consists of seven sections with 14 *DOF*. It utilises a rack and pinion structure to control two tendons per joint, thereby significantly reducing the number of motors required for actuation. The manipulator presented by Li et al. [160] is also a tendon-driven manipulator with compliant joints designed to house an optical fibre probe for near-infrared underwater spectral detection. The manipulator is driven by 8 steering engines that control the winding pulleys, and incorporates a compressed air system that blows water away from the probe's detection path, allowing for accurate infrared spectral analysis by minimising water interference. Ma et al. [161] proposed a tendon-driven dual-arm continuum robot with 6 DOF per arm. Inside each section are flexure hinges in a diamond shape, flexible leaf spring-like elements distributed evenly around a central ball joint. This way, stiffness can be increased, and hence, kinematic accuracy is improved. The hinges allow the robot to achieve orthogonal rotational motion and maintain precision during operation. The tendons are actuated by motors housed in an actuation box located under the ROV, maintaining the robot's centre of mass stable.

6.1.2 Rigid-Joint Robotic Arms

Unlike compliant arms that rely on material deformation, RJRAs employ a series of discrete, stiff links connected by distinct kinematic pairs, such as universal or revolute joints. This mechanical structure offers superior structural rigidity and payload capacity,

enabling the robot to withstand underwater currents and generate higher forces while navigating complex, confined environments.

Barbieri et al. [162] designed an underwater robotic arm driven by servomotors. The arm utilises a worm gear mechanism to prevent retrograde motion, offering precise control and simplified component design. Another tendon-driven HR manipulator is proposed by Tang et al. [51], consisting of multiple cylindrical joint modules connected by universal joints, which enable the manipulator to bend, rotate, and extend. The manipulator's length and the number of joints can be customised based on the specific underwater tasks. The manipulator features a hollow, tubular structure made from aluminium alloy, which provides a lightweight and pressure-resistant design, making it suitable for underwater applications. Sourkounis et al. [163] introduced a similar, rigid-link tendon-driven manipulator for deep-sea sediment sampling. It consists of stacked, bevelled cylindrical links connected by swivel joints, forming an adaptable structure capable of bending continuously along its length. The hollow centre contains the sampling tube, allowing for a compact design. All parts are made from corrosion-resistant plastic, and the design eliminates air pockets to withstand high underwater pressure.

6.1.3 Soft Robotic Arms

SRAs draw direct inspiration from the anatomy of cephalopods, such as octopuses and squids, to achieve continuous deformation and infinite DOF. Unlike rigid kinematic chains, these manipulators utilise inherently soft materials, such as elastomers and flexible composites, to distribute actuation along the entire body. This morphological compliance allows them to wrap around objects and squeeze through gaps, making them ideal for unstructured underwater environments.

Kang et al. [164] presented a design to replicate the octopus arm's anatomy, with an HR structure with multiple segments capable of elongating, contracting, and bending at any point along its length. Each segment of the manipulator is constructed as a parallel mechanism, comprising a fixed base, a moving platform, four actuated "limbs", and a central support rod. The limbs function like linear hydraulic actuators, providing the manipulator 2 rotational DOF and one translational DOF. The robot comprises 20 serially connected segments, allowing for extensive reach and adaptability, much like a real octopus arm. Gong et al. [165] proposed a soft robotic arm composed of two segments, each made of modular soft chambers that allow for 3D bending. These chambers are actuated pneumatically, creating fluidic channels to control bending motions. The design includes corrugated textures along the arm's surface to reduce unwanted radial expansion

(ballooning) of the chambers. This corrugated structure also incorporates embedded rubber tendons to further control and limit radial expansion while allowing bending. The entire soft robotic arm is enclosed in a cylindrical shape to streamline its movement in the water, further minimising drag. The arm is actuated through a 7-way pneumatic valve system, allowing complex 3D manipulations. An innovative feature of this system is the incorporation of an angle correction model, which compensates for deformations caused by the weight of the soft material and external loads.

Another robot with a soft structure and fibre-reinforced actuators is presented by Gong et al. [166], which introduces an opposite bending and extension design comprising two bending segments, one elongating segment, and a soft gripper at the end. Each bending segment has three individual chambers with a multi-channel pneumatic system to control the pressure, allowing bidirectional bending to achieve complex movements in underwater environments. The fibreglass-reinforced elastomer actuators make the manipulator lightweight and flexible. The underwater manipulator designed by Emet et al. [14] is inspired by the tentacles of squids and cuttlefish, with four soft, tendon-actuated limbs. Two of the limbs function as manipulating arms for tasks such as reaching, gripping, and pulling, while the other two function as tentacles for visual feedback and navigation, and contain an underwater camera and lighting system. The actuators consist of four tendons that pass longitudinally through each limb, contained within silicone tubes to protect the soft limbs from wear. Electromechanical systems inside the robot's head actuate the tendons within each limb. The four-tendon configuration simplifies control strategies while providing sufficient dexterity for underwater manipulation tasks, such as gripping.

A unique and hybrid underwater manipulator is presented by Zheng et al. [167], inspired by the octopus arm and incorporates a continuum robotic arm structure consisting of multiple flexible segments. Each segment contains both longitudinal and radial actuators, mimicking the anatomy of an octopus arm, allowing for bending, elongation, and contraction in various directions. The arm is entirely built with soft/flexible materials, reproducing the octopus's ability to perform dexterous movements. The longitudinal actuators use tendons, with 12 tendons of different lengths attached to three locations along the arm, driven by external servomotors. The radial actuators use SMA springs inside the body at 18 locations along the arm. These SMAs replicate the radial muscle contraction found in an octopus, allowing the arm to change its diameter and perform complex movements.

6.1.4 Design Considerations

Tethered underwater manipulators offer various advantages depending on their mechanical structure, ranging from high flexibility in continuum arms to precision and strength in rigid-joint structures. Their design reflects specific operational needs, where the balance between compliance, manoeuvrability, and payload capacity drives the design choices. Continuum robotic arms offer high manoeuvrability but suffer from tendon routing friction and modelling continuum mechanics, while rigid-joint designs provide better payload capacity but are less flexible. Soft robotic arms, although suitable for delicate object interactions, are limited in terms of load-bearing capacity and control accuracy. Many of these manipulators have modular segments, allowing customisation and easy replacement of damaged parts. The rigid segments of snake-arm manipulators provide greater structural robustness than purely soft-actuated designs, compliant joints, or smart material structures, making them more durable in harsh underwater conditions. However, this robustness comes at the cost of increased weight and lower energy efficiency.

Underwater rigid-link manipulators allow precise movements, making them ideal for tasks such as inspection, maintenance, or exploration in intricate underwater structures, including pipelines, coral reefs, or shipwrecks. The majority of snake-arm underwater robots are tendon-actuated. Tendon-driven robots reduce coupling with underwater vehicles, as having the actuators at the base doesn't affect the vehicle's stability and control by generating reactive forces and moments that can challenge position and orientation maintenance. However, unlike propulsion-driven robots, snake-arm rigid-link manipulators lack the propulsion power for high speeds and/or long-distance travel. In contrast, they perform best in tasks that are stationary or require precise manipulation.

Lightweight, compact actuation units remain a critical area for improvement, as current designs often impose constraints on overall system size and payload capacity. The actuator size in these systems needs to be optimised, as it often requires a large, bulky actuation unit. This way, an ROV can be integrated with the actuation unit, resulting in a hybrid thruster-actuated unit and a snake-arm manipulator that can be propelled to reach remote environments, remaining in place while the robot arm performs related inspection or maintenance tasks. Furthermore, more reliable analyses of hydrodynamics and fluid-structure interactions are necessary to accurately predict robot performance under varying underwater conditions.

Based on these literature findings, the following section outlines the design framework of the HR manipulator considered here for underwater adaptation, which is guided by

the following requirements, based on the experimental findings of Chapter 5 and the structural constraints of Chapter 4:

- Modular scalability to an 8-joint arm (LORY-8JP) using the same modular design, and the same module dimensions ($D_{ext} = 130$ mm, $l = 100$ mm, $L = 1.6$ m).
- Payload capability consistent with the stiffness and tracking limits identified in Chapter 5.
- Mass reduction to enable mounting on an ROV and to reduce required pretension through buoyancy and hydrodynamic effects.

6.2 Design Framework for Underwater Adaptation

Adapting an HR manipulator for underwater applications can be challenging, especially if it must be carried by an underwater vehicle. This part of the work focuses on the design and optimisation of the robot to make it adaptable to such an application. Given the robotic system's current state, attaching it to an ROV would be challenging due to its weight and size. As quantified in Chapter 5, stiffness modulation through global pretension tends to demand higher baseline tendon forces, and higher baseline forces amplify tension drops due to friction and hysteresis in long routings. This motivates underwater adaptation strategies that reduce the tension required to achieve a target stiffness, for example, by reducing weight and adding buoyancy support. The underwater adaptation relies on two constraints already integrated in the design presented in Chapter 3. First, the tendon routing design fixes the minimum module diameter and the tendon pitch-circle geometry, which constrains how much the link cross-section can be reduced without redesigning the routing. Second, placing actuation off-board allows operation in harsh environments, but it also concentrates mass, volume, and power demand into an external actuation unit. Chapter 5 later shows that routing length and baseline tension directly influence tension transfer efficiency and tracking disturbance. In Chapter 5, routing losses were quantified through a linearised tension-transfer relationship $F_{delivered} \approx aF_t - b$. Using the required delivered tendon force estimated above, the corresponding global tension command follows $F_t \approx (F_{delivered} + b)/a$. This links load reduction through buoyancy directly to reduced tension demand and reduced friction losses during motion. Underwater deployment, therefore, becomes a system-sizing problem: reducing submerged apparent weight and drag reduces required tendon forces, thereby reducing actuation unit size and improving controllability. The actuation unit is significantly larger than a typical ROV,

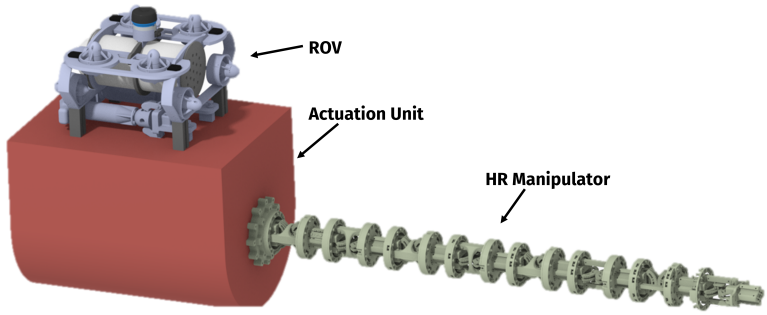


Figure 6.4 Concept of the underwater system

making the system challenging to carry. Buoyant elements could be added to support the large, heavy actuation unit, but this would further increase the overall system size. Therefore, size and weight reduction are still needed, since a smaller unit requires smaller buoyant elements or can be carried directly by the ROV without a buoyancy system. Figure 6.4 shows the concept of an underwater robotic system attached to a typical-sized ROV. There are two complementary strategies to reduce required tendon forces and, therefore, downsize the actuation unit. The first is to reduce the manipulator's submerged apparent weight by achieving near-neutral buoyancy at the modules, so that gravity does not dominate load cases at the proximal joints. The second is to reduce hydrodynamic resistance and mass through link optimisation, which lowers both drag forces during motion and static loads. Both strategies decrease the maximum joint required torque and reduce the baseline pretension required for stable tendon transmission.

6.2.1 Optimisation Process and Performance

The optimisation of the underwater links follows the same GP-based worst-case load identification framework introduced in Chapter 4, adapted here at the module level. This study is also presented in [168]. The goal is to reduce link mass while keeping the peak stress under all relevant load conditions below the material limit. Mass reduction is pursued not only to satisfy ROV payload limits, but also because a lighter structure reduces worst-case joint loads, lowers required tendon tensions, and directly reduces actuator size. The overall workflow is summarised in Figure 6.5. First, a Latin Hypercube Sampling (LHS) algorithm generates $m = 300$ random joint angle vectors for the $LORY - 8JP$ manipulator. For each sampled configuration q_i, the static model described earlier computes the corresponding base loads $\mathbf{X_i} = \{M_{x_i}, M_{y_i}, R_{x_i}, R_{y_i}, R_{z_i}\}$ producing an $m \times 5$ matrix of load cases for the considered link. These loads are then applied in a batch

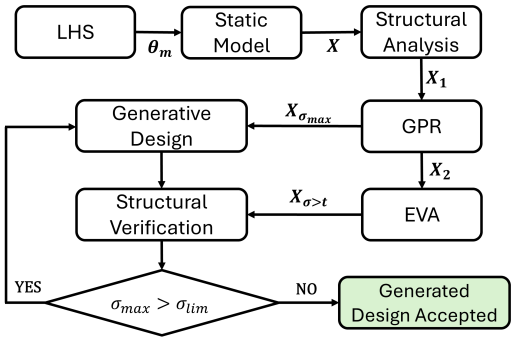


Figure 6.5 Optimisation Process

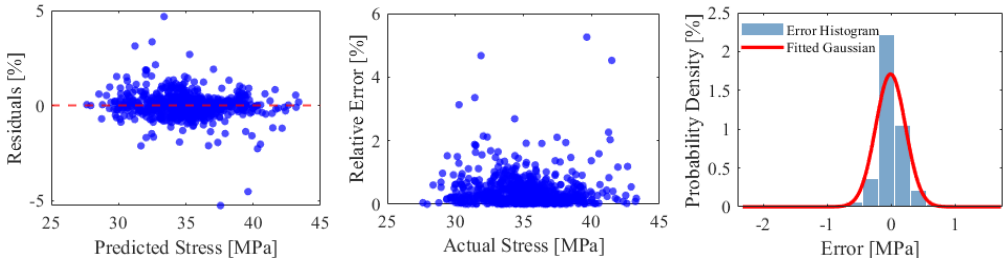
structural analysis in Ansys, as detailed in Chapter 4, which returns the associated peak Von Mises stresses σ_{VM_i} and forms the training dataset $\mathbf{X_1}$= $\{M_{x_i}, M_{y_i}, R_{x_i}, R_{y_i}, R_{z_i}, \sigma_i\}$. A GP regression model is then trained on this dataset, using the same modelling choices, preprocessing, and hyperparameter learning strategy described in Chapter 4. Once trained, the GP is queried on new load combinations generated by the static model to predict stresses over a much denser set of feasible scenarios. The BO-based acquisition step searches this space and identifies the load vector that maximises the predicted stress for the link, denoted $\mathbf{X}_{\boldsymbol{\sigma}_{\mathbf{max}}} = \{M_{x_{\sigma_{max}}}, M_{y_{\sigma_{max}}}, R_{x_{\sigma_{max}}}, R_{y_{\sigma_{max}}}, R_{z_{\sigma_{max}}}\}$. This worst-case load is then used as the primary design load for the generative design stage presented in in Section 6.2.2. After an optimised geometry is obtained, structural validation closes the loop. An Extreme Value Analysis (EVA) based load screening identifies the subset of load cases that produce stresses above a high threshold t, which represents a conservative bound for rare but critical events: $\mathbf{X}_{\boldsymbol{\sigma}>\mathbf{t}} = \{M_{\sigma>t}, M_{\sigma>t}, R_{\sigma>t}, R_{\sigma>t}, R_{\sigma>t}\}$.

These load cases are re-applied to the optimised design. If any of them raises the stress above the material limit, the generative design step is repeated with the offending load as the new design load. In the present case study, no load case in $\mathbf{X}_{\sigma>t}$ exceeded the material strength, so the process terminated after a single optimisation and validation cycle.

To ensure that the results of this optimisation process are reliable, the model's accuracy can be assessed from the performance parameters in table 6.1. The table reports the RMSE, the MAE, and the R^2 parameter for each link of the manipulator, as defined in Chapter 4. As shown in the table, the *RMSE* is very low, indicating high predictive accuracy. The *MAE* is also low, indicating a low deviation from the true values. Finally, R^2 values, which measure the proportion of variance in the actual values, are close to 1, indicating a good fit.

Link	$RMSE[MPa]$	$MAE[MPa]$	R^2
1	0.25	0.27	0.99
2	0.21	0.32	0.99
3	0.23	0.37	0.99
4	0.16	0.24	0.99
5	0.10	0.21	0.99
6	0.02	0.02	0.99
7	0.01	0.07	0.99
8	0.01	0.03	0.99

Table 6.1 Performance parameters of the GP model for each robot link



(a) Residuals (b) Relative Errors (c) Error Distribution

Figure 6.6 Performance Parameters Plots of the GP model for the first link

Furthermore, figure 6.6 shows the model prediction performance plots regarding the first link, including the residuals, the relative errors plot, and the errors distribution plot for the first link of the manipulator. Figure 6.6a shows how, apart from a few outliers, most residuals are centred around zero, meaning the GP model has a low bias, and the predictions are generally close to the actual values. Also, the residuals range approximately from -5% to 5% with good randomness and no clear patterns, which means the errors are moderate and the model is well-calibrated. The relative errors shown in figure 6.6b are also low, with the vast majority being lower than 2%. Finally, figure 6.6c shows the distribution of errors with a fitted Gaussian distribution for comparison. The distribution is symmetric, and the highest frequency of errors is clustered around zero, near the peak of the Gaussian fit. This means the GP model is unbiased, meaning it does not, on average, underestimate or overestimate the stress values.

6.2.2 Optimal Streamlined Geometry with Generative Design

GD is a powerful method for achieving structural efficiency by optimising material distribution based on load-path requirements [169].

This optimisation step targets minimum mass while preserving structural safety under the selected design load. Formally, the problem is written as:

$$\min_{x}[m(x) = \rho\, V(x)] \tag{6.1}$$

$$\sigma_{\mathrm{VM}}(x) \leq \frac{\sigma_{\mathrm{yield}}}{SF} \tag{6.2}$$

where x represents the geometric design variables handled by the GD solver, $m(x)$ is the resulting mass, ρ is the material density, and $V(x)$ is the solid volume of the generated geometry. The stress constraint enforces that the maximum Von Mises stress remains below the allowable strength, defined through the safety factor SF (set to 1.3).

This formulation ensures the solver converges on a geometry that withstands the worst-case load while removing non-structural mass to reduce buoyancy effects.

While topology optimisation focuses on deriving a single solution by addressing functional objectives, constraints, and loads step-by-step [170], GD explores numerous solutions simultaneously, aiming to identify the best options that meet functional requirements. GD aims to determine the optimal distribution of material within a given design space, targeting minimal weight while maintaining structural integrity under multiple load cases [171]. The GD optimisation was performed using Creo Parametric software from PTC, and the steps needed are outlined below. First, the Preserved Geometry (PG) and the Excluded Geometry (EG) need to be specified. PG is part of the analysed geometry, but its shape remains unchanged. EG is the part of the geometry that is not part of the analysis. Then loads and constraints need to be applied to the PG. In this case, the load case $\mathbf{X}_{\sigma_{\mathbf{max}}}$, derived from the GP prediction, is applied to the PG. When loads need to be applied to the EG, a contact between the EG and the PG is first established to account for the constraints applied to the EG in the structural analysis. After that, the design criteria need to be specified, which are of two types: stiffness maximisation and mass minimisation. In this case study, mass minimisation was chosen. Then, the design constraints for the geometry generation need to be specified. The design constraints are: the build direction, the parting line, the linear extrude, the build symmetry, the material spreading, and the minimum crease radius. For preliminary shape generation, no constraints were imposed on the design criteria, allowing the generative design algorithm to explore the entire available space without limitations. A safety factor of 1.3 was used for the structural optimisation. The generated design is shown in figure 6.7 (left), where the coordinate system is represented in the local frame.

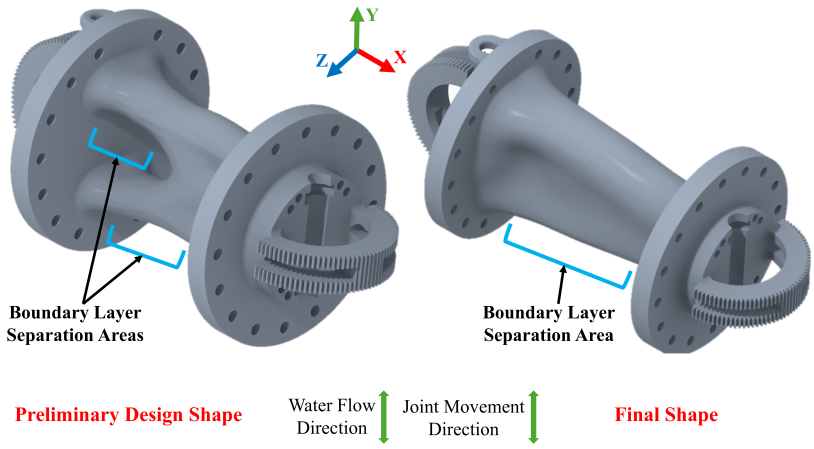


Figure 6.7 Shape of the first joint before and after design constraints. Left: the preliminary design. Right: the final design.

As the joint rotates around the local Z axis, it is worth noting that the link geometry has a higher moment of inertia about the Z axis than about the Y axis. This trend is also seen among all the other joints.

This advantage was exploited to produce a more streamlined shape, thereby reducing the drag coefficient. A continuous shape geometry is preferred over a discontinuous one to minimise water resistance and drag as it allows for smoother flow around the object, reducing turbulence and pressure drag. When a body moves through water, the surrounding fluid exerts forces that depend on the shape and surface continuity of the object [172]. A continuous geometry guarantees that the boundary layer remains attached to the surface for a longer distance, delaying separation and minimising wake formation. In contrast, a discontinuous shape, characterised by abrupt changes, sharp edges, or segmented structures, disrupts the flow, leading to early boundary-layer separation and increased pressure drag due to the formation of vortices and turbulent wake regions. By optimising the shape to maintain a gradual pressure gradient along the surface, a continuous design significantly reduces drag forces, thereby lowering the power required for movement in water. For this reason, some constraints are added to the design criteria in the generative design tool to further adapt the geometry to underwater movement.

A double symmetry constraint is applied by forcing the geometry to have symmetry both in the $X-Y$ and $X-Z$ planes. The symmetry in the $X-Y$ plane is needed in order to have a pressure difference close to zero between the two sides of the geometry. The symmetry in the $X-Z$ plane is needed to account for the fact that the link can move up or down; this way, the drag coefficient difference between the upper and lower sides

Link	1	2	3	4	5	6	7	8
m_1 **[kg]**	0.710	0.631	0.559	0.456	0.408	0.388	0.381	0.278
m_2 **[kg]**	0.526	0.487	0.452	0.412	0.391	0.371	0.369	0.265
Δm **[%]**	25.9	22.8	19.1	9.86	4.17	4.38	3.15	5.04

Table 6.2 Mass reduction of the robot links after optimisation.

of the geometry is nearly zero. Another constraint applied to the design criteria is the maximum material spread, which is kept to a minimum. The reason for this constraint is to reduce boundary layer separations in the geometry, which, as already mentioned, heavily depends on the number of discontinuities in the shape of the object, as illustrated in figure 6.7(left). The resulting geometry of the first link is shown in figure 6.7(right).

While full hydrodynamic verification is outside the scope of this design study, the theoretical aerodynamic improvement can be estimated by comparing standard drag coefficients[1]. The original link design approximates a cylindrical body ($C_d \approx 0.5-1$), whereas the generative design approximates a streamlined profile ($C_d \approx 0.05-0.15$). Even assuming a conservative reduction in C_d of 50%, the hydrodynamic load on the manipulator would be halved.

The optimised design achieved a significant weight reduction compared to the parametrically optimised version, assuming a hollow cylinder. The mass reduction of each link, compared to the previous version of the robot, is presented in table 6.2, where m_1 is the mass of the first version link, and m_2 is the mass of the link generated with GD. Mass reduction was achieved while preserving external diameter constraints and maintaining the same functional interfaces required for tendon routing and joint assembly.

After the optimal geometry is generated, the next step is to validate the resulting link geometry under new load conditions. Using the p load cases generated with the GP model, an EVA [173] algorithm was used to determine the stress threshold corresponding to a high-confidence limit for extreme but rare load scenarios. Regarding the dataset analysed with the GP model, stresses above the threshold are considered in the structural analysis of the newly generated geometry, providing an additional layer of confidence in the system's structural safety. EVA uses a Generalised Extreme Value (GEV) distribution, defined by its cumulative distribution function [174]:

$$P(\sigma \leq u) = \exp\left(-\left(1+\xi\frac{\sigma-\mu}{\sigma}\right)^{-1/\xi}\right)$$

[1] https://volupe.com/support//

where μ is the location parameter, representing the centre of the distribution of extreme values, σ is the scale parameter, controlling the spread of the extreme values, and ξ is the shape parameter, which defines the tail behaviour of the distribution. In this case, σ represents the p predicted stress values generated by the GP model, and the parameters μ, σ, and ξ are estimated from the data. The estimated parameters then allow for modelling the distribution of extreme stresses and for identifying critical thresholds. For a set of predicted stresses $\sigma_{pred}(X_2)$, the return level σ_{return} is the stress level expected to be exceeded with a specified probability over a given set of configurations. For a given probability level p, the return level is computed as:

$$\sigma_{return} = \mu + \frac{\sigma}{\xi}\left((-\ln(1-p))^{-\xi} - 1\right)$$

where p is the probability level (e.g., 0.99 for a 99% return level), indicating the likelihood of observing a stress value above σ_{return} within the analysed configurations. Among the $\mathbf{X_2}$ load combinations generated by the GP model, there are l_i load cases that are above σ_{return}, where i is the link number. A structural analysis was performed on all the l_i load cases on the generated geometry for each link. In this case study, all the robot links withstood the load cases above the corresponding thresholds. However, if one of the links failed under one of the load cases, that load case would have been considered for another generative design optimisation, and the validation process would have been repeated.

The resulting optimised prototype has a total mass $m_{tot} = 3.8\ kg$, a length $L = 1.6\ m$, and a payload $P = 1\ kg$. This value represents a payload-based reference value under gravity-compensated conditions, since it accounts only for the payload contribution. Any residual negative buoyancy of the modules, hydrodynamic loads, or non-buoyant tooling would add an additional torque term, thereby increasing the required tendon force above 375 N. The virtual prototype of the optimised robot is shown in figure 6.8. With a payload P, the required torque for the first joint is $M = 16\ Nm$, resulting in a tendon tension $F_u^+ = 375\ N$. Intrinsically buoyant components allow neglecting the manipulator's weight, as it would not affect the actuation forces, and only the payload can be considered.

Considering only the robot weight, the existing prototype needed a minimum cable force of 1180 N at the first joint, which is much higher than F_u^+, and the actuation unit has been designed accordingly. On the other hand, F_u^+ can be transmitted by a much smaller actuation unit than the one used in the existing prototype. Although the manipulator's weight is not important for actuation, optimisation is still needed to increase the system's payload-to-size ratio. If the robot is not inherently buoyant, the optimisation method

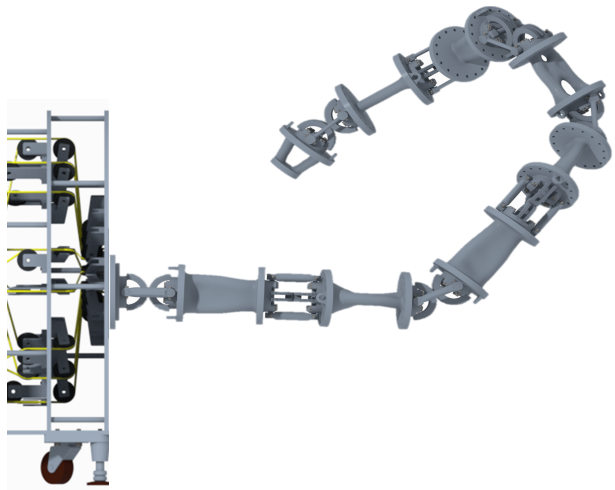


Figure 6.8 Virtual prototype of the optimised manipulator

presented is even more important, as lower module weight results in smaller BEs with lower weight. This concept is detailed in the next section.

6.2.3 3D Printing, Buoyancy Design and Testing

As mentioned, the optimisation process depends on the buoyancy of the system, which is directly related to the average density of each module. The density of the 3D-printed elements often is not the density of the filament or resin from which it is printed. Generally, SLA printed parts have a higher quality compared to FDM printed ones, as they have fewer void spaces in the material, and consequently, the density of an SLA printed part is usually very close to the theoretical density provided by the manufacturer [175]. The build volume is the most important discriminator for the printer choice in this case study. Considering that the maximum dimension of the largest link in the prototype is approximately 220 *mm*, the only suitable printing technology for the links is Fused Deposition Modelling (FDM). The other components of the robot were printed using SLA technology, as it offers better printing quality, and the density of the printed parts is closer to the actual density.

The material choice is primarily based on strength, density, and water absorption, in that order. Having looked into different materials from different manufacturers[2][3], data shows that the best-performing materials are FT2000 from Formlabs[4] and Onyx from

[2]https://bambulab.com/

[3]https://ultimaker.com/3d-printers/s-series/ultimaker-s5/

[4]https://formlabs.com/it/3d-printers/catalog/

	SLA Parts	FDM Parts
$\rho_{th}[kg/m^3]$	1050	1200
$\rho_r[kg/m^3]$	1030	733

Table 6.3 Theoretical and real densities of the printed parts

Markforged Mark 2[5]. The water absorption rate for Onyx is not easily obtainable, as different manufacturers provide varying numbers, and the printer manufacturer does not provide any. However, the tensile strength of Onyx is comparable to that of 3D-printed Nylon, and the flexural strength is one of the highest, which is very important for the robot links. Therefore, Onyx is chosen for the links, while FT200 is preferable for the other parts since they are smaller. PETG from BambuLab is also good, but since SLA is preferable, FT2000 is the better choice.

Considering the uncertainties regarding the density of the printed parts, the best approach is to first print the part, with the preferred printing characteristics, weigh it, and derive its real density ρ_r, calculating the ratio between the measured module weight and the volume of the module provided by the CAD model. After having printed and weighed the parts, and having compared them to the virtual prototypes, the densities of the SLA and FDM printed parts are as shown in table 6.3, where ρ_{th} is the theoretical density provided by the manufacturer, and ρ_r is the real measured density. As shown in table 6.3, SLA printed parts have a density that is very close to the theoretical one, while FDM printed parts present a significant density difference. Furthermore, a water-absorption test was performed by submerging one of the modules in seawater for 24 hours. In 3D-printed Nylon parts, most water absorption occurs rapidly within the first day, making the first day a valid time frame for evaluating the initial effects of moisture absorption before more severe degradation sets in. As reported in [176], 3D-printed Nylon can absorb approximately 10% of its weight in water within the first 24 hours at 21°C, and this absorption results in an initial 4% decrease in yield strength after 24 hours. However, prolonged exposure leads to significant degradation, with a 60% reduction in flexural modulus after 7 days. Onyx parts are made of Nylon and reinforced by carbon fibre. Since Onyx is Nylon-based and produced by FDM, the absorbed fraction depends on both the polymer composition and the internal porosity introduced by print settings, so the 24-hour mass gain should be interpreted as a process-dependent design input rather than a material constant. Hence, the underwater behaviour is considered similar, although the carbon fibres may improve performance, as confirmed by the fact that after

[5]https://markforged.com/materials/plastics/onyx

24 hours of submersion, the Onyx parts only gained 3.4% of their weight. However, a longer submersion time could lead to a non-negligible weight gain and degradation of mechanical properties.

After having assembled the Onyx 3D-printed parts of the first module, it was weighed, and the resulting density was $\rho_a = 1010\ kg/m^3$, slightly lower than the seawater density $\rho_w = 1020\ kg/m^3$. This difference can be compensated by adding a thin steel ring that wraps around the link or an SLA-printed part that has a high enough density. The optimised 3D-printed parts were assembled into a two-module manipulator and tested for buoyancy, as shown in figure 6.9. The test was performed using seawater from the

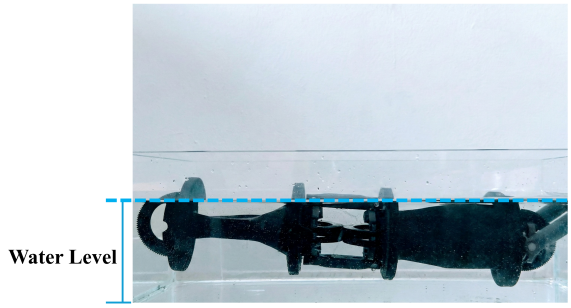
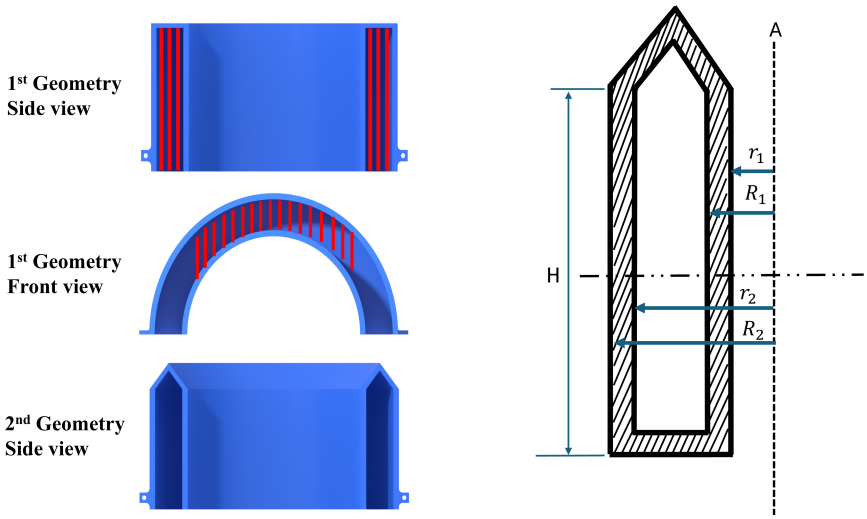


Figure 6.9 Simple buoyancy test on a two-module prototype

North Sea, with a density $\rho_w = 1020\ kg/m^3$, slightly lower than the world average. The first joint was kept fixed to the outer wall of the bucket to simulate a fixed platform just below the water surface. As shown in figure 6.9, the two modules are almost completely submerged, meaning it is sufficient to add a small counterweight to achieve neutral buoyancy. It is important to note that, as shown in the picture, the left module appears slightly less buoyant than the right one. This occurs because the link's buoyancy was computed by taking into account the weights of both the link itself and the subsequent joint. Since there is no additional joint on the left side, there is no weight to counteract the positive buoyancy, resulting in the apparent imbalance. In this case, it was decided to leave the robot's average density slightly below water density to provide a slight buoyancy margin for possible non-buoyant end-effectors.

As mentioned before, if the average density of the ith module is greater than seawater density, which can easily be the case if further assembling components are added or the parts have higher density, an external BE has to be designed to achieve neutral buoyancy.

The BEs must be implemented for each module to obtain neutral buoyancy so the whole system stays in equilibrium when in water. The simplest geometry for a BE to be implemented into each link is a hollow cylinder. However, a purely cylindrical shape



(a) Possible geometries for the BE

(b) 2nd geometry cross-section

Figure 6.10 Comparison between the two possible BE geometries (left), and the BE base geometry (right)

is not well suited to be 3D printed, no matter the printing technology used, as the part would require internal support in both printing directions, which would increase the mass, and it would be impossible to account for it in the equilibrium equations. This is illustrated in figure 6.10a, which shows the cylindrical shape in two different view sections. The presented views represent the two possible print directions for the purely cylindrical-shaped geometry (1st geometry). As shown in the figure, in both printing directions, the first geometry needs supports to be printed. In this case study, the BE geometry is considered to be a hollow cylinder with a cone attached to the top, generated by performing a revolution on a triangle, as forming the 2nd geometry of figure 6.10a. As shown, no supports are needed for the second type of geometry. This is because the side of the triangle is at 50°, allowing printing without needing supports. The material chosen for the BE is ABS, given its low density, which is desirable for having a smaller size. Figure 6.10b shows the cross-section of the geometry, where the crossed-out area indicates presence of material, and, by performing a revolution around the A axis, generates the mentioned shape.

Considering the equilibrium state of each module, the force due to the module's weight must be equal to the hydrostatic force generated by the BE in the opposite direction of gravity. Since it is impossible to fix the BE at the centre of gravity of each module, they will be fixed at the links, as shown in figure 6.11. Depending on the mass of each module

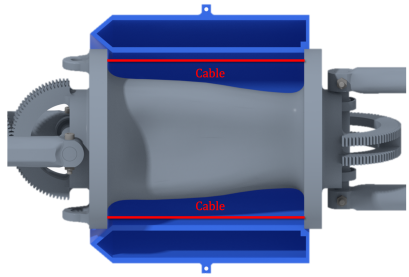


Figure 6.11 Implementation of the BE in the modules

and the length of each link, the outer radius R_2 of the cylinder is obtained by solving the equilibrium equation for each module. With reference to figure 6.10b, the height H of the BE depends on the link length, while the radius $r_1 = 46\ mm$ is considered slightly above the cable passage radius, and $R_1 = r_1 + t$, $r_2 = R_2 - t$, where $t = 3\ mm$.

$$\rho_w \cdot g \cdot V_{\text{tot-BE}} = g \cdot M_{\text{module}} + \rho_{\text{ABS}} \cdot g \cdot V_{\text{non-void-space-BE}} \tag{6.3}$$

Where ρ_w is the seawater density considering the average in the North Sea, g is the gravitational constant, $V_{\text{tot-BE}}$ is the total Volume of the BE, M_{module} is the mass of the ith module, ρ_{ABS} is the ABS density, and $V_{\text{non-void-space-BE}}$ is the volume of the non-void space of the BE. The left side of the equation represents the buoyant force, while the right side represents the sum of the weight forces of the ith module and i^{th} BE. With reference to figure 6.10b, considering $R_1 = r_1 + t$, V_{tot} and $V_{\text{non-void-space}}$ can be written as:

$$\begin{aligned} V_{\text{tot}} &= \frac{\pi}{4}\tan^2(50^\circ)\left(\frac{4}{3}R_2^3 - R_2^2 r_1 - R_2 r_1^2 - \frac{1}{3}r_1^3\right) \quad + \pi H\left(R_2^2 - r_1^2\right) \\ V_{\text{non-void-space}} &= \pi H\left(R_2^2 - r_1^2\right) - \pi(H-t)(R_2^2 - r_1^2) \\ &+ \frac{\pi}{4}\tan^2(50^\circ)\left(\frac{4}{3}R_2^3 - R_2^2 r_1 - R_2 r_1^2 - \frac{1}{3}r_1^3\right) \\ &- \frac{\pi}{4}\tan^2(50^\circ)\left(\frac{4}{3}r_2^3 - r_2^2 R_1 - r_2 R_1^2 - \frac{1}{3}R_1^3\right) \end{aligned}$$

Rearranging to obtain a third-degree equation, the following can be written:

$$AR_2^3 + BR_2^2 + CR_2 + D = 0 \tag{6.4}$$

Where:

$$A = \rho_w \frac{\pi}{3}\tan^2(\alpha) - \rho_{\text{abs}} \frac{\pi}{3}\tan^2(\alpha) + \rho_{\text{abs}} \frac{\pi}{3}\tan^2(\alpha),$$

$$\begin{aligned} B = {} & \rho_w \pi H - \rho_w \frac{\pi}{4}\tan^2(\alpha) r_1 - \rho_{\text{abs}} \pi H + \rho_{\text{abs}} \frac{\pi}{4}\tan^2(\alpha) r_1 + \rho_{\text{abs}} \pi H \\ & + \rho_{\text{abs}} \pi t - 2\rho_{\text{abs}} \frac{\pi}{3}\tan^2(\alpha) t - \rho_{\text{abs}} \frac{\pi}{3}\tan^2(\alpha) t - \rho_{\text{abs}} \frac{\pi}{4}\tan^2(\alpha) R_1, \end{aligned}$$

$$\begin{aligned} C = {} & -\rho_w \frac{\pi}{4}\tan^2(\alpha) r_1^2 + \rho_{\text{abs}} \frac{\pi}{4}\tan^2(\alpha) r_1 - 2\rho_{\text{abs}} t \pi H - 2\rho_{\text{abs}} \pi t^2 \\ & + \rho_{\text{abs}} \frac{\pi}{3}\tan^2(\alpha) t^2 + 2\rho_{\text{abs}} \frac{\pi}{3}\tan^2(\alpha) t^2 + \rho_{\text{abs}} \frac{\pi}{4}\tan^2(\alpha) R_1 t - \rho_{\text{abs}} \frac{\pi}{4}\tan^2(\alpha) R_1^2, \end{aligned}$$

$$\begin{aligned} D = {} & -\rho_w \pi H r_1^2 - \rho_w \frac{\pi}{12}\tan^2(\alpha) r_1^3 + \rho_{\text{abs}} \pi H r_1^2 + \rho_{\text{abs}} \pi H t^2 + \rho_{\text{abs}} \pi t^3 - \rho_{\text{abs}} \pi H R_1^2 \\ & + \rho_{\text{abs}} \pi t R_1^2 + \rho_{\text{abs}} \frac{\pi}{12}\tan^2(\alpha) r_1^3 - \rho_{\text{abs}} \frac{\pi}{4}\tan^2(\alpha) r_1^2 R_1 - \rho_{\text{abs}} \frac{\pi}{12}\tan^2(\alpha) R_1^3 \\ & - \rho_{\text{abs}} \frac{\pi}{3}\tan^2(\alpha) t^3 - \rho_{\text{abs}} \frac{\pi}{4}\tan^2(\alpha) R_1 t^2 + \rho_{\text{abs}} \frac{\pi}{4}\tan^2(\alpha) t R_1^2 - M_{\text{module}} \end{aligned}$$

Equation 6.4 is only valid if the average density of the ith module is higher than the water density.

An important constraint considered is the Range Of Motion (ROM) of the joints after the BE implementation. The ROM of each joint depends on the outer radius of the BE, which depends on the weight of the module. Considering an ABS 3d-printed BE, the limit mass of the first module allowing a ROM of 45° is 500 g. Given the robot's statics, the modules have decreasing weights toward the tip, so the masses never exceed 500 g, and all the joints allow a ROM of 45° even if all the modules achieved the mass of the first module.

The 3D printing material that can be selected for this purpose depends on its density and printing technology, as parts with lower density require a lower buoyant volume. The material selected to test the theoretical derivation is ABS since it has the lowest density among the available materials for 3D printing, resulting in a lighter and smaller BE. To obtain the final BE a test must first be performed on a test part, measuring its weight and deriving its density, as well as testing its water absorption, as it can affect the design. A cube of 3d printed ABS was used for testing. It was weighed before and after having left it in seawater for 24 hours, and the mass change was negligible, around 1.3%, corresponding to 2 g. Furthermore, the weight of the printed BE was 137 g, while the virtual part showed a weight of 200 g, resulting in a weight loss of 31.5% after printing. By considering the real weight and the volume of the BE, the real density was measured,

obtaining $\rho_a = 690\ kg/m^3$. Considering these results, the BE was designed considering the ρ_a of the printed part, and a mass of 600 g was used as module mass, resulting in an outer radius $R_2 = 69.2\ mm$. The BE was printed and tested with a 600 g weight, and the result was satisfying, as the system stayed just below the water surface, and when a 10 g non-buoyant mass was added, it began to sink very slowly. This means that the design method for the BE and formulation is correct.

Overall, this Chapter demonstrated how the validated TD manipulator can be adapted for field deployment by combining data-driven worst-case stress prediction (Chapter 4) with mass and buoyancy design.

CHAPTER 7

TOWARDS THE METALLIC PROTOTYPE: TORSIONAL STIFFENER DESIGN

Late-stage functional testing on LORY-5JP revealed an overlooked limitation: under high torsional loading, particularly in configurations where the entire manipulator rotated laterally from joint 1, the joint showed significant torsional compliance, with observable deflection at the end-effector.

These findings prompted a re-evaluation in the context of the upcoming metallic prototype, which requires higher stiffness and accuracy. Specifically, the first joint must withstand the largest cumulative torsional loads, and its deflection becomes a bottleneck for precision tasks.

This chapter addresses that need by proposing and evaluating lightweight stiffener designs for the first joint of the future metallic version of the robot, as detailed in [177]. The study explores two constrained geometries compatible with the existing actuation and routing scheme, providing quantitative guidance for increasing torsional stiffness while maintaining manufacturability and mass efficiency.

7.1 PROBLEM DESCRIPTION

The maximum torsional load applied on the origin O_2 along the x_2-axis of the first joint is $M_t = 100$ Nm, representing the maximum cantilever extension, and is obtained when

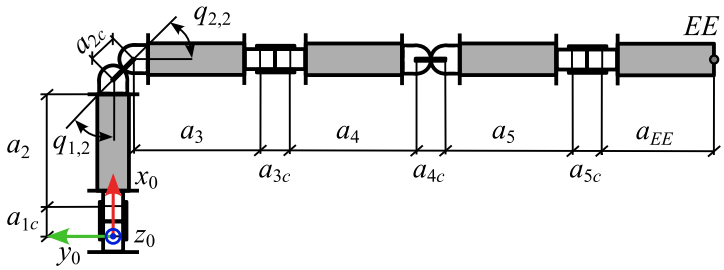


Figure 7.1 Robot configuration corresponding to maximum torsional load on the first joint, M_t.

Parameter	Symbol	Value	Unit
Density	ρ	2810	kg/m^3
Young Modulus	E	71.7	GPa
Poisson Ratio	ν	0.33	

Table 7.1 Physical and mechanical properties of A7075 T6 (Ergal).

the values of $q_{i,j}$ are zeros for all j except for $j = 2$, as shown in Fig. 7.1:

$$q_{1,2} = -\frac{\pi}{4}\text{rad},$$
$$q_{2,2} = -\frac{\pi}{4}\text{rad}.$$

The resulting torsional deformation of the first joint, as evaluated through finite element analysis, induces an error in the end-effector position of the robot. The structural static analyses performed in this work are executed using PTC Creo® 9.0 and are based on the following assumptions and parameters:

- the joint geometry is simplified considering the bodies most sensitive to M_t, i.e. the intermediate links connected by two shafts;
- all the contact interfaces are assumed to be bonded;
- p-elements polynomial order from minimum 3 to maximum 9;
- mesh element type tetrahedron;
- mesh element edge size 5mm;
- Multi-Pass Adaptive method with percent convergence 10%.

All the mechanical components considered in this study are made of aluminium alloy

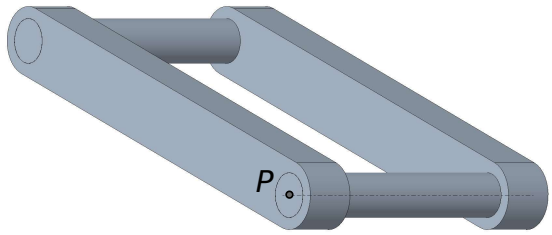


Figure 7.2 3D CAD model of the simplified joint highlighting the point P.

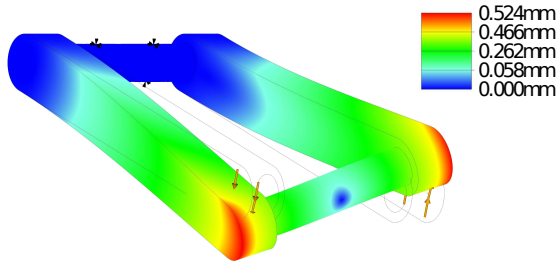


Figure 7.3 Deformed model of the simplified joint showing the constraint on the inner shaft and the torsional load on the outer shaft. A scale factor of 10 is applied to better visualise the deformation.

A7075 T6, also known as Ergal. This material has been chosen because it performs well in terms of mechanical stiffness to weight ratio:

$$\frac{E}{\rho} = 26 \frac{\text{MPa m}^3}{\text{kg}},$$

where E is the Young modulus and ρ is the density. Such value is comparable to that of titanium. The 3D CAD model of the simplified joint, whose mass is $m_0 = 0.368\text{kg}$, is reported in Fig. 7.2. A first structural static analysis has been performed on the simplified joint where the load M_t is applied on the contact surfaces between the outer shaft and the intermediate links, having constrained the inner shaft. Figure 7.3 reports the results of the analysis. The displacement of the point P, which is one of the end points of the axis of the outer shaft, is $u_{P_0} = 0.481\text{mm}$. The corresponding torsional deformation results in a rotation of

$$\theta_{P_0} = \arcsin\left(\frac{2u_{P_0}}{l_s}\right) = 10.7 \times 10^{-3}\text{rad},$$

where $l_s = 90\text{mm}$ is the length of the outer shaft. Considering the joints configuration of the robotic system for which the torsional load on the first joint is M_t, the maximum displacement of the position of the end-effector induced by θ_{P_0} is $u_{EE_0} = 20.9\text{mm}$. To

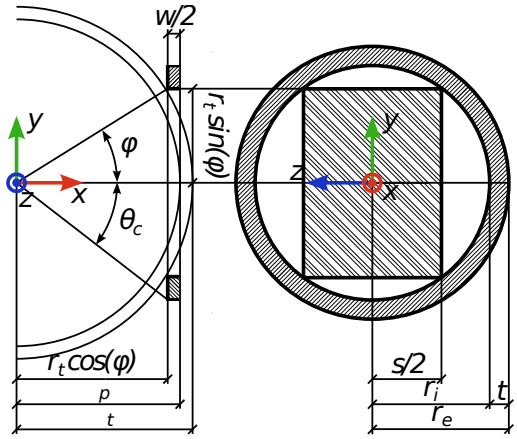


Figure 7.4 Geometrical parameters for a stiffener element surrounding the gears.

increase the joint's torsional stiffness without altering the components' original geometry, a stiffener element must be added. Such an element must satisfy the constraints of the geometry of the whole joint, including the gears, the flanges, and the cables. Figures 7.4 and 7.5 report the geometrical parameters required to describe such constraints. In the following, two different designs that satisfy such constraints are investigated.

7.1.1 Tube-shaped geometry

Assuming a ring section, with width and thickness w and t, respectively, drawn in the space between the two gears of the joint as shown in Fig. 7.4, the following relations are defined:

$$\begin{aligned}
\varphi &= \arccos\left(\frac{2r_p - w}{2r_t}\right), \\
r_i &= \sqrt{\left(\frac{s}{2}\right)^2 + \left[r_t \sin(\varphi)\right]^2}, \\
t &= r_e - r_i = \left[\frac{d\cos(q_m) - d_c}{2}\right] - \sqrt{\left(\frac{s}{2}\right)^2 + r_t^2\left[1 - \left(\frac{2r_p - w}{2r_t}\right)^2\right]},
\end{aligned} \tag{7.1}$$

where r_t and r_p are the tip and the pitch radii of the gear, respectively, s is the gear depth, d_c is the cable diameter, and r_e is the semi-minor axis of the ellipse passing through the positions of the cables when $q_1 = q_m$. Considering a minimum thickness t_{min} and a minimum width w_{min}, w lies in the range $[w_{min}, w_{max}]$ where $w_{max} = w(t_{min})$. The values

Parameter	Value	Unit
d	130	mm
r_t	76.5	mm
r_p	75	mm
s	10	mm
d_c	3	mm
r_e	44.5	mm
t_{min}	1	mm
w_{min}	1	mm
w_{max}	23.7	mm

Table 7.2 Geometric parameters describing the tube-shaped geometry constraints.

of the geometric parameters required to describe the constraints that the tube-shaped geometry has to satisfy are listed in Table 7.2. Furthermore, assuming a support similar in shape to a cylindrical tube with the ring cross-section described above, its faces must be cut to avoid contact between the support and the joint flanges. As shown in Fig. 7.4, the cut angle θ_c is subject to the following constraint:

$$\theta_c = \operatorname{atan2}\left(r_e, r_p - \frac{w}{2}\right) < q_m.$$

Given the limits of w, it is trivial to prove that such a condition is always respected.

7.1.2 Rectangular-shaped geometry

Assuming two equal rectangular sections, with base and height b and h, respectively, drawn in the inner spaces of both the gears of the joint as shown in Fig. 7.5, the following relation is defined:

$$h = 2\sqrt{r_2^2 - (r_1 + b)^2}, \tag{7.2}$$

where r_2 is the inner radius of the gear and r_1 is the radius of the circle tangent to the mounting support placed inside the gear. Assuming a minimum height h_{min}, h lies in the range $[h_{min}, h_{max}]$, with

$$h_{max} = 2\sqrt{r_e^2 - \left(\frac{l_s - 2d_i}{2}\right)^2},$$

where d_i is the depth of the intermediate link. The base b belongs in $[b_{min}, b_{max}]$, with

$$b_{min} = b(h_{max}),$$
$$b_{max} = b(h_{min}).$$

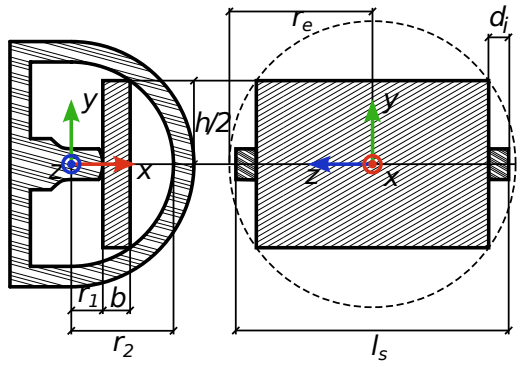


Figure 7.5 Geometrical parameters for a stiffener element mounted in the inner space of the gears.

Parameter	Value	Unit
r_1	42	mm
r_2	60	mm
d_i	15	mm
h_{min}	1	mm
h_{max}	65.7	mm
b_{min}	8.2	mm
b_{max}	17.998	mm

Table 7.3 Geometric parameters describing the rectangular-shaped geometry constraints.

The values of the geometric parameters required to describe the constraints that the rectangular-shaped geometry have to satisfy are listed in Table 7.3.

7.2 Proposed Solutions

The displacement u_{P_0} can be reduced by increasing the torsional stiffness of the joint adding a stiffener that connects the two intermediate links. To compare different stiffener designs, the following performance indicators are evaluated for a given i^{th} solution:

- the efficacy ε_i is calculated as follows

$$\varepsilon_i = 100\frac{(u_{P_0} - u_{P_i})}{(u_{P_0})},$$

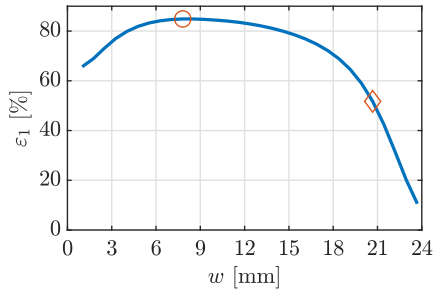


Figure 7.6 Sensitivity analysis for solution 1 in terms of ε. The orange circle highlights the values associated with maximum efficacy.

where u_{P_i} is the displacement of the point P with the stiffener, defined as the percentage reduction of the displacement with respect to the joint without the stiffener;

- the efficiency η_i is calculated as follows

$$\eta_i = \frac{(u_{P_0} - u_{P_i})}{(m_i - m_0)},$$

where m_i is the mass of the joint with the stiffener.

According to the geometrical constraints, assumptions, and parameters introduced in Section 7.1, two different solutions have been designed and analysed.

7.2.1 Solution 1: Tube-Shaped Stiffener

The first proposed solution is a tube-shaped stiffener surrounding the gears. This element is obtained from a cylindrical tube with length $2r_p$, external radius r_e, and thickness t, whose faces are cut each by two planes tilted of the angle θ_c. In addition, two portions of material with a rectangular cross-section in the x-z plane are removed to avoid interference between the stiffener element and the gears, maintaining a width of w according to (7.1). A sensitivity analysis has been performed varying the parameter w within the range $[w_{min}, w_{max}]$ with 30 steps. The corresponding results in terms of performance indicators are reported in Fig. 7.6 and 7.7. Two structural static analyses have been performed with the designs corresponding to the parameters that maximise ε_1 and η_1. The two designs are depicted in Fig. 7.8 and 7.9. The corresponding structural static analyses are shown in Fig. 7.10 and 7.11.

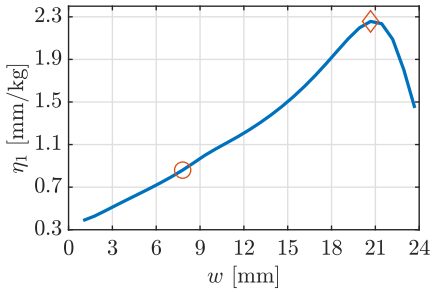


Figure 7.7 Sensitivity analysis for solution 1 in terms of ε. The orange diamond highlights the values associated with maximum efficiency.

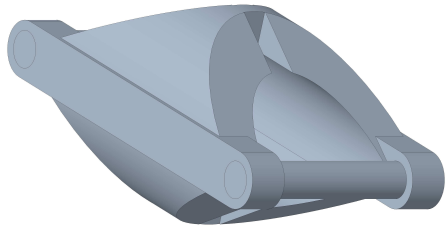


Figure 7.8 Design for solution 1 that maximises ε_1.

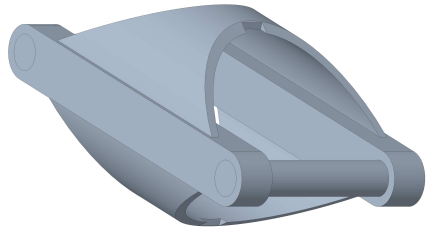


Figure 7.9 Design for solution 1 that maximises η_1.

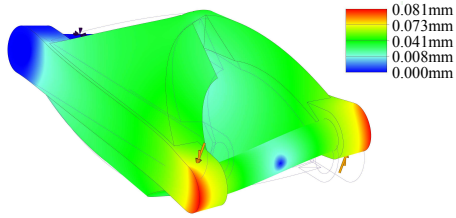


Figure 7.10 Deformed model of the simplified joint with the stiffener solution 1 that maximises ε. A scale factor of 10 is applied to better visualise the deformation.

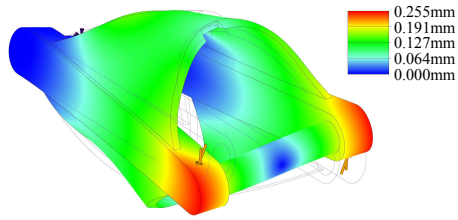


Figure 7.11 Deformed model of the simplified joint with the stiffener solution 1 that maximises η. A scale factor of 10 is applied to better visualise the deformation.

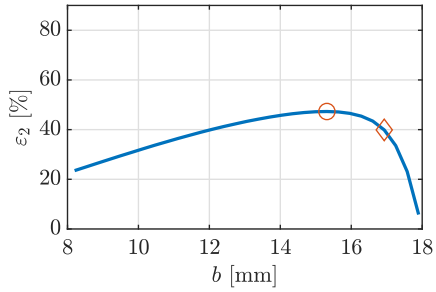


Figure 7.12 Sensitivity analysis for solution 2 in terms of ε. The orange circle highlights the values associated with maximum efficacy.

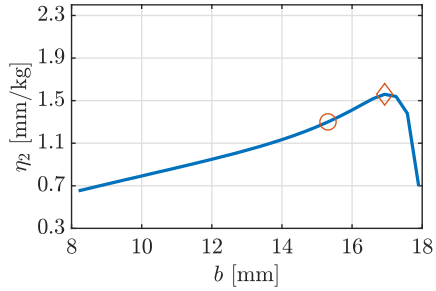


Figure 7.13 Sensitivity analysis for solution 2 in terms of η. The orange diamond highlights the values associated with maximum efficiency.

7.2.2 Solution 2: Rectangular-Shaped Stiffener

The second proposed solution comprises a pair of rectangular-shaped stiffeners passing through the gears. Both elements have a rectangular cross-section with base b and height h, which are related by (7.2). A sensitivity analysis has been performed varying the parameter b within the range $[b_{min}, b_{max}]$ with 30 steps. The corresponding results in terms of performance indicators are reported in Fig. 7.12 and 7.13. Two structural static analyses have been performed with the designs corresponding to the parameters

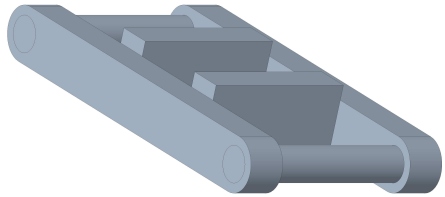


Figure 7.14 Design for solution 2 that maximises ε_2.

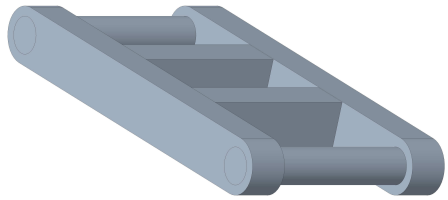


Figure 7.15 Design for solution 2 that maximises η_2.

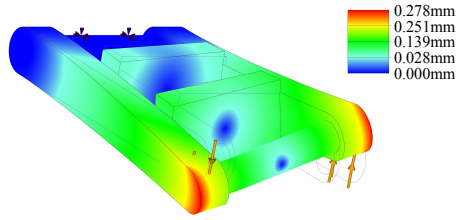


Figure 7.16 Deformed model of the simplified joint with the stiffener solution 2 that maximises ε. A scale factor of 10 is applied to better visualise the deformation.

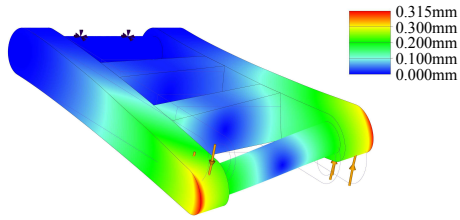


Figure 7.17 Deformed model of the simplified joint with the stiffener solution 2 that maximises η. A scale factor of 10 is applied to better visualise the deformation.

that maximise ε_2 and η_2. The two designs are depicted in Fig. 7.14 and 7.15. The corresponding structural static analyses are shown in Fig. 7.16 and 7.17.

Solution 1	w [mm]	m_1 [kg]	ε_1 [%]	η_1 [mm/kg]
ε_{max}	7.8	0.843	84.9	0.9
η_{max}	20.7	0.478	51.7	2.3
Solution 2	b [mm]	m_2 [kg]	ε_2 [%]	η_2 [mm/kg]
ε_{max}	15.3	0.543	47.3	1.3
η_{max}	16.9	0.491	39.9	1.6

Table 7.4 Summary of the results of the sensitivity analyses for solution 1 and 2.

		u_P [mm]	θ_P [$\times 10^{-3}$rad]	u_{EE} [mm]
Without stiffener		0.481	10.7	20.9
Solution 1	ε_{max}	0.073	1.6	3.2
	η_{max}	0.232	5.2	10.1
Solution 2	ε_{max}	0.254	5.6	11.0
	η_{max}	0.289	6.4	12.6

Table 7.5 End-effector displacement corresponding to the first joint without stiffener and the first joint with solution 1 and 2 for ε_{max} and η_{max}.

7.2.3 Results and Final Considerations

Figures 7.6 and 7.7 and figures 7.12 and 7.13 report the sensitivity analyses for solution 1 and 2, respectively, in terms of ε and η. Table 7.4 summarises the corresponding results. Solution 1 performs better in both performance indicators. Furthermore, in the range of w between the points of maximum efficacy (orange circle) and maximum efficiency (orange diamond), ε_1 and η_1 are monotonically decreasing and increasing, respectively. Since, in this range, the absolute local slope of ε_1 is much lower than that of η_1, it is possible to have a slight loss in efficacy (i.e. less displacement reduction) while retaining high performance in efficiency (i.e. less mass added). Consequently, different stiffener designs can suit the different joints of the robot depending on the magnitude of the torsional load that affects the joint itself. In addition, the displacement on the end-effector has been evaluated considering the robotic system in configuration depicted in Fig. 7.1 and mounting the two proposed stiffener on the first joint. Table 7.5 reports the comparison of the two displacements on the end-effector for both solutions with respect to the joint without stiffener. Solution 1 also performs better in terms of end-effector positioning accuracy. Furthermore, the proposed design for solution 1 can be easily manufactured starting from a cylindrical tube. Finally, this element can be mounted on the gear transmission joint without changing the assembly procedure so far defined.

CHAPTER 8

CONCLUSION AND FUTURE WORKS

This dissertation aimed to bridge the gap between theoretical modelling and physical realisation of tendon-driven hyper-redundant manipulators. The research transformed a virtual concept into a fully operational polymeric prototype. Key advancements focused on actuation efficiency, stiffness modulation, and structural optimisation for harsh and unstructured environments.

The development of the physical prototype implemented the design-for-assembly approach. Additive manufacturing with *PA*12 allowed for a lightweight structure with integrated electronics. A core innovation is the evaluation of the new active tensioning system. This mechanism replaced the fixed preload strategy. It dynamically compensated for slack during motion. Experimental results quantified the system's performance. The active tensioning system achieved a motion efficiency of 65.9%, while the static efficiency resulted 37.1%. This improvement confirms that dynamic friction is much lower than static friction in this routing configuration.

Stiffness modulation tests demonstrated the system's adaptability. A single global tensioner modulated the tip translational stiffness by a factor of four. The compliance distribution remained invariant across tension levels, which validated the use of scalar control strategies for tension control.

The research also introduced a data-driven framework for structural integrity. Bayesian Optimisation using Gaussian Processes accurately predicted worst-case stress scenarios without the need for expensive FEA simulations. The model achieved a mean relative error of 0.95%. This computational efficiency allowed the subsequent design of underwater modules through generative methods.

Finally, the work addressed underwater adaptation. The integration of generative design reduced link mass by up to 25.9% compared to parametric optimisation. This

mass reduction, combined with custom buoyant elements, achieved neutral buoyancy. This advanced the system closer to ROV platform integration.

8.1 Future Works

Future research will address specific physical limitations identified during the system validation.

The first challenge is to develop a prototype ready for deployment for inspection and maintenance tasks. A prototype made primarily of carbon fibre components would significantly improve the stiffness-to-weight ratio. Reducing the overall weight of the robot structure would also help decrease the size of the actuation unit. Furthermore, providing protection for the on-board electronics would bring the system closer to real-world deployment in harsh environments.

Although the active tensioning system appears to have relatively high efficiency during motion, it still experiences significant frictional losses. A detailed analysis of friction losses is necessary and can be achieved by employing the capstan equation and analysing the total wrap angles at the tendon-pulley interfaces. This would help determine the tensioning force to be applied to the tensioner, given the desired pre-tension required on the most disadvantaged tendon. The efficiency of the tensioning system could also be improved by redesigning the tendon routing during the tensioning stage, specifically by using fewer pulleys and shorter tendon paths. This would also help reduce the size of the tensioning part of the robotic system's actuation unit, making it smaller and easier to deploy.

Furthermore, while the current control architecture relies on kinematic mapping with static tension compensation, future research should integrate a full dynamic model into the control loop. By utilising high-frequency feedback from embedded optical sensors, a dynamic controller could actively modulate joint stiffness in real time.

REFERENCES

[1] C. Canali, A. Pistone, D. Ludovico, P. Guardiani, R. Gagliardi, L. De Mari Casareto Dal Verme, G. Sofia, and D. G. Caldwell, "Design of a novel long-reach cable-driven hyper-redundant snake-like manipulator for inspection and maintenance," *Applied Sciences*, vol. 12, no. 7, p. 3348, 2022.

[2] J. Sanderson, "Spreading the word," *Science*, vol. 321, pp. 12 – 12, 2008.

[3] L. Botti, E. Ferrari, and C. Mora, "Automated entry technologies for confined space work activities: A survey," *Journal of occupational and environmental hygiene*, vol. 14, no. 4, pp. 271–284, 2017.

[4] A. Datar, C. Pan, M. Nazeri, and X. Xiao, "Toward wheeled mobility on vertically challenging terrain: Platforms, datasets, and algorithms," in *2024 IEEE International Conference on Robotics and Automation (ICRA)*, pp. 16322–16329, IEEE, 2024.

[5] W. Khalil and E. Dombre, *Modeling, identification and control of robots*. Butterworth-Heinemann, 2004.

[6] R. Cieślak and A. Morecki, "Elephant trunk type elastic manipulator-a tool for bulk and liquid materials transportation," *Robotica*, vol. 17, no. 1, pp. 11–16, 1999.

[7] Y. Zhao, X. Song, X. Zhang, and X. Lu, "A hyper-redundant elephant's trunk robot with an open structure: design, kinematics, control and prototype," *Chinese Journal of Mechanical Engineering*, vol. 33, no. 1, pp. 1–19, 2020.

[8] M. W. Hannan and I. D. Walker, "Analysis and initial experiments for a novel elephant's trunk robot," in *Proceedings. 2000 IEEE/RSJ International Conference on Intelligent Robots and Systems (IROS 2000)(Cat. No. 00CH37113)*, vol. 1, pp. 330–337, IEEE, 2000.

[9] J. Clark, D. P. Noonan, V. Vitiello, M. H. Sodergren, J. Shang, C. J. Payne, T. P. Cundy, G.-Z. Yang, and A. Darzi, "A novel flexible hyper-redundant surgical robot: prototype evaluation using a single incision flexible access pelvic application as a clinical exemplar," *Surgical endoscopy*, vol. 29, pp. 658–667, 2015.

[10] F. Manara, A. Poka, D. Ludovico, A. Pistone, L. D. M. C. Dal Verme, C. Canali, G. Berselli, and D. G. Caldwell, "Tendon-driven hyper-redundant manipulators: A review on design solutions," *IEEE/ASME Transactions on Mechatronics*, 2025.

[11] A. Poka, F. Manara, D. Ludovico, A. Pistone, L. D. M. C. Dal Verme, C. Canali, G. Berselli, and D. G. Caldwell, "Alternative solutions to tendon-driven hyper-redundant manipulators: A review on design and actuation strategies," *IEEE/ASME Transactions on Mechatronics*, 2025.

[12] G. Robinson and J. B. C. Davies, "Continuum robots-a state of the art," in *Proceedings 1999 IEEE international conference on robotics and automation (Cat. No. 99CH36288C)*, vol. 4, pp. 2849–2854, IEEE, 1999.

[13] J. Yang, P. Jason, and K. Abdel-Malek, "A hyper-redundant continuous robot," in *Proceedings 2006 IEEE International Conference on Robotics and Automation, 2006. ICRA 2006.*, pp. 1854–1859, IEEE, 2006.

[14] H. Emet, B. Gür, and M. İ. C. Dede, "The design and kinematic representation of a soft robot in a simulation environment," *Robotica*, vol. 42, no. 1, pp. 139–152, 2024.

[15] A. Yeshmukhametov, K. Koganezawa, and Y. Yamamoto, "Design and kinematics of cable-driven continuum robot arm with universal joint backbone," in *2018 IEEE International Conference on Robotics and Biomimetics (ROBIO)*, pp. 2444–2449, IEEE, 2018.

[16] Y. Dai, Z. Li, X. Chen, X. Wang, and H. Yuan, "A novel space robot with triple cable-driven continuum arms for space grasping," *Micromachines*, vol. 14, no. 2, p. 416, 2023.

[17] M. Wang, X. Dong, W. Ba, A. Mohammad, D. Axinte, and A. Norton, "Design, modelling and validation of a novel extra slender continuum robot for in-situ inspection and repair in aeroengine," *Robotics and Computer-Integrated Manufacturing*, vol. 67, p. 102054, 2021.

[18] T.-D. Nguyen and J. Burgner-Kahrs, "A tendon-driven continuum robot with extensible sections," in *2015 IEEE/RSJ International Conference on Intelligent Robots and Systems (IROS)*, pp. 2130–2135, IEEE, 2015.

[19] Y. Zhang, H. Sun, Y. Jia, D. Huang, R. Li, Z. Mao, Y. Hu, J. Chen, S. Kuang, J. Tang, *et al.*, "A continuum robot with contractible and extensible length for neurosurgery," in *2018 IEEE 14th International Conference on Control and Automation (ICCA)*, pp. 1150–1155, IEEE, 2018.

[20] I. A. Gravagne, C. D. Rahn, and I. D. Walker, "Large deflection dynamics and control for planar continuum robots," *IEEE/ASME transactions on mechatronics*, vol. 8, no. 2, pp. 299–307, 2003.

[21] S. Dumitru, D. Cojocaru, and D. Marghitu, "Computer aided design of a hyper-redundant manipulator," *Advances in Electrical and Computer Engineering*, vol. 13, no. 4, pp. 51–57, 2013.

[22] J. Lin and Z.-H. Zhou, "Design and implementation of a cable-driven dexterous continuum manipulators in confined space usage," in *2022 International Conference on Electrical, Computer and Energy Technologies (ICECET)*, pp. 1–6, IEEE, 2022.

[23] J. S. Mehling, M. A. Diftler, M. Chu, and M. Valvo, "A minimally invasive tendril robot for in-space inspection," in *The First IEEE/RAS-EMBS International Conference on Biomedical Robotics and Biomechatronics, 2006. BioRob 2006.*, pp. 690–695, IEEE, 2006.

[24] X. Ye and W. J. Yoon, "Design of a bending mechanism for automated cystoscope," in *2012 IEEE International Conference on Automation Science and Engineering (CASE)*, pp. 261–266, IEEE, 2012.

[25] Z. Li, H. Yu, H. Ren, P. W. Chiu, and R. Du, "A novel constrained tendon-driven serpentine manipulator," in *2015 IEEE/RSJ International Conference on Intelligent Robots and Systems (IROS)*, pp. 5966–5971, IEEE, 2015.

[26] H. Hu, P. Wang, B. Zhao, M. Li, and L. Sun, "Design of a novel snake-like robotic colonoscope," in *2009 IEEE International Conference on Robotics and Biomimetics (ROBIO)*, pp. 1957–1961, IEEE, 2009.

[27] J. Santoso and C. D. Onal, "An origami continuum robot capable of precise motion through torsionally stiff body and smooth inverse kinematics," *Soft Robotics*, vol. 8, no. 4, pp. 371–386, 2021.

[28] K. Zhang, C. Qiu, and J. S. Dai, "An extensible continuum robot with integrated origami parallel modules," *Journal of Mechanisms and Robotics*, vol. 8, no. 3, p. 031010, 2016.

[29] Y. Zhang and G. Gao, "Design and kinematics on biased channel retractable continuum robot," in *2019 2nd World Conference on Mechanical Engineering and Intelligent Manufacturing (WCMEIM)*, pp. 541–544, IEEE, 2019.

[30] A. Gao, H. Liu, Y. Zhou, Z. Yang, Z. Wang, and H. Li, "A cross-helical tendons actuated dexterous continuum manipulator," in *2015 IEEE/RSJ International Conference on Intelligent Robots and Systems (IROS)*, pp. 2012–2017, IEEE, 2015.

[31] J. Starke, E. Amanov, M. T. Chikhaoui, and J. Burgner-Kahrs, "On the merits of helical tendon routing in continuum robots," in *2017 IEEE/RSJ International Conference on Intelligent Robots and Systems (IROS)*, pp. 6470–6476, IEEE, 2017.

[32] K. Oliver-Butler, J. Till, and C. Rucker, "Continuum robot stiffness under external loads and prescribed tendon displacements," *IEEE Transactions on Robotics*, vol. 35, no. 2, pp. 403–419, 2019.

[33] N. G. Cheng, M. B. Lobovsky, S. J. Keating, A. M. Setapen, K. I. Gero, A. E. Hosoi, and K. D. Iagnemma, "Design and analysis of a robust, low-cost, highly articulated manipulator enabled by jamming of granular media," in *2012 IEEE international conference on robotics and automation*, pp. 4328–4333, IEEE, 2012.

[34] Y. Zhao, Y. Shan, J. Zhang, K. Guo, L. Qi, L. Han, and H. Yu, "A soft continuum robot, with a large variable-stiffness range, based on jamming," *Bioinspiration & biomimetics*, vol. 14, no. 6, p. 066007, 2019.

[35] W. J. Marais and A. H. Göktogan, "Design and control of cram: A highly articulated cable-driven remote access manipulator for confined space inspection," in *Proceedings of the Australasian Conference on Robotics and Automation (ACRA-2017), Sydney, Australia*, pp. 11–13, 2017.

[36] L. Tang, J. Wang, Y. Zheng, G. Gu, L. Zhu, and X. Zhu, "Design of a cable-driven hyper-redundant robot with experimental validation," *International Journal of Advanced Robotic Systems*, vol. 14, no. 5, p. 1729881417734458, 2017.

[37] Y. Sklyarenko, F. Schreiber, M. Kolbus, F. Wobbe, and W. Schumacher, "Design of the new modular tendon-driven manipulator tendrim," in *2009 IEEE International Conference on Robotics and Biomimetics (ROBIO)*, pp. 574–579, IEEE, 2009.

[38] R. Al-Khulaidi, R. Akmeliawati, S. Grainger, and T.-F. Lu, "Structural optimisation and design of a cable-driven hyper-redundant manipulator for confined semi-structured environments," *Sensors*, vol. 22, no. 22, p. 8632, 2022.

[39] G. Endo, A. Horigome, and A. Takata, "Super dragon: A 10-m-long-coupled tendon-driven articulated manipulator," *IEEE Robotics and Automation Letters*, vol. 4, no. 2, pp. 934–941, 2019.

[40] Y. Zheng, B. Wu, Y. Chen, L. Zeng, G. Gu, X. Zhu, and K. Xu, "Design and validation of cable-driven hyper-redundant manipulator with a closed-loop puller-follower controller," *Mechatronics*, vol. 78, p. 102605, 2021.

[41] T. Chanthasopeephan, P. Srikirin, M. Srisap, and A. Rattapat, "Flexure design of a compliant modular hyper-redundant manipulator," in *2017 26th IEEE International Symposium on Robot and Human Interactive Communication (RO-MAN)*, pp. 1394–1399, IEEE, 2017.

[42] S. Jainandunsing, J. L. Herder, Y. Takeda, and D. Matsuura, "Design of a compliant environmentally interactive snake-like manipulator," in *ROMANSY 21-Robot Design, Dynamics and Control: Proceedings of the 21st CISM-IFToMM Symposium, June 20-23, Udine, Italy*, pp. 233–240, Springer, 2016.

[43] X. Dong, D. Axinte, D. Palmer, S. Cobos, M. Raffles, A. Rabani, and J. Kell, "Development of a slender continuum robotic system for on-wing inspection/repair of gas turbine engines," *Robotics and computer-integrated manufacturing*, vol. 44, pp. 218–229, 2017.

[44] X. Wei, Y. Zhang, F. Ju, H. Guo, B. Chen, and H. Wu, "Design and analysis of a continuum robot for transnasal skull base surgery," *The International Journal of Medical Robotics and Computer Assisted Surgery*, vol. 17, no. 6, p. e2328, 2021.

[45] Z. Yang, L. Yang, Y. Sun, and X. Chen, "Comprehensive kinetostatic modeling and morphology characterization of cable-driven continuum robots for in-situ aero-engine maintenance," *Frontiers of Mechanical Engineering*, vol. 18, no. 3, p. 40, 2023.

[46] Y. Sun, Y. Liu, and T. C. Lueth, "Optimization of stress distribution in tendon-driven continuum robots using fish-tail-inspired method," *IEEE Robotics and Automation Letters*, vol. 7, no. 2, pp. 3380–3387, 2022.

[47] H. Liu, Z. Ji, J. Li, Y. Zhou, C. Wang, and P. Ba, "As shape continuum robot with a single actuation structured by niti slices," in *2017 IEEE International Conference on Robotics and Biomimetics (ROBIO)*, pp. 401–405, IEEE, 2017.

[48] M. Li, R. Kang, S. Geng, and E. Guglielmino, "Design and control of a tendon-driven continuum robot," *Transactions of the Institute of Measurement and Control*, vol. 40, no. 11, pp. 3263–3272, 2018.

[49] D.-G. Choi, B.-J. Yi, and W.-K. Kim, "Design of a spring backbone micro endoscope," in *2007 IEEE/RSJ International Conference on Intelligent Robots and Systems*, pp. 1815–1821, IEEE, 2007.

[50] A. Yeshmukhametov, K. Koganezawa, and Y. Yamamoto, "A novel discrete wire-driven continuum robot arm with passive sliding disc: Design, kinematics and passive tension control," *Robotics*, vol. 8, no. 3, p. 51, 2019.

[51] J. Tang, Y. Zhang, F. Huang, J. Li, Z. Chen, W. Song, S. Zhu, and J. Gu, "Design and kinematic control of the cable-driven hyper-redundant manipulator for potential underwater applications," *Applied Sciences*, vol. 9, no. 6, p. 1142, 2019.

[52] P. Jagadeesan, S. Sivaprakasham, D. Kumar, and M. Madhu, "A 'multilink spatial hyper redundant' manipulator," in *Advances in Reconfigurable Mechanisms and Robots I*, pp. 869–875, Springer, 2012.

[53] P. You, Z. Liu, and Z. Ma, "Multibody dynamic modeling and analysis of cable-driven snake robot considering clearance and friction based on ale method," *Mechanism and Machine Theory*, vol. 184, p. 105313, 2023.

[54] T. Liu, W. Xu, T. Yang, and Y. Li, "A hybrid active and passive cable-driven segmented redundant manipulator: design, kinematics, and planning," *IEEE/ASME Transactions on Mechatronics*, vol. 26, no. 2, pp. 930–942, 2020.

[55] P. Dutta, K. K. Gotewal, N. Rastogi, R. Tiwari, and M. M, "A hyper-redundant robot development for tokamak inspection," in *Proceedings of the Advances in Robotics*, Association for Computing Machinery, 2017.

[56] L. Huang, B. Liu, L. Yin, P. Zeng, and Y. Yang, "Design and validation of a novel cable-driven hyper-redundant robot based on decoupled joints," *Journal of Robotics*, vol. 2021, pp. 1–16, 2021.

[57] X. Jin, J. Zhao, M. Feng, L. Hao, and Q. Li, "Snake-like surgical forceps for robot-assisted minimally invasive surgery," *The International Journal of Medical Robotics and Computer Assisted Surgery*, vol. 14, no. 4, p. e1908, 2018.

[58] P. Guardiani, D. Ludovico, A. Pistone, H. Abidi, I. Zaplana, J. Lee, D. G. Caldwell, and C. Canali, "Design and analysis of a fully actuated cable-driven joint for hyper-redundant robots with optimal cable routing," *Journal of Mechanisms and Robotics*, vol. 14, no. 2, p. 021006, 2022.

[59] D. Ludovico, P. Guardiani, A. Pistone, J. Lee, F. Cannella, D. G. Caldwell, and C. Canali, "Modeling cable-driven joint dynamics and friction: a bond-graph

approach," in *2020 IEEE/RSJ International Conference on Intelligent Robots and Systems (IROS)*, pp. 7285–7291, IEEE, 2020.

[60] J. Kim, S.-i. Kwon, Y. Moon, and K. Kim, "Cable-movable rolling joint to expand workspace under high external load in a hyper-redundant manipulator," *IEEE/ASME Transactions on Mechatronics*, vol. 27, no. 1, pp. 501–512, 2021.

[61] D. Dragone, F. F. Donadio, C. Mirabelli, C. Cosentino, F. Amato, P. Zaffino, M. F. Spadea, D. La Torre, and A. Merola, "Design and experimental validation of a 3d-printed embedded-sensing continuum robot for neurosurgery," *Micromachines*, vol. 14, no. 9, p. 1743, 2023.

[62] L. Ciurezu-Gherghe, N. Dumitru, D. Geonea, and S. Bostina, "Snake-like flexible mechanical system with applications in exploratory activities," in *2022 IEEE International Conference on Automation, Quality and Testing, Robotics (AQTR)*, pp. 1–5, IEEE, 2022.

[63] S. Kwon, J. Kim, Y. Moon, and K. Kim, "Hyper-redundant manipulator capable of adjusting its non-uniform curvature with discrete stiffness distribution," *Applied Sciences*, vol. 12, no. 1, p. 482, 2022.

[64] P. Berthet-Rayne, K. Leibrandt, K. Kim, C. A. Seneci, J. Shang, and G.-Z. Yang, "Rolling-joint design optimization for tendon driven snake-like surgical robots," in *2018 IEEE/RSJ international conference on intelligent robots and systems (IROS)*, pp. 4964–4971, IEEE, 2018.

[65] Q. Gao, G. Ji, and Z. Sun, "Robust shape-distortion prediction for a wire-driven hyper-redundant manipulator with engaging rolling joints," *IEEE Transactions on Medical Robotics and Bionics*, 2023.

[66] M. Hwang and D.-S. Kwon, "Strong continuum manipulator for flexible endoscopic surgery," *IEEE/ASME Transactions on Mechatronics*, vol. 24, no. 5, pp. 2193–2203, 2019.

[67] D. Ji, T. H. Kang, S. Shim, S. Lee, and J. Hong, "Wire-driven flexible manipulator with constrained spherical joints for minimally invasive surgery," *International journal of computer assisted radiology and surgery*, vol. 14, pp. 1365–1377, 2019.

[68] G. Qin, Q. Wang, C. Li, A. Ji, H. Wu, Z. Yang, and S. Wen, "Design and development of a cable-driven elephant trunk robot with variable cross-sections," *Industrial Robot: the international journal of robotics research and application*, vol. 50, no. 3, pp. 520–529, 2023.

[69] Z. Qiang and G. Fang, "Design and analysis of a new cable-driven hyper redundant manipulator," in *2010 International Conference on Intelligent Computation Technology and Automation*, vol. 1, pp. 1111–1114, IEEE, 2010.

[70] J. M. You, H. Kim, J. Kim, and D.-S. Kwon, "Design and analysis of high-stiffness hyperredundant manipulator with sigma-shaped wire path and rolling joints," *IEEE Robotics and Automation Letters*, vol. 6, no. 4, pp. 7357–7364, 2021.

[71] H. Kim, J. M. You, M. Hwang, K.-U. Kyung, and D.-S. Kwon, "Sigmoidal auxiliary tendon-driven mechanism reinforcing structural stiffness of hyper-redundant manipulator for endoscopic surgery," *Soft Robotics*, vol. 10, no. 2, pp. 234–245, 2023.

[72] F. Wang, J. Peng, H. Yuan, B. Liang, and W. Xu, "Cable configuration and driving force analysis of a cable-driven hyper-redundant manipulator," in *2021 6th IEEE International Conference on Advanced Robotics and Mechatronics (ICARM)*, pp. 465–470, IEEE, 2021.

[73] Z. Li, J. Deng, Y. Zheng, C. Liu, and G. Gu, "Cable length estimation for a hyper-redundant robot based on cable hole clearance calculation," in *2023 IEEE 19th International Conference on Automation Science and Engineering (CASE)*, pp. 1–7, IEEE, 2023.

[74] D. Xu, E. Li, Z. Liang, and Z. Gao, "Design and tension modeling of a novel cable-driven rigid snake-like manipulator," *Journal of Intelligent & Robotic Systems*, vol. 99, pp. 211–228, 2020.

[75] P. Jianqing, W. Haoxuan, L. Tianliang, and H. Yu, "Workspace, stiffness analysis and design optimization of coupled active-passive multilink cable-driven space robots for on-orbit services," *Chinese Journal of Aeronautics*, vol. 36, no. 2, pp. 402–416, 2023.

[76] D. Diek, K. Stuja, and M. Aburaia, "Design and development of a flexible, cable-controlled and hyperredundant robot with strength-adjustable ball joints," in *Proceedings of the 33rd DAAAM International Symposium*, pp. 0024–0028, 2022.

[77] A. Pistone, D. Ludovico, L. D. M. C. Dal Verme, S. Leggieri, C. Canali, and D. G. Caldwell, "Modelling and control of manipulators for inspection and maintenance in challenging environments: A literature review," *Annual Reviews in Control*, vol. 57, p. 100949, 2024.

[78] S. Kolachalama and S. Lakshmanan, "Continuum robots for manipulation applications: A survey," *Journal of Robotics*, vol. 2020, no. 1, p. 4187048, 2020.

[79] Z. Mu, L. Zhang, L. Yan, Z. Li, R. Dong, C. Wang, and N. Ding, "Hyper-redundant manipulators for operations in confined space: Typical applications, key technologies, and grand challenges," *IEEE Transactions on Aerospace and Electronic Systems*, vol. 58, no. 6, pp. 4928–4937, 2022.

[80] B. Zhao, W. Zhang, Z. Zhang, X. Zhu, and K. Xu, "Continuum manipulator with redundant backbones and constrained bending curvature for continuously variable stiffness," in *2018 IEEE/RSJ International Conference on Intelligent Robots and Systems (IROS)*, pp. 7492–7499, IEEE, 2018.

[81] S. Liu, Z. Yang, Z. Zhu, L. Han, X. Zhu, and K. Xu, "Development of a dexterous continuum manipulator for exploration and inspection in confined spaces," *Industrial Robot: An International Journal*, vol. 43, no. 3, pp. 284–295, 2016.

[82] M. Wang, J. Yuan, S. Bao, L. Du, and S. Ma, "Research on self-stiffness adjustment of growth-controllable continuum robot (gccr) based on elastic force transmission," *Biomimetics*, vol. 8, no. 5, p. 433, 2023.

[83] H. Liu, H. Wang, S. Fan, and D. Yang, "Bio-inspired design of alternate rigid-flexible segments to improve the stiffness of a continuum manipulator," *Science China Technological Sciences*, vol. 63, no. 8, pp. 1549–1559, 2020.

[84] K. Xu, M. Fu, and J. Zhao, "An experimental kinestatic comparison between continuum manipulators with structural variations," in *2014 IEEE International Conference on Robotics and Automation (ICRA)*, pp. 3258–3264, IEEE, 2014.

[85] Y.-J. Kim, S. Cheng, S. Kim, and K. Iagnemma, "A novel layer jamming mechanism with tunable stiffness capability for minimally invasive surgery," *IEEE Transactions on Robotics*, vol. 29, no. 4, pp. 1031–1042, 2013.

[86] P. E. Dupont, J. Lock, B. Itkowitz, and E. Butler, "Design and control of concentric-tube robots," *IEEE Transactions on Robotics*, vol. 26, no. 2, pp. 209–225, 2009.

[87] T. K. Morimoto and A. M. Okamura, "Design of 3-d printed concentric tube robots," *IEEE Transactions on Robotics*, vol. 32, no. 6, pp. 1419–1430, 2016.

[88] R. J. Webster, A. M. Okamura, and N. J. Cowan, "Toward active cannulas: Miniature snake-like surgical robots," in *2006 IEEE/RSJ international conference on intelligent robots and systems*, pp. 2857–2863, IEEE, 2006.

[89] E. Lanteigne and A. Jnifene, "An experimental study on a sma driven pressurized hyper-redundant manipulator," *Journal of Intelligent Material Systems and Structures*, vol. 19, no. 9, pp. 1067–1076, 2008.

[90] M. A. Mandolino, Y. Goergen, P. Motzki, and G. Rizzello, "Design and characterization of a fully integrated continuum robot actuated by shape memory alloy wires," in *2022 IEEE 17th International Conference on Advanced Motion Control (AMC)*, pp. 6–11, IEEE, 2022.

[91] Y. Li and Y. Chen, "The ultimate hyper redundant robotic arm based on omnidirectional joints," in *2015 IEEE International Conference on Mechatronics and Automation (ICMA)*, pp. 1840–1845, IEEE, 2015.

[92] V. A. Sujan and S. Dubowsky, "Design of a lightweight hyper-redundant deployable binary manipulator," *J. Mech. Des.*, vol. 126, no. 1, pp. 29–39, 2004.

[93] E. Tzorakoleftherakis, A. Mavrommati, and A. Tzes, "Design and implementation of a binary redundant manipulator with cascaded modules," *Journal of Mechanisms and Robotics*, vol. 8, no. 1, p. 011002, 2016.

[94] R. Kang, D. T. Branson, T. Zheng, E. Guglielmino, and D. G. Caldwell, "Design, modeling and control of a pneumatically actuated manipulator inspired by biological continuum structures," *Bioinspiration & biomimetics*, vol. 8, no. 3, p. 036008, 2013.

[95] X. Gao, X. Li, C. Zhao, L. Hao, and C. Xiang, "Variable stiffness structural design of a dual-segment continuum manipulator with independent stiffness and angular position," *Robotics and Computer-Integrated Manufacturing*, vol. 67, p. 102000, 2021.

[96] W. McMahan, V. Chitrakaran, M. Csencsits, D. Dawson, I. D. Walker, B. A. Jones, M. Pritts, D. Dienno, M. Grissom, and C. D. Rahn, "Field trials and testing of the octarm continuum manipulator," in *Proceedings 2006 IEEE International Conference on Robotics and Automation, 2006. ICRA 2006.*, pp. 2336–2341, IEEE, 2006.

[97] J. D. Greer, T. K. Morimoto, A. M. Okamura, and E. W. Hawkes, "Series pneumatic artificial muscles (spams) and application to a soft continuum robot," in *2017 IEEE International Conference on Robotics and Automation (ICRA)*, pp. 5503–5510, IEEE, 2017.

[98] M. S. Sofla, M. J. Sadigh, and M. Zareinejad, "Design and dynamic modeling of a continuum and compliant manipulator with large workspace," *Mechanism and Machine Theory*, vol. 164, p. 104413, 2021.

[99] Y. Shapiro, A. Wolf, and K. Gabor, "Bi-bellows: Pneumatic bending actuator," *Sensors and Actuators A: Physical*, vol. 167, no. 2, pp. 484–494, 2011.

[100] Y. Bailly, Y. Amirat, and G. Fried, "Modeling and control of a continuum style microrobot for endovascular surgery," *IEEE Transactions on Robotics*, vol. 27, no. 5, pp. 1024–1030, 2011.

[101] H. Wang, H. Xu, F. Yu, X. Li, C. Yang, S. Chen, J. Chen, Y. Zhang, and X. Zhou, "Modeling and experiments on the swallowing and disgorging characteristics of an underwater continuum manipulator," in *2020 IEEE International Conference on Robotics and Automation (ICRA)*, pp. 2946–2952, IEEE, 2020.

[102] D. Lin, N. Jiao, Z. Wang, and L. Liu, "A magnetic continuum robot with multi-mode control using opposite-magnetized magnets," *IEEE Robotics and Automation Letters*, vol. 6, no. 2, pp. 2485–2492, 2021.

[103] S. Tappe, J. Kotlarski, T. Ortmaier, M. Dörbaum, A. Mertens, and B. Ponick, "The kinematic synthesis of a spatial, hyper-redundant system based on binary electromagnetic actuators," in *2015 6th International Conference on Automation, Robotics and Applications (ICARA)*, pp. 211–216, IEEE, 2015.

[104] Y. Liu, Z. Ge, S. Yang, I. D. Walker, and Z. Ju, "Elephant's trunk robot: An extremely versatile under-actuated continuum robot driven by a single motor," *Journal of Mechanisms and Robotics*, vol. 11, no. 5, p. 051008, 2019.

[105] S. Bayani, R. Rastegari, and F. C. Samavati, "Design of hyper redundant robot using ball screw mechanism approach," in *2015 IEEE International Conference on Advanced Intelligent Mechatronics (AIM)*, pp. 1271–1276, IEEE, 2015.

[106] A. Bayram and M. Kemal Özgören, "The conceptual design of a spatial binary hyper redundant manipulator and its forward kinematics," *Proceedings of the*

Institution of Mechanical Engineers, Part C: Journal of Mechanical Engineering Science, vol. 226, no. 1, pp. 217–227, 2012.

[107] J. Mintenbeck and R. Estana, "Design, modelling and control of a hyper-redundant 3-rps parallel mechanism," in *2010 IEEE International Conference on Robotics and Biomimetics*, pp. 591–596, IEEE, 2010.

[108] O. Salomon and A. Wolf, "Inclined links hyper-redundant elephant trunk-like robot," *Journal of Mechanisms and Robotics*, 2012.

[109] A. B. Jamali, M. R. Khan, and M. Rahman, "Design and control of variable length hyper redundant robot," *Procedia Engineering*, vol. 41, pp. 1105–1113, 2012.

[110] C. Pogue, P. Rao, Q. Peyron, J. Kim, J. Burgner-Kahrs, and E. Diller, "Multiple curvatures in a tendon-driven continuum robot using a novel magnetic locking mechanism," in *2022 IEEE/RSJ International Conference on Intelligent Robots and Systems (IROS)*, pp. 472–479, IEEE, 2022.

[111] W. McMahan, B. A. Jones, and I. D. Walker, "Design and implementation of a multi-section continuum robot: Air-octor," in *2005 IEEE/RSJ international conference on intelligent robots and systems*, pp. 2578–2585, IEEE, 2005.

[112] D. Sui, S. Zhao, T. Wang, Y. Liu, Y. Zhu, and J. Zhao, "Design of a bio-inspired extensible continuum manipulator with variable stiffness," *Journal of Bionic Engineering*, pp. 1–14, 2022.

[113] N. Ma, "Design and modelling of a continuum robot with soft stiffness-adjustable elements for confined environments," *Authorea Preprints*, 2023.

[114] E. Amanov, J. Granna, and J. Burgner-Kahrs, "Toward improving path following motion: hybrid continuum robot design," in *2017 IEEE international conference on robotics and automation (ICRA)*, pp. 4666–4672, IEEE, 2017.

[115] M. C. Lastinger, S. Verma, A. D. Kapadia, and I. D. Walker, "Tree: A variable topology, branching continuum robot," in *2019 International Conference on Robotics and Automation (ICRA)*, pp. 5365–5371, IEEE, 2019.

[116] P. Wang, S. Guo, X. Wang, and Y. Wu, "Design and analysis of a novel variable stiffness continuum robot with built-in winding-styled ropes," *IEEE Robotics and Automation Letters*, vol. 7, no. 3, pp. 6375–6382, 2022.

[117] X. Jing, J. Jiang, F. Xie, C. Zhang, S. Chen, and L. Yang, "Continuum manipulator with rigid-flexible coupling structure," *IEEE Robotics and Automation Letters*, vol. 7, no. 4, pp. 11386–11393, 2022.

[118] P. Guardiani, "Design of a cable-driven hyper-redundant robot with optimal cable routing," -, 2021.

[119] G. Mengesha, "Design optimization in structural engineering: A systematic review of computational techniques and real-world applications," *Available at SSRN 5254589*, 2025.

[120] D. Prayogo, W. Hauwing, F. Wong, D. Tjandra, *et al.*, "Structural design optimization using particle swarm optimization and its variants," in *IOP Conference Series: Earth and Environmental Science*, vol. 506, p. 012048, IOP Publishing, 2020.

[121] Y. Karafi, Z. Moussaoui, and B. Abou El Majd, "Simultaneous surrogate modeling and dimension reduction using unsupervised learning. application to parametric wing shape optimization," *Math. Model. Comput*, vol. 11, no. 1, pp. 154–165, 2024.

[122] E. Tromme, D. Tortorelli, O. Brüls, and P. Duysinx, "Structural optimization of multibody system components described using level set techniques," *Structural and Multidisciplinary Optimization*, vol. 52, no. 5, pp. 959–971, 2015.

[123] J. A. Paulson and C. Tsay, "Bayesian optimization as a flexible and efficient design framework for sustainable process systems," *Current Opinion in Green and Sustainable Chemistry*, vol. 51, p. 100983, 2025.

[124] Q. D. Tran, D. Shin, and G.-W. Jang, "Bayesian optimization-based topology optimization using moving morphable bars for flexible structure design problems," *Engineering Structures*, vol. 300, p. 117103, 2024.

[125] Y. Kim, Z. Pan, and K. Hauser, "Mo-bbo: Multi-objective bilevel bayesian optimization for robot and behavior co-design," in *2021 IEEE International Conference on Robotics and Automation (ICRA)*, pp. 9877–9883, IEEE, 2021.

[126] W. F. Jenkins, P. Gerstoft, and Y. Park, "Bayesian optimization with gaussian process surrogate model for source localization," *The Journal of the Acoustical Society of America*, vol. 154, no. 3, pp. 1459–1470, 2023.

[127] S. Rana, C. Li, S. Gupta, V. Nguyen, and S. Venkatesh, "High dimensional bayesian optimization with elastic gaussian process," in *International conference on machine learning*, pp. 2883–2891, PMLR, 2017.

[128] M. A. Osborne, R. Garnett, and S. J. Roberts, "Gaussian processes for global optimization," *Oxford University Research Archive*, 2009.

[129] A. De Freitas, R. W. Focke, C. Beyers, and P. De Villiers, "Global optimization for resource allocation in a networked-surveillance radar," in *2019 22th International Conference on Information Fusion (FUSION)*, pp. 1–8, IEEE, 2019.

[130] N. Qin, X. Zhou, J. Wang, and C. Shen, "Bayesian optimization: Model comparison with different benchmark functions," in *2021 International Conference on Signal Processing and Machine Learning (CONF-SPML)*, pp. 329–333, IEEE, 2021.

[131] D. Rajaram, T. G. Puranik, S. Ashwin Renganathan, W. Sung, O. P. Fischer, D. N. Mavris, and A. Ramamurthy, "Empirical assessment of deep gaussian process surrogate models for engineering problems," *Journal of Aircraft*, vol. 58, no. 1, pp. 182–196, 2021.

[132] A. Candelieri, "A gentle introduction to bayesian optimization," in *2021 Winter Simulation Conference (WSC)*, pp. 1–16, IEEE, 2021.

[133] M. Diessner, J. O'Connor, A. Wynn, S. Laizet, Y. Guan, K. Wilson, and R. D. Whalley, "Investigating bayesian optimization for expensive-to-evaluate black box functions: Application in fluid dynamics," *Frontiers in Applied Mathematics and Statistics*, vol. 8, p. 1076296, 2022.

[134] H. Liu, Y.-S. Ong, X. Shen, and J. Cai, "When gaussian process meets big data: A review of scalable gps," *IEEE transactions on neural networks and learning systems*, vol. 31, no. 11, pp. 4405–4423, 2020.

[135] A. Grigorievskiy and J. Karhunen, "Gaussian process kernels for popular state-space time series models," in *2016 International Joint Conference on Neural Networks (IJCNN)*, pp. 3354–3363, IEEE, 2016.

[136] R. Le Riche and V. Picheny, "Revisiting bayesian optimization in the light of the coco benchmark," *Structural and Multidisciplinary Optimization*, vol. 64, no. 5, pp. 3063–3087, 2021.

[137] A. Butler, R. D. Haynes, T. D. Humphries, and P. Ranjan, "Efficient optimization of the likelihood function in gaussian process modelling," *Computational Statistics & Data Analysis*, vol. 73, pp. 40–52, 2014.

[138] A. Damianou and N. D. Lawrence, "Deep gaussian processes," in *Artificial intelligence and statistics*, pp. 207–215, PMLR, 2013.

[139] W. Gan, Z. Ji, and Y. Liang, "Acquisition functions in bayesian optimization," in *2021 2nd international conference on big data & artificial intelligence & software engineering (ICBASE)*, pp. 129–135, IEEE, 2021.

[140] F. Manara, A. Poka, D. Ludovico, L. D. M. C. Dal Verme, C. Canali, G. Berselli, and D. G. Caldwell, "A hyper-redundant manipulator with an active tendon tensioning system (under review)," *IEEE/ASME Transactions on Mechatronics*, 2026.

[141] S. Wolf, G. Grioli, O. Eiberger, W. Friedl, M. Grebenstein, H. Höppner, E. Burdet, D. G. Caldwell, R. Carloni, M. G. Catalano, *et al.*, "Variable stiffness actuators: Review on design and components," *IEEE/ASME transactions on mechatronics*, vol. 21, no. 5, pp. 2418–2430, 2015.

[142] M. Usman and A. Raza, "Development of adjustable stiffness actuator by varying lever arm length," *Journal of the Chinese institute of engineers*, vol. 40, no. 8, pp. 651–658, 2017.

[143] A. Jafari, N. G. Tsagarakis, B. Vanderborght, and D. G. Caldwell, "A novel actuator with adjustable stiffness (awas)," in *2010 IEEE/RSJ international conference on intelligent robots and systems*, pp. 4201–4206, IEEE, 2010.

[144] S. A. Migliore, E. A. Brown, and S. P. DeWeerth, "Biologically inspired joint stiffness control," in *Proceedings of the 2005 IEEE international conference on robotics and automation*, pp. 4508–4513, IEEE, 2005.

[145] A. Poka, F. Manara, D. Ludovico, L. D. M. C. Dal Verme, C. Canali, G. Berselli, and D. G. Caldwell, "A variable-stiffness tendon-driven manipulator with an active

tensioning system (under review)," *IEEE/ASME Transactions on Mechatronics*, 2026.

[146] P. Merriaux, Y. Dupuis, R. Boutteau, P. Vasseur, and X. Savatier, "A study of vicon system positioning performance," *Sensors*, vol. 17, no. 7, p. 1591, 2017.

[147] ME Systeme, "Km26z 1kn force sensor," 2025. (accessed 22 December 2025).

[148] O. A. Aguirre-Castro, E. Inzunza-González, E. E. García-Guerrero, E. Tlelo-Cuautle, O. R. López-Bonilla, J. E. Olguín-Tiznado, and J. R. Cárdenas-Valdez, "Design and construction of an rov for underwater exploration," *Sensors*, vol. 19, no. 24, p. 5387, 2019.

[149] J. Zhou, Y. Si, and Y. Chen, "A review of subsea auv technology," *Journal of Marine Science and Engineering*, vol. 11, no. 6, p. 1119, 2023.

[150] A. Birk, T. Doernbach, C. Mueller, T. Łuczynski, A. G. Chavez, D. Koehntopp, A. Kupcsik, S. Calinon, A. K. Tanwani, G. Antonelli, *et al.*, "Dexterous underwater manipulation from onshore locations: Streamlining efficiencies for remotely operated underwater vehicles," *IEEE Robotics & Automation Magazine*, vol. 25, no. 4, pp. 24–33, 2018.

[151] P. Liljebäck and R. Mills, "Eelume: A flexible and subsea resident imr vehicle," in *Oceans 2017-Aberdeen*, pp. 1–4, IEEE, 2017.

[152] F. Lyu, X. Xu, X. Zha, Z. Li, and H. Yuan, "A snake eel inspired multi-joint underwater inspection robot for undersea infrastructure intelligent maintenance," in *OCEANS 2022-Chennai*, pp. 1–6, IEEE, 2022.

[153] A. Poka, D. Ludovico, F. Manara, L. D. M. C. Dal Verme, C. Canali, G. Berselli, D. G. Caldwell, and J. Jovanova, "Design of a lightweight and slender hyper-redundant manipulator for underwater applications," *Ocean Engineering*, vol. 342, p. 122800, 2025.

[154] A. Poka, D. Ludovico, F. Manara, L. De Mari Casareto Dal Verme, C. Canali, G. Berselli, D. G. Caldwell, and J. Jovanova, "Underwater snake-like robots: a review on design, actuation, and modelling methods," *The International Journal of Advanced Manufacturing Technology*, vol. 139, no. 11, pp. 5445–5460, 2025.

[155] F. Xue, Y. Fan, and Z. Fan, "Design and kinematics analysis for a cable-driven underwater snake arm robot," in *Journal of Physics: Conference Series*, vol. 1654, p. 012028, IOP Publishing, 2020.

[156] J. L. Sitler and L. Wang, "A modular open-source continuum manipulator for underwater remotely operated vehicles," *Journal of Mechanisms and Robotics*, vol. 14, no. 6, p. 060906, 2022.

[157] E. Guglielmino, D. Branson, and P. Silvestri, "A bio-inspired flexible arm for subsea inspection: A water hydraulically actuated continuum manipulator," *Journal of Marine Science and Engineering*, vol. 13, no. 4, p. 676, 2025.

[158] Y. Jia, Z. Zhang, W. Sun, K. Zhang, Y. Chen, and Y. Gong, "Study of bionic module driven by water hydraulic artificial muscles for underwater continuum robot," *Marine Systems & Ocean Technology*, vol. 20, no. 2, pp. 1–13, 2025.

[159] F. Xue and Z. Fan, "Kinematic control of a cable-driven snake-like manipulator for deep-water based on fuzzy pid controller," *Proceedings of the Institution of Mechanical Engineers, Part I: Journal of Systems and Control Engineering*, vol. 236, no. 5, pp. 989–998, 2022.

[160] Y. Li, F. Shen, Z. Lang, M. Cai, Q. Zeng, Q. Liu, and F. Cai, "An underwater near-infrared spectral continuum robot as a tool for in situ detection and classification," *Measurement*, vol. 216, p. 112913, 2023.

[161] N. Ma, D. Cheneler, and S. D. Monk, "Improving the kinematic accuracy of a collaborative continuum robot by using flexure-hinges," *Heliyon*, vol. 10, no. 4, 2024.

[162] L. Barbieri, F. Bruno, A. Gallo, M. Muzzupappa, and M. L. Russo, "Design, prototyping and testing of a modular small-sized underwater robotic arm controlled through a master-slave approach," *Ocean Engineering*, vol. 158, pp. 253–262, 2018.

[163] C. M. Sourkounis, T. Kwasnitschka, and A. Raatz, "Tendon-driven continuum robot for deep-sea application," in *2024 IEEE International Conference on Robotics and Automation (ICRA)*, pp. 1498–1504, IEEE, 2024.

[164] R. Kang, A. Kazakidi, E. Guglielmino, D. T. Branson, D. P. Tsakiris, J. A. Ekaterinaris, and D. G. Caldwell, "Dynamic model of a hyper-redundant, octopus-like manipulator for underwater applications," in *2011 IEEE/RSJ International Conference on Intelligent Robots and Systems*, pp. 4054–4059, IEEE, 2011.

[165] Z. Gong, J. Cheng, X. Chen, W. Sun, X. Fang, K. Hu, Z. Xie, T. Wang, and L. Wen, "A bio-inspired soft robotic arm: Kinematic modeling and hydrodynamic experiments," *Journal of Bionic Engineering*, vol. 15, pp. 204–219, 2018.

[166] Z. Gong, B. Chen, J. Liu, X. Fang, Z. Liu, T. Wang, and L. Wen, "An opposite-bending-and-extension soft robotic manipulator for delicate grasping in shallow water," *Frontiers in Robotics and AI*, vol. 6, p. 26, 2019.

[167] T. Zheng, D. T. Branson, E. Guglielmino, R. Kang, G. A. Medrano Cerda, M. Cianchetti, M. Follador, I. S. Godage, and D. G. Caldwell, "Model validation of an octopus inspired continuum robotic arm for use in underwater environments," *Journal of Mechanisms and Robotics*, vol. 5, no. 2, p. 021004, 2013.

[168] A. Poka, D. Ludovico, F. Manara, L. D. M. C. Dal Verme, C. Canali, G. Berselli, and D. G. Caldwell, "Structural optimisation of a cable-driven hyper-redundant manipulator," in *2025 IEEE/ASME International Conference on Advanced Intelligent Mechatronics (AIM)*, pp. 1–6, IEEE, 2025.

[169] F. Mariano, R. F. Pitzalis, L. Monica, J. Ortiz, and G. Berselli, "Traditional vs generative design optimization for novel wrist exoskeleton," in *2024 20th*

IEEE/ASME International Conference on Mechatronic and Embedded Systems and Applications (MESA), pp. 1–7, IEEE, 2024.

[170] O. Sigmund, "Topology optimization: a tool for the tailoring of structures and materials," *Philosophical Transactions of the Royal Society of London. Series A: Mathematical, Physical and Engineering Sciences*, vol. 358, no. 1765, pp. 211–227, 2000.

[171] J. Wu, X. Qian, and M. Y. Wang, "Advances in generative design," *Computer-Aided Design*, vol. 116, no. 102733, pp. 10–1016, 2019.

[172] Y. Cengel and J. Cimbala, *Ebook: Fluid mechanics fundamentals and applications (si units)*. McGraw Hill, 2013.

[173] M. Charras-Garrido and P. Lezaud, "Extreme value analysis: an introduction," *Journal de la société française de statistique*, vol. 154, no. 2, pp. 66–97, 2013.

[174] E. Gilleland, M. Ribatet, and A. G. Stephenson, "A software review for extreme value analysis," *Extremes*, vol. 16, pp. 103–119, 2013.

[175] Ö. Özdilli, "Comparison of the surface quality of the products manufactured by the plastic injection molding and sla and fdm method," *International Journal of Engineering Research and Development*, vol. 13, no. 2, pp. 428–437, 2021.

[176] A. D. Banjo, V. Agrawal, M. L. Auad, and A.-D. N. Celestine, "Moisture-induced changes in the mechanical behavior of 3d printed polymers," *Composites Part C: Open Access*, vol. 7, p. 100243, 2022.

[177] A. Poka, F. Manara, D. Ludovico, A. Pistone, L. D. M. C. Dal Verme, G. Berselli, D. G. Caldwell, and C. Canali, "Design of a torsional stiffener for a cable-driven hyper-redundant robot composed of gear transmission joints," *The International Journal of Advanced Manufacturing Technology*, vol. 136, no. 9, pp. 3945–3956, 2025.

APPENDIX A

NYLON AND ZYLON MATERIAL PROPERTIES

Table A.1 presents the material properties of Nylon.

Sintered Part Density	0.95 g/cm^2
Tensile Strength	50 MPa
Flexural Strength	60 MPa
Tensile Modulus	1700 MPa
Flexural Modulus	1700 MPa
Elongation at Yield	14 %
Elongation at Break	22 %
Heat Deflection Temperature (at 0.45MPa - at 1.82MPa)	182°C - 97°C

Table A.1 Properties of 3D-printed PA 12

Table A.2 shows the material properties of synthetic Zylon fibres.

Strength	Stiffness	Density	Decomposition Temperature
5800 MPa	270 GPa	1.56 g/cm^3	650 °C

Table A.2 Zylon Fibres Material Properties

APPENDIX B

SUMMARY OF FOUNDATIONAL MODELS AND PRIOR WORK

This appendix provides an overview of core models and definitions introduced in earlier work that are referenced in the present thesis. It is intended to make the thesis self-contained and to facilitate understanding of the key mathematical and mechanical concepts that support the design, optimisation and experimental analysis.

B.1 TENDON ROUTING TOPOLOGY

The mechanical behaviour of an HR manipulator is strictly defined by how tendons are guided from the base to the distal links. This topology is codified using a discrete Routing Matrix.

B.1.1 THE ROUTING MATRIX

Consider a manipulator with n joints and m tendons. The routing topology is represented by a matrix $T_{routing} \in \mathbb{Z}^{n \times m}$. Each element $t_{i,j}$ corresponds to the specific routing port index through which tendon j passes at joint i.

$$T_{rout} = \begin{bmatrix} t_{1,1} & t_{1,2} & \cdots & t_{1,m} \\ t_{2,1} & t_{2,2} & \cdots & t_{2,m} \\ \vdots & \vdots & \ddots & \vdots \\ t_{n,1} & t_{n,2} & \cdots & t_{n,m} \end{bmatrix} \tag{B.1}$$

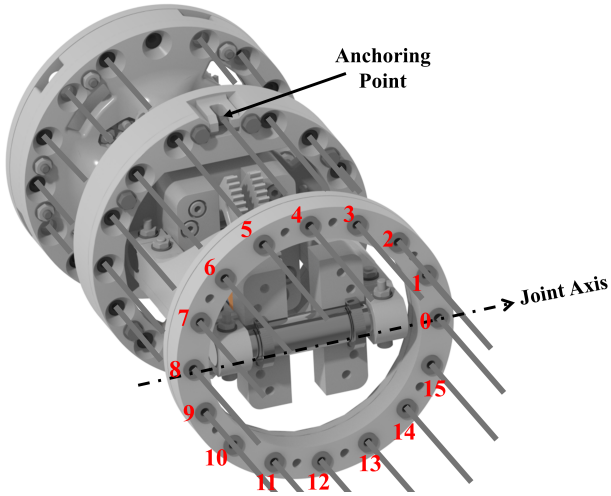


Figure B.1 Schematic of the tendon routing ports distributed along the flange pitch circle.

A value of $t_{i,j} = 0$ indicates that the tendon does not interact with that joint (i.e., it passes through the neutral axis or terminates before that joint). Non-zero integers represent specific ports distributed along the pitch circle of the joint disks. Figure B.1 shows the routing ports distributed along the flanges.

B.1.2 Geometric Mapping through the Matrix D

To translate the discrete indices of $T_{routing}$ into physical lever arms, a mapping function based on the flange geometry is defined. Assuming the ports are equally spaced on a pitch circle of diameter d_c, the lever arm $d_{i,j}$ for tendon j at joint i is:

$$d_{i,j} = \frac{d_c}{2} \cdot \sin\left(t_{i,j} \cdot \frac{2\pi}{N_p}\right) \tag{B.2}$$

where N_p is the total number of available ports. This generates the Distance Matrix $D \in \mathbb{R}^{n \times m}$, which contains the effective moment arms for every tendon-joint interaction.

B.2 Static Model via Newton-Euler Recursion

Unlike global energy methods, the static model employed here utilises a recursive Newton-Euler approach. The kinematics are propagated forward from the base to the tip, while forces are resolved backwards from the tip to the base. This allows for a detailed analysis of internal reaction forces within the joint sub-components (flanges and links).

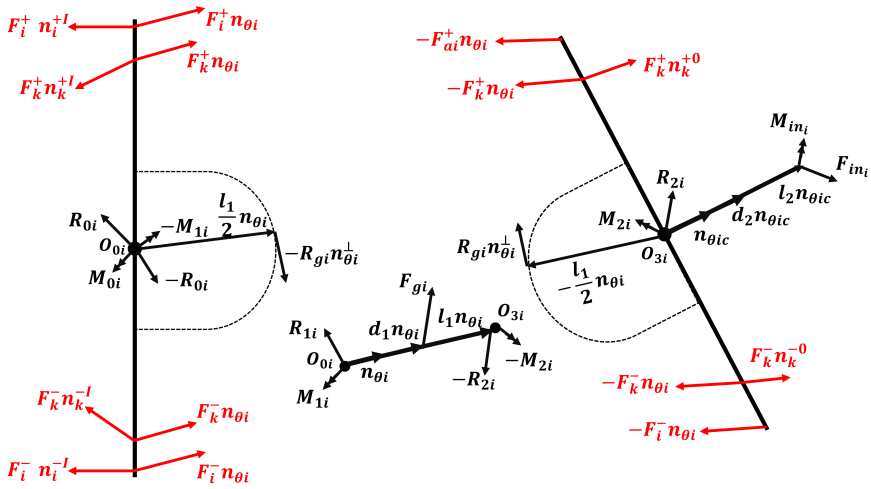


Figure B.2 Free body diagram of the joint module showing internal forces and tendon interactions. Tendon-flange interaction forces are shown in red.

B.2.1 Joint Decomposition and Load Definitions

The static equilibrium is solved for a single joint module i, which is mechanically decomposed into three rigid bodies: the Inner Flange, the Intermediate Link, and the Outer Flange, as shown in figure B.2.

The tendon forces acting on the joint are defined as an antagonistic pair, F_i^+ and F_i^-, a preload component F_{t_i} and a differential actuation force ΔF_i:

$$F_i^+ = F_{t_i} + \frac{1}{2}\Delta F_i(\theta, T_{routing}, F_i^n, \Delta F_i^n) \tag{B.3}$$

$$F_i^- = F_{t_i} - \frac{1}{2}\Delta F_i(\theta, T_{routing}, F_i^n, \Delta F_i^n) \tag{B.4}$$

where F_i^n and ΔF_i^n represent the vectors of forces for all subsequent distal joints $(i+1 \ldots n)$.

B.2.2 Equilibrium Equations

The equilibrium is established by isolating the three bodies. We define the reference frames O_{0_i} (Inner Flange) and O_{3_i} (Outer Flange).

1. Outer Flange Equilibrium

The outer flange is subject to the external load from the subsequent module (F_{IN_i}, M_{IN_i}), the reaction from the intermediate link (R_{2_i}, M_{2_i}), gravity (F_{g_2}), and the tendon forces.

Force Equilibrium:

$$F_{IN_i} + F_{g_2} + R_{2_i} + R_{g_i} n_{\theta_i}^{\perp} - F_i^{+} n_{\theta_i} - F_i^{-} n_{\theta_i} - \sum_{k=i+1}^{n} \left[F_k^{+} (n_{\theta_i} - n_k^{+o}) + F_k^{-} (n_{\theta_i} - n_k^{-o}) \right] = 0 \tag{B.5}$$

Moment Equilibrium (about O_{3_i}):

$$\begin{aligned} M_{IN_i} + M_{2_i} + l_2 n_{\theta_{ic}} \times F_{IN_i} + d_2 n_{\theta_{ic}} \times F_{g_2} - \frac{l_2}{2} n_{\theta_i} \times R_{g_i} n_{\theta_i}^{\perp} \\ - \frac{d_c}{2} n_{r,i}^{+o} \times F_i^{+} n_{\theta_i} + \frac{d_c}{2} n_{r,i}^{+o} \times F_i^{-} n_{\theta_i} \\ + \frac{d_c}{2} \sum_{k=i+1}^{n} \left\{ n_{r,k}^{+o} \times [F_k^{+} (n_{\theta_i} - n_k^{+o})] - n_{r,k}^{+o} \times [F_k^{-} (n_{\theta_i} - n_k^{-o})] \right\} = 0 \end{aligned} \tag{B.6}$$

Here, R_{g_i} represents the gear constraint reaction, and n vectors denote the direction unit vectors for tendons and structural axes.

2. Intermediate Link Equilibrium

The intermediate link connects the two flanges and balances the reactions R_{1_i} (from inner) and R_{2_i} (from outer).

Force Equilibrium:

$$R_{1_i} - R_{2_i} + F_{g_1} = 0 \tag{B.7}$$

Moment Equilibrium (about O_{0_i}):

$$M_{1_i} - M_{2_i} + d_1 n_{\theta_i} \times F_{g_1} - l_1 n_{\theta_i} \times R_{2_i} = 0 \tag{B.8}$$

3. Inner Flange Equilibrium

The inner flange connects to the previous module and supports the tendons entering the joint.

Force Equilibrium:

$$\begin{aligned} - R_{1_i} + R_{0_i} - R_{g_i} n_{\theta_i}^{\perp} + F_i^{+} (n_i^{+1} + n_{\theta_i}) + F_i^{-} (n_i^{-1} + n_{\theta_i}) \\ + \sum_{k=i+1}^{n} \left[F_k^{+} (n_k^{+1} + n_{\theta_i}) + F_k^{-} (n_k^{-1} + n_{\theta_i}) \right] = 0 \end{aligned} \tag{B.9}$$

Moment Equilibrium (about O_{0_i}):

$$-M_{1_i}+M_{0_i}-\frac{l_1}{2}(n_{\theta_i}\times R_{g_i}n_{\theta_i}^{\perp}) + \frac{d_c}{2}n_{r,i}^{I}\times\left[F_i^{+}(n_i^{+1}+n_{\theta_i})-F_i^{-}(n_i^{-1}+n_{\theta_i})\right] + \frac{d_c}{2}\sum_{k=i+1}^{n}\left[n_{r,k}^{I}\times F_k^{+}(n_k^{+1}+n_{\theta_i})-n_{r,k}^{I}\times F_k^{-}(n_k^{-1}+n_{\theta_i})\right]=0 \quad \text{(B.10)}$$

B.2.3 Matrix Resolution

The system of equilibrium equations for joint i contains 16 unknown scalar variables. These can be arranged into a linear system:

$$Q_i x_i = c_i \quad \text{(B.11)}$$

where the unknown vector x_i contains the reaction forces/moments and the required differential tendon force ΔF_i:

$$x_i = \left[R_{2_i}^T, \quad M_{2_i}^T, \quad R_{1_i}^T, \quad M_{1_i}^T, \quad R_{0_i}^T, \quad R_{g_i}, \quad \Delta F_i\right]^T \quad \text{(B.12)}$$

The vector c_i contains the known terms (external loads, gravity, and tendon forces from distal joints). By inverting Q_i, we solve for the required ΔF_i to maintain static equilibrium.

B.3 Optimisation of Cable Preloads

To prevent slack during operation, a minimum-tension constraint is enforced. The preload F_{t_i} is determined by solving an optimisation problem for the entire workspace.

We require that for all valid joint configurations q within limits ($|q| < q_{lim}$):

$$F_i^{\pm}(q, T_{routing}, F_i^n) > F_0 \quad \text{(B.13)}$$

where F_0 is a user-defined safety margin of minimum tension threshold chosen to enforce the no-slack condition. This is formulated as a minimisation problem to find the lowest necessary preload that satisfies the constraint:

$$F_{t_i} = F_0 + \max_{|q_j|<q_l}\left(\frac{1}{2}|\Delta F_i(q, T_{routing}, F_i^n)|\right) \quad \text{(B.14)}$$

This optimisation is solved using the Simplex method, a heuristic algorithm robust to non-linearities, ensuring that the tendons stay tensioned for all static loading scenarios specified by the robot's trajectory.

APPENDIX C

ACTUATION HARDWARE DETAILS

While the sensing system relies on a custom distributed SPI architecture, the actuation relies on an industrial CANopen network. The robot employs Maxon DCX35L motors driven by EPOS4 digital positioning controllers. The CompactRIO (cRIO) serves as the high-level controller, closing the control loop by reading the joint sensors via SPI and sending actuation commands to the drivers via CAN.

The actuation unit consists of a Maxon DCX35L DC motor characterised by a compact 35 *mm* diameter and high power density. The motor is brushed, providing a nominal torque of 121 *mNm* at a nominal speed of 7160 rpm and a stall torque of 2030 *mNm*. It is coupled with a GGPX37 planetary gearhead with a $26:1$ reduction ratio, driving a 3 *mm* pitch lead screw through an additional $1.5:1$ external gear reduction. The nominal linear speed is 9.2 mm/s and has a theoretical starting push force of approximately 33.16 *kN* and a nominal push force of 1.98 *kN*, allowing the system to handle significant axial loads. The linear actuators have a useful stroke of approximately 310 *mm*. The virtual prototype of the assembled linear actuator unit is shown in figure C.1. Each motor is controlled by a Maxon EPOS4 Module $50/8$, which handles the low-level current (torque) and velocity control loops internally at a frequency of 2.5 kHz. This compact, modular driver supports up to 50 V and 8000 *mA* continuous current, and the nominal current of 4260 *mA* of the motor. Communication between the cRIO (Master) and the EPOS4 drivers (Slaves) is implemented over a Controller Area Network (CAN) bus using the CANopen protocol.

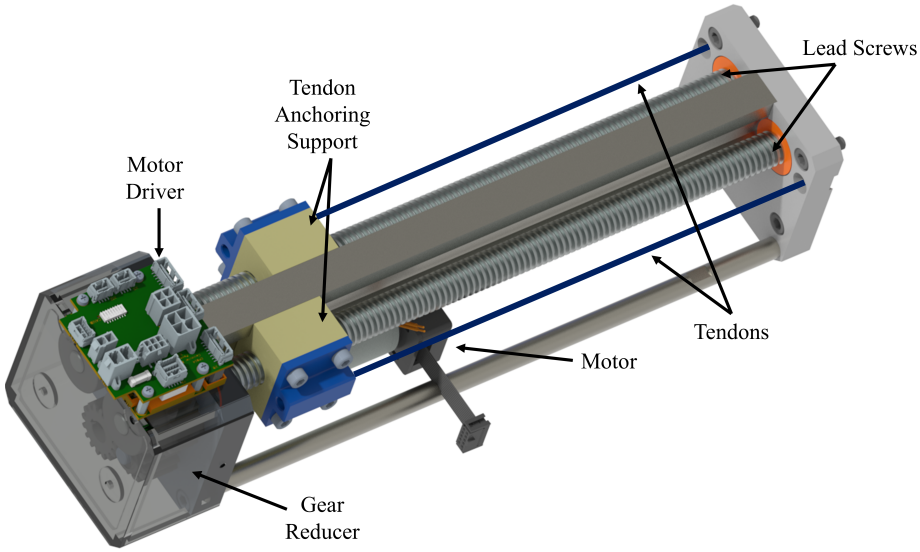


Figure C.1 Virtual prototype of the linear actuator

APPENDIX D

TENSIONING SYSTEM TEST RESULTS: TENSION IN MOTION

Figures D.1–D.5 present the tendon force profiles for joints 1 through 5, respectively, for each tendon (F_{sl}^{+} and F_{sl}^{-}) obtained from the experimental trials conducted during manipulator motion.

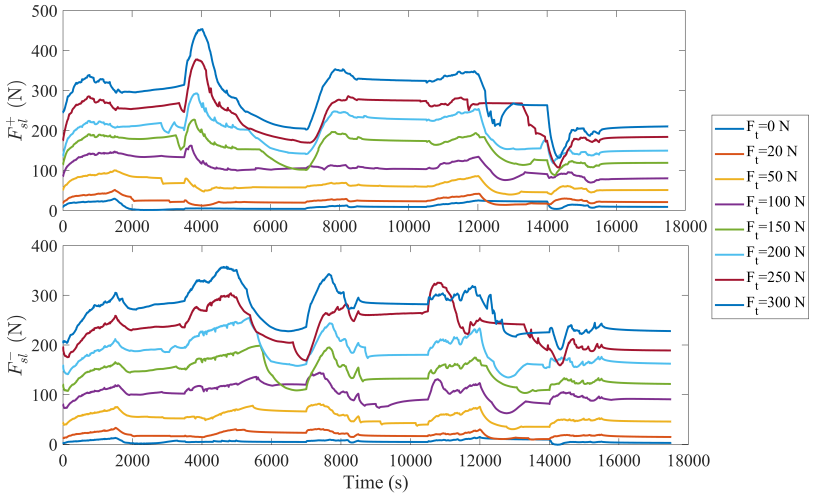


Figure D.1 Joint 1 tendon tension trends for each F_t setpoint

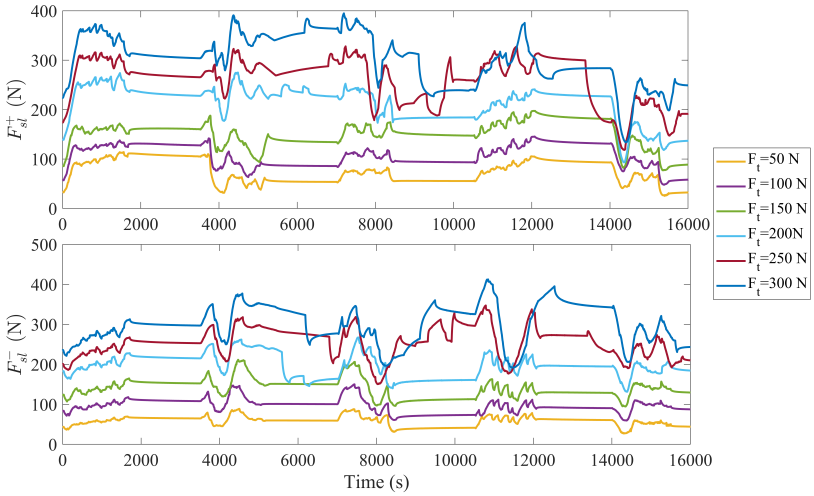


Figure D.2 Joint 2 tendon tension trends for each F_t setpoint

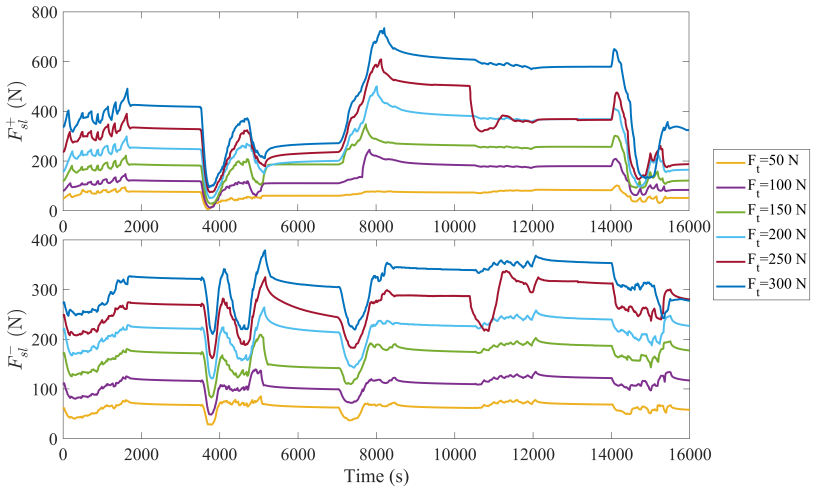


Figure D.3 Joint 3 tendon tension trends for each F_t setpoint

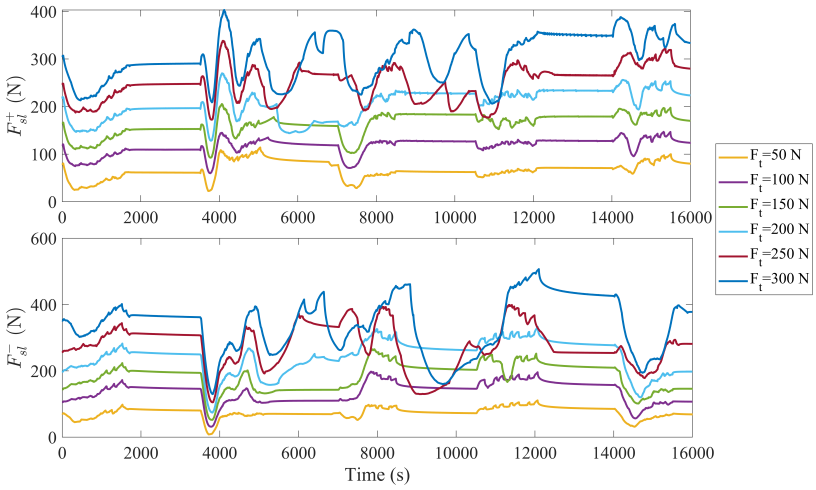


Figure D.4 Joint 4 tendon tension trends for each F_t setpoint

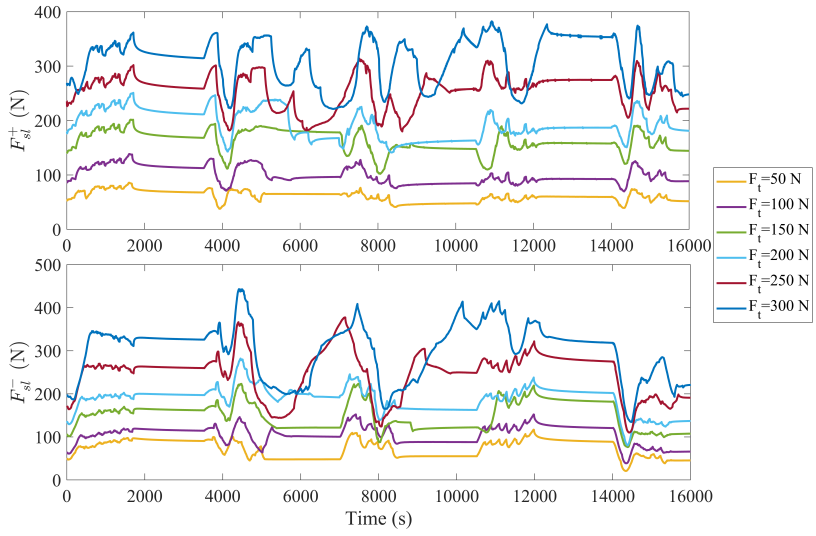


Figure D.5 Joint 5 tendon tension trends for each F_t setpoint